

**STATE RESEARCH CENTER OF RUSSIA
INSTITUTE FOR HIGH ENERGY PHYSICS**

REPORT

**Conceptual Design Work and Neutrino Beam
Calculations for the NuMI Project**

(Tasks C of the Accord between FNAL and IHEP)

A.Abramov, I.Azhgirey, S.Denisov, P.Galkin, N.Galyaev, V.Garkusha,
A.Kharlamov, Yu.Khodyrev, S.Knyazev, I.Kurochkin, E.Lomakin,
F.Novoskoltsev, A.Ryabov, V.Seleznev, Z.Sharifullin, E.Ustinov,
V.Zapolsky, V.Zarucheisky

Protvino 1997

Contents

1	Development of Target Design	3
1.1	Production Efficiency	3
1.2	Cooling and stresses	6
1.3	Target Head	10
1.4	Target Unit	11
1.5	Target Complex	13
1.5.1	Shielding	13
1.5.2	Internal Components	15
1.5.3	External Components	16
1.6	Replacement	17
1.7	General Beam Layout	19
1.8	Beam Diagnostic System	19
2	NuMI Neutrino Beams using the Parabolic Horn (Lens)	
	Focusing System	52
2.1	Wide Band Neutrino Beam	52
2.2	Narrow Band Neutrino Beam	53
3	Parabolic Lenses	65
3.1	Lens LX	65
3.2	Stripline	66
3.3	General layout	67
3.4	Focusing Device Support Design	67
3.5	Replacement of failed lens	68
3.6	Switching between Wide Band and Narrow Band Beams	69

1 Development of Target Design

This section of the Report presents new results of various studies of the target design for NuMI project and the details of some results reported earlier. The main attention was paid to the description of the accepted and proposed technical decisions for basic units and components of the target station.

In all cases for the primary proton beam the following parameters were assumed:

Energy	120 GeV
Intensity	$4 \cdot 10^{13}$ ppp
Duration of spill	1 ms
Horizontal emittance	0.117 mm·mrad
Vertical emittance	0.24 mm·mrad
Cycle time	1.9 s

As a rule, the presented results concern to the beamline with a wide band neutrino beam (WBB).

1.1 Production Efficiency

In addition to the computation results given in the previous IHEP Report [1] on the target efficiency as a function of the target configuration, a large series of calculations for optimizing the length L_t and the density ρ_c of the graphite cylindrical target has been performed using the modified program MARS [2]. In these calculations the target efficiency was estimated by a density of positive pions emerging from the target in three-dimensional space of the following parameters: energy E_π , radius, and a trajectory angle to the Z -axis θ_z . The pion trajectory parameters are taken at the beam line section Z_s , corresponding to a middle of the first assembly of parabolic lenses.

The geometry used for these calculations is shown in Figure 1.1. Only those particles which hit the screen with a radius of $R_s=12$ cm and have the trajectory angles to Z -axis less than $\theta_z=40$ mrad were taken into account. The screen radius R_s and the full angle θ_z are divided into a given number of cells, over which the statistical weights of particles (from Monte Carlo simulation of particle cascades) hitting the screen are distributed.

Similarly, for E_π a sufficiently large interval is taken, also divided into cells. The distance between the target center and the screen was kept constant $Z_s=300$ cm.

It was assumed that the target is uniform longitudinally (without gaps). The calculations were performed in the following sequence. Several target lengths L_t were taken. For each length the yield of positive pions was determined as a function of the graphite density. This dependence allows to evaluate an optimum density corresponding to the maximum yield for a given length. For the energy interval of 35–45 GeV and angular interval of 0–40 mrad such dependences are presented in Figure 1.2 for $L_t = 100, 125, 140, 150, 160, 170$ and 200 cm. In this Figure the pion yield is expressed in relative units, so 1.0 corresponds to the pion yield for a target with $L_t = 100$ cm and $\rho_c = 1.81$ g/cm³. The dashed line passes through the points satisfying the condition $L_t \cdot \rho_c = 181$ g/cm². For the angular interval of 0–10 mrad at the same E_π and L_t similar dependences are shown in Figure 1.3.

The relation between the target length and the optimum density ρ_{opt} is shown in Figure 1.4. The pion flux at ρ_{opt} (pion yield has the maximum value) as a function of the target length is also given in Figure 1.4 for the angular intervals of 0–10 and 0–40 mrad. The pion yields for cylindrical, fin and plate uniform graphite targets, the length of 100 cm and density of 1.81 g/cm³ are given in Table 1.1. In this Table the relative units for the energy intervals of 25–35 and 35–45 GeV are different: the ratio of the yield units from the first to the second cases is equal to 2.42.

For a cylindrical beryllium target with $L_t = 90$ cm (L_t for beryllium is taken smaller than for graphite because of its smaller nuclear interaction length) and density of 1.85 g/cm³ the pion yield is approximately equal to 1.05 relative units. It's necessary to note that graphite density of 1.81 g/cm³ and beryllium length of 90 cm are not optimum. For optimum values (1.95 g/cm³ and 130 cm, respectively) the yields are higher by 5–10%.

Material, configuration	Cross-size, mm, mm×mm	E_π , GeV	
		25 – 35	35 – 45
C-cylinder	ø3.4	0.948	0.923
	ø3.8	1.000	1.000
	ø4.2	0.948	0.940
Be-cylinder	ø3.8	1.025	1.054
C-fin	3.4×51.7	0.869	0.964
	3.8×51.9	0.946	0.964
	4.2×52.1	0.882	0.964
C-plate	3.4×100	0.911	0.917
	3.8×100	0.904	0.883
	4.2×100	0.881	0.881

Table 1.1: The production efficiency of the beryllium and graphite targets with lengths of 90 cm (Be), 100 cm (C) and densities of 1.85 g/cm³ (Be), 1.81 g/cm³ (C) and for the pion angular divergence of ± 40 mrad.

In Table 1.2 the pion yields are given for uniform and segmented graphite targets with a radius of 0.19 cm, a length of 160 cm and density of 1.2 g/cm³. The second line in the table shows the reduction of the pion yield from the target due to graphite disks used for fixing of the cylindrical segments.

Longitudinal structure	Segment length, mm	E_π , GeV	
		25 – 35	35 – 45
uniform	—	1.000	1.000
uniform+disks	—	0.965	0.962
5 segments	212	0.863	0.850
10 segments	106	0.928	0.929

Table 1.2: The production efficiency of the distributed and segmented graphite targets with cylindrical configuration, the total length of 160 cm, the average density of 1.2 g/cm³ and for the pion angular divergence of ± 40 mrad.

In case of segmented targets, the length (L_s), number (N_s) and density (ρ_c) of segments, and the gap length (L_g) are bound by the following relations:

$$L_s[cm] = \frac{192}{N_s \cdot \rho_c[g/cm^3]}; \quad L_g[cm] = \frac{160 - N_s \cdot L_s[cm]}{N_s - 1}.$$

These relations are obtained from the condition of conservation of the target total length of 160 cm and its averaged density of 1.2 g/cm³.

The relative units for pion yield used in Table 1.2 are different from units of Table 1.1. The yield corresponding to 1 unit in Table 1.2 is higher by about 25% than one in Table 1.1. The relative units for the energy intervals of 25–35 and 35–45 GeV are also different, and are in the ratio of 2.14. The second line in Table 1.2 shows how much the pion yield is reduced by graphite cylinder with the length of 160 cm and effective density of 0.0181 g/cm³. This cylinder surrounded the target by a layer with radius of 70 mm, which corresponded to 16 disks with thickness 1 mm each.

1.2 Cooling and stresses

The way of target cooling affects essentially the working resource. The results of analysis of the two cooling methods, by forced gas convection (helium blow) and by conduction through a lateral target part into a cooling water system, are shown below.

Helium cooling is considered for the WBB cylindrical graphite target of 0.4 cm diameter. The total heat power deposited in this target reaches 1400 W. Maximum energy is deposited at the initial part of a target and comes to 20 W/cm for longitudinal distribution of the heat power. At the downstream target end this quantity decreases by a factor of two. At such thermal load a target with natural cooling (by non–forced convection and radiation) would be heated to a very high temperature, which excludes an opportunity of its reliable long operation. The downturn of temperature to acceptable level is provided by a forced gas convection.

The target temperature regime is characterized by an average steady-state temperature and a maximum jump of temperature in the moment of proton beam spill. The temperature jump depends on the proton beam parameters and on the target material heat properties. The steady-state temperature is defined by the cooling system efficiency. The efficiency of

target cooling by helium flow with different velocities is determined from a homologous equation for the case of transverse gas stream to a cylinder axis. In calculations, three different homologous equations were used including that given in [4]. The discrepancy of results in all cases was within the limits of the calculation accuracy. In a case of transverse blow of a cylinder there is a strong non-uniformity of the heat transfer over the cylinder circumference — from 1.7 of the average heat transfer factor in the direction of a gas flow to 0.4 in the transverse direction. Table 1.3 shows the heat transfer factors averaged over circumference at the target surface and the steady-state temperatures for several flow speeds.

Velocity, m/s	4	10	20
Convection coefficient, $\text{W/m}^2/^{\circ}\text{C}$	200	310	450
Steady-state temperature, $^{\circ}\text{C}$	800	520	365
Helium flow, l/s/cm	0.6	1.5	3.0
Temperature rise, $^{\circ}\text{C}$	41	16	8

Table 1.3: A convection coefficient, steady-state temperature of the target, the helium flow and the increase of helium temperature at target downstream versus the helium velocity.

The helium jet is formed by a flat nozzle placed 4 cm apart from the target surface for free passage of secondary particles. The nozzle width (0.6 cm) is chosen 1.5 times larger than the target diameter to compensate for a jet blurring. The helium speed at the nozzle exit is taken 1.5 times higher than the speed at the target surface to compensate for its reduction. Table 1.3 shows the rate of helium flow per 1 cm of the target length at the maximum energy deposition and the helium temperature gain as functions of the blow speed. The maximum rate of helium flow at the speed of 20 m/s makes up about 800 m³/h for the whole target. Figure 1.5 shows how the target temperature regime flattens out with time for various speeds of blow. One sees that with helium cooling the cylindrical carbon target gets the steady-state temperature regime after 10–20 spills. At the flow speed of 4 m/s the maximum temperature exceeds 1000 $^{\circ}\text{C}$ on the target surface just after the beam spill; at this moment up to 30% of heat removal is due to thermal radiation.

The calculations took into account the temperature dependence of the graphite specific heat, which is increased more than a factor of 2 with graphite heating up to 1000 °C. Figure 1.6 shows the temperature change on the axis and on the surface of a target after a single proton spill, with account for the temperature dependence of the graphite specific heat. The Figure shows that maximum temperature on the target axis does not exceed 380 °C, and the uniform distribution of temperature across the target occurs in 20–30 ms after a beam spill. On the nanosecond scale the heating with regard for the beam bunch structure should be calculated using C_v , not C_p . The performed estimations for graphite show that C_v exceeds C_p by 2–3% at the given above temperatures. This difference is within the accuracy limits of C_p determination for particular conditions.

Graphite is the most suitable material, capable to withstand the above mentioned temperatures. Beryllium is the material closest to graphite by the efficiency of production of secondary particles. But to ensure a suitable temperature regime of a beryllium cylindrical target operation it is necessary to increase the target diameter and the beam cross-section.

Heat conduction in combination with water cooling is applied, as a rule, to flat targets (plate, fin). Heat is removed through the side target planes having thermal contact with a target support cooled by water. The thickness of a working part of a target (zone of beam interaction) is equal to the diameter of the above considered cylindrical target. Therefore the heating of a working part of a flat target during the beam spill will be the same as with cylindrical one. The total energy deposition at the end of a flat target will be a little higher because of the energy deposition in a heat conducting part of a target. The total heating power in a flat target is about 1.5 times higher than that in cylindrical.

The steady-state temperature is defined by the heat conduction of a target material and the heat transfer factor at an entry face. More efficient heat removal allows to consider as a target material both graphite and beryllium. It is also possible to reduce the thickness of a heat removing part of a target to 0.2 cm in order to increase the yield of secondary particles. The steady-state temperatures for several variants of targets under various conditions of cooling are listed in Table 1.4.

Target material	Graphite			Beryllium		
Convection coefficient, W/m ² /°C	0.1	0.4	1.0	0.1	0.4	1.0
Plate 0.4 cm	360	164	126	280	118	86
Plate 0.2 cm	583	261	197	452	184	130
Fin 0.4 cm	670	296	222	520	208	146
Fin 0.2 cm	1100	490	366	860	340	237

Table 1.4: The steady-state temperatures of the C and Be targets versus the convection coefficient.

The lowest steady-state temperatures are reached by use of combined cooling — forced convection and conduction. With additional blow by helium (the averaged-over-surface factor of heat transfer is equal to 100W/m²/°C) the steady-state temperature is lowered by a factor of 1.5–2.

The temperature jump at the beam axis in the moment of spill amounts 170 °C for beryllium (without account for the temperature dependence of specific heat). For carbon, as well as for a thin target, it is 380 °C. After the uniform distribution of temperature over the working part of beryllium target the average increase in the temperature will make 80 °C (260 °C for carbon). The temperature dependence of heat conduction of graphite and beryllium in calculations was not taken into account (with heating to 1000 °C it decreases by 20–30% for some brand marks of graphite).

Figures 1.7 and 1.8 show the dependence of the quasi-static temperature stress on the proton beam size σ_p for cylindrical targets from beryllium and graphite, respectively. Here the σ_e value represents a maximum equivalent stress defined in accordance with criterion of maximum tangential stress (according to the maximum shear theory).

The quasi-static temperature stresses for a freely suspended cylindrical target were calculated by the formulas [6]. The temperature distribution was calculated from the formula

$$\Delta T(r) = \frac{3.82 \cdot 10^{-11} \cdot E(r) \cdot I_p}{C_p \cdot \rho},$$

where r is radial coordinate in cm; $T(r)$ is local temperature in °C; $E(r)$ is the local density of absorbed energy in GeV·cm⁻³; C_p is specific heat in cal/g/°C; ρ is density in g/cm³.

The C_p dependence on the temperature was neglected, and the C_p value was taken at 25 °C. In calculation of the quasistatic stress the temperature dependences of the elasticity module and of the temperature expansion factor were also neglected.

The dashed horizontal line in Figures 1.7 and 1.8 corresponds to the yield limit σ_{02} . As one can see, in static conditions the material of a graphite target will be overstressed if the beam size σ_p is less than 0.55 mm, and that of a target from Be — if σ_p is less than 0.8 mm. In the real case one should also take into account the fatigue effects from the thermocyclic character of a load and radiation destruction of a target material. Tentative estimations show that at least a triple safety factor is necessary for reliable work of targets.

1.3 Target Head

In this section the requirements for the choice of a target head design are generalized. These requirements are not complete, as far as at present the calculations on optimization of the target head parameters are not yet completed. From the analysis of obtained results of calculations for the secondary particles yield and thermo-mechanical effects it follows that one has to perform an additional more detailed study of various types of non-cylindrical targets (see Figure 1.9) and of the radiation influence on material properties. This analysis allows to make the following preliminary conclusions:

- For a cylindrical target with helium cooling the graphite is a more suitable material, than beryllium. In case of beryllium target the allowable size of a proton beam and, accordingly, the target diameter are factor of 1.5–2 larger than ones for a graphite target. This leads to reduction of the secondary particle yield and complication of a cooling system.
- The optimum length L_{opt} of a WBB graphite target is equal to 160–170 cm and the optimum density of graphite is equal to 1.2 g/cm³. But it is necessary to note that with reduction of density the thermophysical properties of graphite are essentially worsened, so that will not allow to use graphite with optimum density. At a density of graphite greater than optimum, the target is divided into segments, which are placed with intervals along the beam axis so that the total length of a target

is kept equal to the optimum length. It corresponds to the following relations:

$$L_s = \frac{L_{opt} \cdot \rho_{opt}}{N_s \cdot \rho_s}, \quad L_g = \frac{L_{opt} - N_s \cdot L_s}{N_s - 1},$$

where ρ_s – the segment graphite density, L_s – the segment length, L_g – the gap length, N_s – number of the segments.

- Production efficiency of various types of graphite targets with a flat configuration is lower by 5–15% than for cylindrical targets.
- Production efficiency of beryllium target is higher by 5–10% than efficiency of a graphite target at equal geometrical parameters of a proton beam and the targets.
- Conduction cooling is essentially more efficient than convection cooling. A reasonably reliable work of both beryllium and graphite targets (flat configuration) can be ensured only with conduction cooling or combinations of conduction with other methods of cooling. When taking into account the difference in technology of manufacturing and in character of destruction of targets from beryllium and graphite, the preferable material for manufacturing of flat targets is beryllium. Herewith the design of a target head can be, for example, one shown in Figure 1.9(c), and the proton beam may have ellipsoidal cross-section ($\sigma_x/\sigma_y=2$).
- In case of use of graphite the final choice of parameters of a target head and the modes of cooling requires a detailed study of erosion resistance of the thin graphite specimens in the conditions of long operation time at thermocyclic stresses and in the radiation fields of high intensity.

1.4 Target Unit

The target unit contains only a single target head placed in the target box. This box is hermetically sealed and filled by inert gas (helium) continuously circulating through it. The box is made from an aluminium or magnesium alloy. The external dimensions of the WBB target box are equal to $20 \times 30 \times 180$ cm³.

Figures 1.10 and 1.13 show the general view of the WBB target box. This box consists of the two main parts: a flat rigid base and a box casing

with parallelepiped form. At the upstream and downstream casing ends there are two titanium beam windows with thickness of 0.1 mm and diameters of 70 and 140 mm, respectively. The box casing is bolted to the box base to provide the necessary pack connection.

All internal components of the target unit are installed on the box base. The layout of these components is shown in Figures 1.11, 1.12 and 1.13 for the cylindrical and fin target partitioned into segments. In case of a cylindrical target each segment is fixed in two thin (1–2 mm) cross plates (plate support), which are inserted in slots of two cramp supports. These two cramp supports are rigidly connected to a common lower plate, which has an alignment device for the horizontal and vertical planes. Beryllium or graphite can be considered as material for the plate supports. For the cramp supports and lower plate one can use an aluminium or magnesium alloy. The connection between the cramp supports and the lower plate is insulated electrically as required for the Budal's target monitor.

Three slot-hole jets create a helium cooling flow on each target segment. The coolant to jets moves from a longitudinal collector in the box base. Here in the box base there are also channels of water cooling for thermostabilisation of the box base and for the reduction of thermal deformations. For this aim the target unit and the details connected with it are blown by external air, leaving out through a heat exchanger (see section 1.5.2). The temperature regime of the titanium windows is most hard in the entry window. In this window the temperature rise on the proton beam axis reaches 600°C . For the exit window the maximum temperature rise is equal to 100°C .

The target unit with a fin head, as seen from Figure 1.13, differs from the one described above, mainly by the character of the target segments fixing and the lateral arrangement of the helium cooling jets. The target support has a long extended vertical slit, in which the segment is fixed along the whole length. Vertical alignment of the segment is realized by changing its position in this slit. The electrical insulation of the target head is provided in this fixing slit. The lower plate of the target support is strongly clamped to the box base. Horizontal alignment of the target is provided by changing the position of the lower plate on the box base. This support allows a more rigid clamping of the target position than in the case of a cylindrical target. Besides, usage of combined cooling allows to reduce

by 2–3 times the steady-state temperature of the target as compared to the cylindrical target.

Figure 1.14 shows the configuration of the NBB target unit. In this case a beryllium finlike target with a cramp-shape head is used. The cooling is conduction in a combination with water system of cooling. The target length is about 50 cm, and corresponds to approximately one nuclear length. The target box size is equal to $120 \times 120 \times 500 \text{ mm}^3$. For effective suppression of background particles in a target unit, a downstream copper collimator is stipulated. Before the target box there is a security (shielding) aluminium collimator.

1.5 Target Complex

The general layout of the target complex is shown in Figure 1.15. The basic equipment and components of the target complex can be divided into three categories:

1. immobile and mobile radiation shielding;
2. components situated inside the shielding (in the "hot zone");
3. active (moving) electromechanical equipment, control and measuring devices and communications situated outside the shielding.

1.5.1 Shielding

The basic parameters and structure of radiation shielding in WBB version were defined in [3]. This shielding assumed the usage of steel and calcium carbonate.

For the presented shielding geometry the radiation fields around the target were calculated by the simulation code MARS'96 [2]. The computation model included the WBB graphite target of 156 cm length, the internal concrete (or marble) shielding at $R=[35;85]$ cm, the iron shielding at $R=[85;185]$ cm, the external concrete shielding at $R=[185;235]$ cm, the upstream collimator with the length of 25 cm and the downstream collimator with the length of 80 cm. Downstream collimator has a conical channel with $R_1 = 6.6$ cm, $R_2 = 9.8$ cm. Figure 1.16 shows longitudinal distributions over the concrete shielding of hadron fluence (hadron energy above 10 MeV) and absorbed dose, respectively. In this Figure zero Z-coordinate corresponds to the forward plug upstream edge. The upstream target end

is located at 204 cm. The primary beam has intensity $4 \cdot 10^{13}$ protons per a spill, the cycle time 1.9 s, and the number of spills is 10^7 per a year of NuMI work.

For the 30 days irradiation and 1 day cooling time the residual radiation were estimated by model [5]

$$P_c = 10^{-7} \cdot F_h,$$

where P_c is the gamma dose rate in rad/h, F_h is hadron fluence in $\text{cm}^{-2} \cdot \text{s}^{-1}$, and scaling factor

$$a(T, t) = 0.0738 \cdot \ln(1 + T/t),$$

where T is the irradiation time, t is the cooling time.

Figure 1.17 gives the longitudinal distribution of the induced radioactivity levels on the internal (solid) and external (dashed) surfaces of iron shielding. For the up- and downstream collimators the induced activity levels reach 15 rad/h and 10^4 rad/h, respectively.

The results presented in Figures 1.16 and 1.17 show that this amount of shielding is more than sufficient for effective suppression of the radiation around the target. It seems reasonable to remove the internal and partly external concrete (or marble) shielding.

This would simplify the installation of the target station equipment and removal of the target unit from the "hot zone".

For removal (or installation) of the target unit from the "hot zone" it is suggested to make a part of shielding mobile in order to provide a possibility to create a transport corridor to move the target unit from (or to) the "hot zone". Various cases were considered: with upper and lower location of the mechanisms to move the target unit, with big and small height of the crane hook above the floor. In the most complicated case with a upper location of mechanisms and small height of the hook the mobile shielding consists of the blocks removable beyond the limits of the stationery shielding and the blocks movable within the limits of the stationery shielding. The layout of these blocks is shown in Figure 1.18. In the created corridor the target unit is moved in the horizontal plane: firstly perpendicular to the beam axis, and then parallel to the axis in the upstream direction beyond the limits of the stationery shielding. In more details the procedure of the target unit removal is described in Section 1.6, both for the present case and for the case of lower location of mechanisms.

1.5.2 Internal Components

Basic components of a target station situated inside the shielding (in a "hot zone") are: target unit, heat exchanger for cooling air and position transceivers. Figure 1.19 shows the layout of these arrangements. The designs of various types of the proposed target units were described earlier in Section 1.4. The appearance of the WBB target box with details of fastening and connecting is given in Figure 1.10. At such a geometry of the box and the character of its fastening it is very important to minimize the temperature deformations both of the box itself and of its shafts. To ensure the necessary for this purpose thermostabilization, a water (for the box base) and air (for the other parts of target box and the shafts) cooling is used. The temperature of water and air should be kept constant with accuracy of ± 5 °C. The coolant fluxes should be reasonably intensive, as far as the energy deposition power in the target box and the shafts from radiation reaches 5–10 kW. Besides, when selecting parameters of a forced air cooling system it is necessary to take into account the energy deposition in the walls of a "hot zone". Even without regard for the energy deposition in the exit collimator (in view of a high density of energy deposition it requires water cooling), the energy deposition in the "hot zone" is approximately equal to 15–20 kW. (There is the same energy deposition in downstream collimator.) The necessary total flow of cooling air is on the order of ten thousands of cubic metre per hour.

The position transceivers are proposed for periodic precise calibration of X- and Y-coordinates of the up- and downstream ends of a target box. In a working situation the position transceivers are installed on the distance of 10–15 mm from the box end faces. Thus the position transceivers do not introduce any substance into the proton beam. Each position transceiver has two sensitive elements at the coordinates: $X_1 = Y_1 = +80 \pm 0.03$ mm; $X_2 = Y_2 = -80 \pm 0.03$ mm with respect to the beamline axis. Two sensitive elements are fixed at every end face of the target box with the same X/Y-coordinates, but with respect to the box axis. The elements of position transceivers are active: they generate electrical signals with levels depending on their positions with respect to the corresponding passive sensitive elements of the target box. At coincidence of the positions of active and passive elements the signal has extreme value. The detectors of this type developed in IHEP have characteristics for dependence of a signal on dis-

placement, which allow a position calibration in an automatic mode with a clamp zone of ± 20 mm and accuracy of ± 0.05 mm.

Position traneivers are produced from all-radiation hard materials. They are fastened on vertical rigid shafts by a length of approximately 2 m. To reduce the influence of fluctuations of temperature, the bars are produced from a material with a small factor of temperature expansion, and their thermostabilization is provided with a system of cooling. The supports of the top ends of shafts of position traneiver lean on a primary frame (see Figure 1.20). They are equipped by marks for geodetic hand-operated alignment.

The use of the described position traneiver allows:

- to execute the additional control of the target unit coordinates independent of the target position control system;
- to reduce requirements on the position accuracy of the initial installation of a target unit;
- to carry out the calibration of coordinates and angles of the target unit inclination at any time when necessary.

1.5.3 External Components

All the active electromechanical equipment for moving the target unit, elements of kinematic system, instruments and other auxiliary devices are installed at the top of the shielding. The main components of this assembly of equipment are (see Figure 1.15):

- primary frame (base support);
- secondary frame (alignment table);
- two suspension shafts;
- drives with electrical servomotors of constant current;
- position transducers.

Figure 1.20 shows some additional details of devices of this assembly. Figure 1.21 clarifies the kinematical scheme of alignment moves.

The primary frame is installed horizontally on iron shield. Its horizontal and vertical position and the alignment to geodetic frame are provided with hand-operated adjusting devices (jacks) directly fixed to the shield. On top of the primary frame there are three precise guiding and three supporting balls, on which the alignment table is installed. The alignment table can be moved horizontally with respect to the primary frame. The position of the alignment table is fixed by drives and rods connected with guides. The parallel moving of alignment table is executed by two servomotors (forward and back, for up- and downstream table ends) working synchronously. To turn the alignment table in horizontal plane only one of servomotors works.

The alignment table serves as a support for suspended shafts of a target unit. For this purpose two vertical guiding cylinders are rigidly fixed on it. Inside each cylinder there is a mobile piston rod connected with drive and suspended shaft. With two servomotors which can work synchronously and unsynchronously, one performs a necessary vertical move or a turn in vertical plane of the target unit with respect to the alignment table. Position of the alignment table and the piston rods are measured by photo-pulse transducers.

The following parameters of the driving gears (for the alignment equipment) were adopted:

Limits of linear moves of target box along X and Y axes	± 20 mm
Limits of angular turns of target box around the axes X and Y	± 2 mrad
Linear speed of moving	5 mm/s
Angular speed of turn	1 mrad/s
Accuracy of positioning	± 0.1 mm
AC power supply	220 V (50–60 Hz)
Power consumption	10 kW
Weight	500 kg

1.6 Replacement

The procedure of the target unit replacement with the upper location of the replacement mechanisms is shown in Figures 1.22 and 1.23. These Figures present the sequential stages of the target unit replacement procedure. To

allow replacement, a part of shielding is made movable (Figures 1.18). This part is placed under the platform at the right side. This shielding part has electrodrive with remote control.

The target unit removal sequence is as follows:

- The alignment table with shafts and target unit moves to the replacement position. In this case target unit is in the highest position, which is determined by position transducers and by status switches of the Y-axis limits.
- Coolant is drained out from the target unit pipes, then the pipes are closed.
- The target unit with the shafts is positioned in the "replacement zone" and then the shafts are released from the piston rods.
- After disconnection, the piston rods are raised up to 50 mm from the shafts. The shafts with target unit remain on the movable part of shielding (block 2 in the Figures 1.18 and 1.22(b)) and are fixed by pin joints.
- The crane traverse with ropes is fastened to the upper shaft flanges for the following transportation. This traverse and ropes have the automatic captures.
- To remove target unit together with the shafts, a transport corridor is created. The crane removes the shielding block 1 (see Figures 1.18 and 1.23, block sizes are equal to $2500 \times 2000 \times 400 \text{ mm}^3$).
- The shielding block 2 (see Figures 1.18 and 1.22(b), block sizes are equal to $2000 \times 2000 \times 400 \text{ mm}^3$) is moved by the electrodrive along the rails at the distance of 400 mm.
- The shielding block 3 (Figures 1.22(b) and 1.23(d), block sizes are equal to $2000 \times 1500 \times 250 \text{ mm}^3$) is removed.
- Crane removes the target unit and shafts along the created corridor (Figures 1.22(c) and 1.23(c)).

Second case of the target unit removal from the "hot zone" is illustrated in Figure 1.24. On this case a feature of the target station layout

is the lower location of the adjustment mechanisms. To replace target unit in the front part of the shielding, a corridor of 1500 mm length and $500 \times 250 \text{ mm}^2$ cross-section is created. A part of the movable shielding with size of $2500 \times 250 \times 1500 \text{ mm}^3$ and weight of 10 tons is lifted by a bridge crane at the height of 500 mm to create a transportation corridor. During removal and installation, the target unit is moved along the wheels fitted in the transportation corridor walls. The target unit has a tug hawser used for extracting target unit from the "hot zone". The hawser is fixed at the target unit base and stacked together with communications.

The major advantages of this method of target unit removal are:

- minimum weight and volume of the shielding to be moved for creating the transportation corridor;
- maximum caver of the "hot zone" during of the target unit removal.

1.7 General Beam Layout

Figures 1.25 and 1.26 present the general layouts of WBB and NBB beam-lines, respectively. These layouts correspond to the optics schemes with parabolic lenses described in section 2 (Figures 2.1 and 2.8). The longitudinal and cross sections of the target station are given in Figures 1.27 and 1.28, respectively. Figure 1.28 shows the target station section together with a target hall. The height of the hall and, in particular, the height of crane hook above the floor level are taken from the consideration to have possibility of the vertical removal of the target unit with shafts by the crane.

1.8 Beam Diagnostic System

To maintain the necessary focusing of a beam and to control its parameters for realization of physical experiments, a diagnostic system is proposed which allows to carry out the following tasks:

1. measurement of the proton beam position and profile (geometrical parameters);
2. measurement of the efficiency of proton beam interaction with a target;
3. measurement of the secondary particle multiplicity;
4. alignment of the secondary-particle focusing elements to the beam;

5. measurement of the secondary-beam geometrical parameters;
6. measurement of the proton beam intensity;
7. beam loss monitoring.

The layout of the beam diagnostic devices is shown in Figure 1.29. Notification is as follows:

- BLM is Beam Loss Monitor;
- BPM is Beam Position Monitor;
- BCT is Beam Current Transformer;
- SEP is Secondary Emission Profilometer;
- Target – Q is the charge of insulated pieces of a target;
- SPIC is Split-Plate Ion Chamber;
- SEM is Secondary Emission Monitor;
- C is Cerenkov Counter;
- MC is Muon Counter.

The above enumerated tuning procedures are realized by the following ways:

1. The initial tuning of a proton beam to the necessary direction with accuracy of 0.001 mrad is carried out with removed target. Three profilometers (coordinate detectors SEPup 1, 2 and SEPdump) are used in this case, located on the basis of 700 meters. The necessary parameters of a proton beam on a target are provided with the same devices SEPup 1 and 2. They have spatial resolution of 250 microns and angular resolution of 0.03 mrad. SEPup 1 and 2 carry out continuous monitoring of a beam during a physical experiment.

2. The direct evaluation of efficiency of a proton beam interaction with a target is carried out by a measurement of the charges from the electrical insulated parts of a target (Budal monitor). Maximum efficiency corresponds to the maximum charge. In addition, the target efficiency can be supervised by the monitor of secondary particles (BLM) located near the target.

3. Multiplicity in formation the secondary particles is calculated from the ratio of the SEM indications to the indications of the beam current transformer (BCT). Herewith first, in the mode with removed target, an absolute calibration of the secondary emission monitor (SEM) should be carried out. This ratio is maximum at optimum position of the target relative to the beam.

4. The alignment of focusing devices relative to the beam axis is controlled by a measuring the azimuth symmetry of distribution of secondary particles. For this purpose a four-section (along the azimuth) ionization chamber SPIC serves, which has a hole at the aperture center for a passage of proton beam. Besides, the correctness of the focusing devices position can be controlled by BLM located after the horns. Optimum position corresponds to the minimum signal from BLM.

5. The geometrical characteristics of the proton and hadron beams at an inlet and outlet of the decay pipe are measured by coordinate chambers SEPdown and SEPdump.

6. The intensity of proton beam in the beamline at a target is measured by the beam current transformer (BCT). The accuracy of measurement is better than 1%.

7. Beam loss is monitored by radiation monitors – ionization chambers located near the beam along the beamline.

By its location, the whole set of detectors for beam diagnostics (Figure 1.29) can be divided into three parts:

- the proton beamline;
- target enclosure;
- beam dump enclosure.

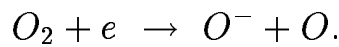
In the proton beamline there are the beam current transformer to measure intensity; beam position monitors (BPM) to measure the position of a center of gravity and the intensity; beam loss monitors (BLM).

In dump enclosure there are the multichannel chamber of secondary emission (SEPdump) and muon counters.

From the point of view of realization of the tuning procedures the most detailed analysis is carried out for detectors located in target enclosure. Taking into account a high level of intensity, heavy radiation and thermal

load, we propose a set of detectors most adapted to handling of the given tasks. The types and designs of several detectors differ from ones proposed in the Status Report [3]. The detector types that we propose, are tested in the IHEP proton beams and better match the general design of target station. The specification of these devices is given below.

SEPup 1 and 2 are the two-electrode plates multichannel chambers of secondary emission. The aperture is 50 mm, step of winding of 0.5 mm. The number of channels in each plane is 32. The basic advantage of these detectors is their work in a mode of secondary emission on atmospheric air without electrical displacement. Thus is used the dissociative mechanism of electron capture by molecules of oxygen (electronegative gas), i.e.



In this way a positive charge as great as a few percent of the beam charge is formed on the chamber metal electrodes for a while.

SEPdown is a large-frame two-electrode multichannel chamber of secondary emission. The aperture is 200 mm, step of winding is 1 mm. The number of channels in each plane is 32 with an opportunity of switching to different steps.

SEM is a high-vacuum chamber of secondary emission. Its functions: measurement of the total intensity; control of the left/right, top/bottom displacements; evaluation of the beam halo level.

SPIC is a 4-section air ionization chamber. At the center of the chamber aperture there is a hole ($\varnothing 200$ mm) for passage of a proton beam.

Q is the charge of electrical insulated target. It arises because of interaction protons with material target atoms. The amount of arisen δ -electrons corresponding one length unit and one energy unit is

$$\frac{d^2 N}{dE dx} = \frac{kZ}{AT^2} \sim Q,$$

where k – constant, Z – atomic number, A – atomic weight of target material, T – electron kinetic energy. The waiting value of charge is fifteen per cent from beam ones.

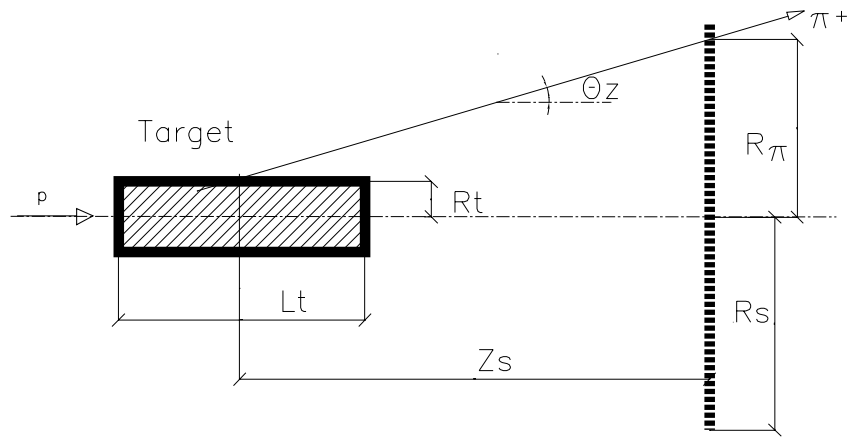


Figure 1.1: The geometry for production efficiency calculations.

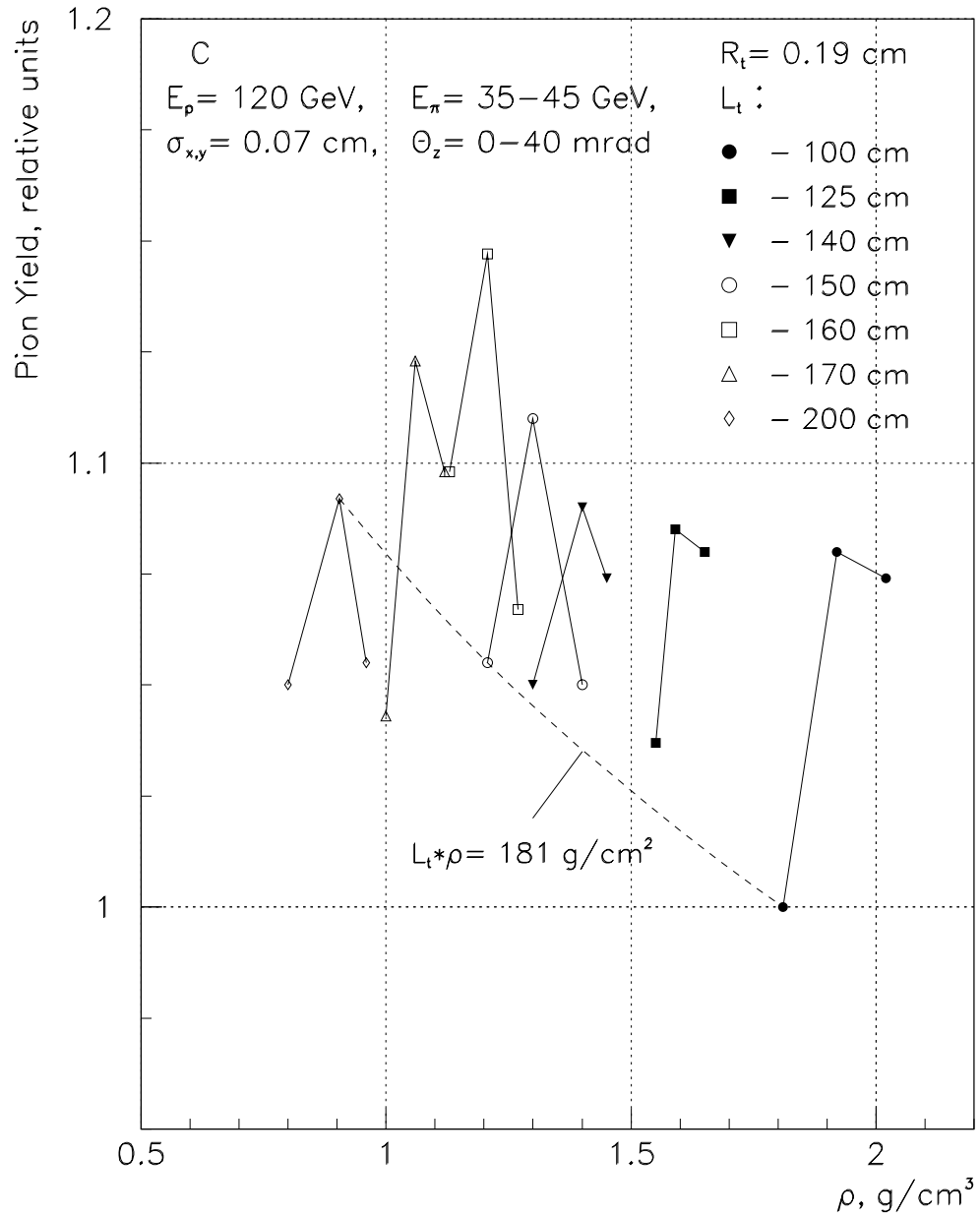


Figure 1.2: The pion yield at the angular divergence of $\pm 40 \text{ mrad}$ as a function of the graphite density for various target lengths.

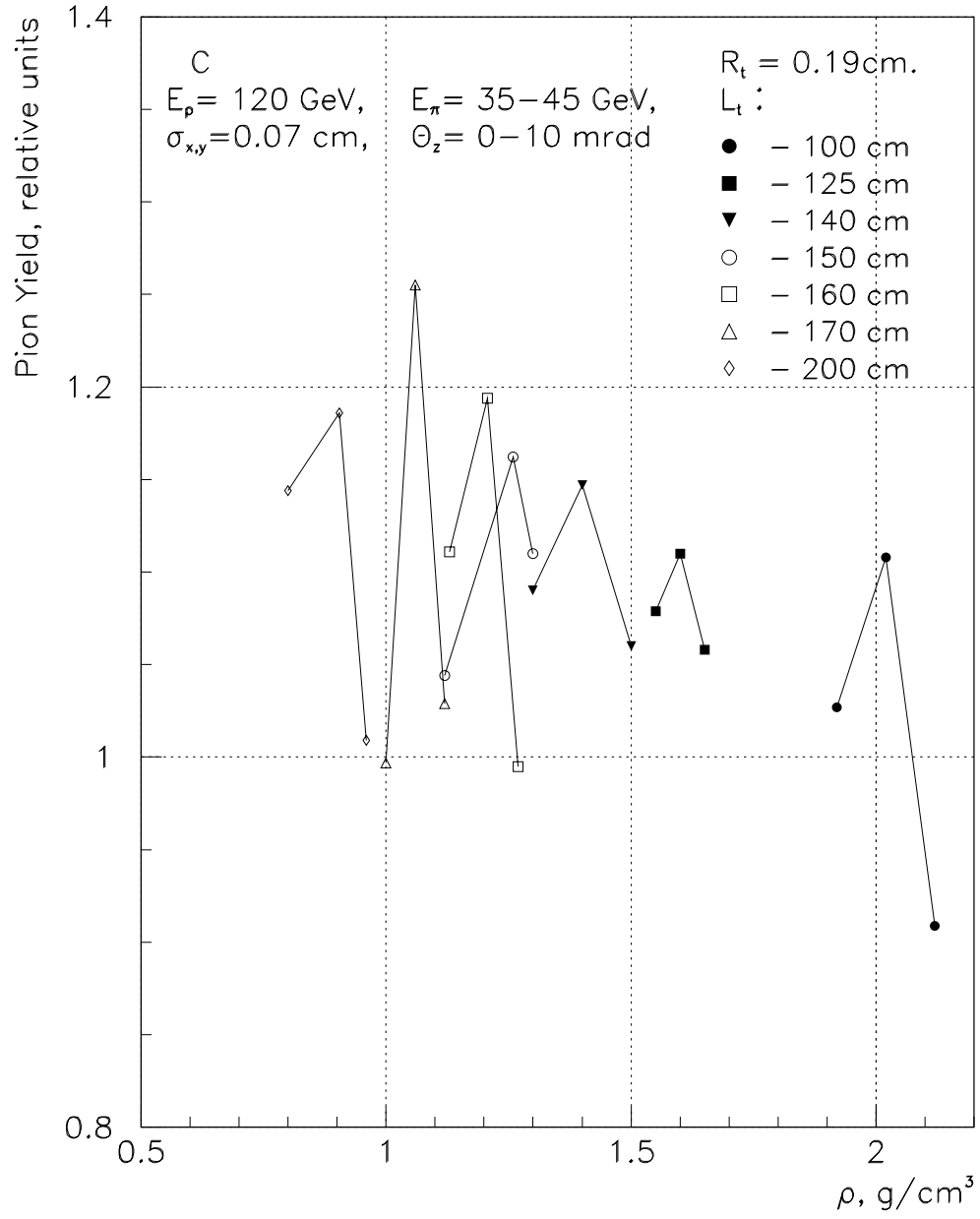


Figure 1.3: The pion yield at the angular divergence of $\pm 10 \text{ mrad}$ as a function of the graphite density for various target lengths.

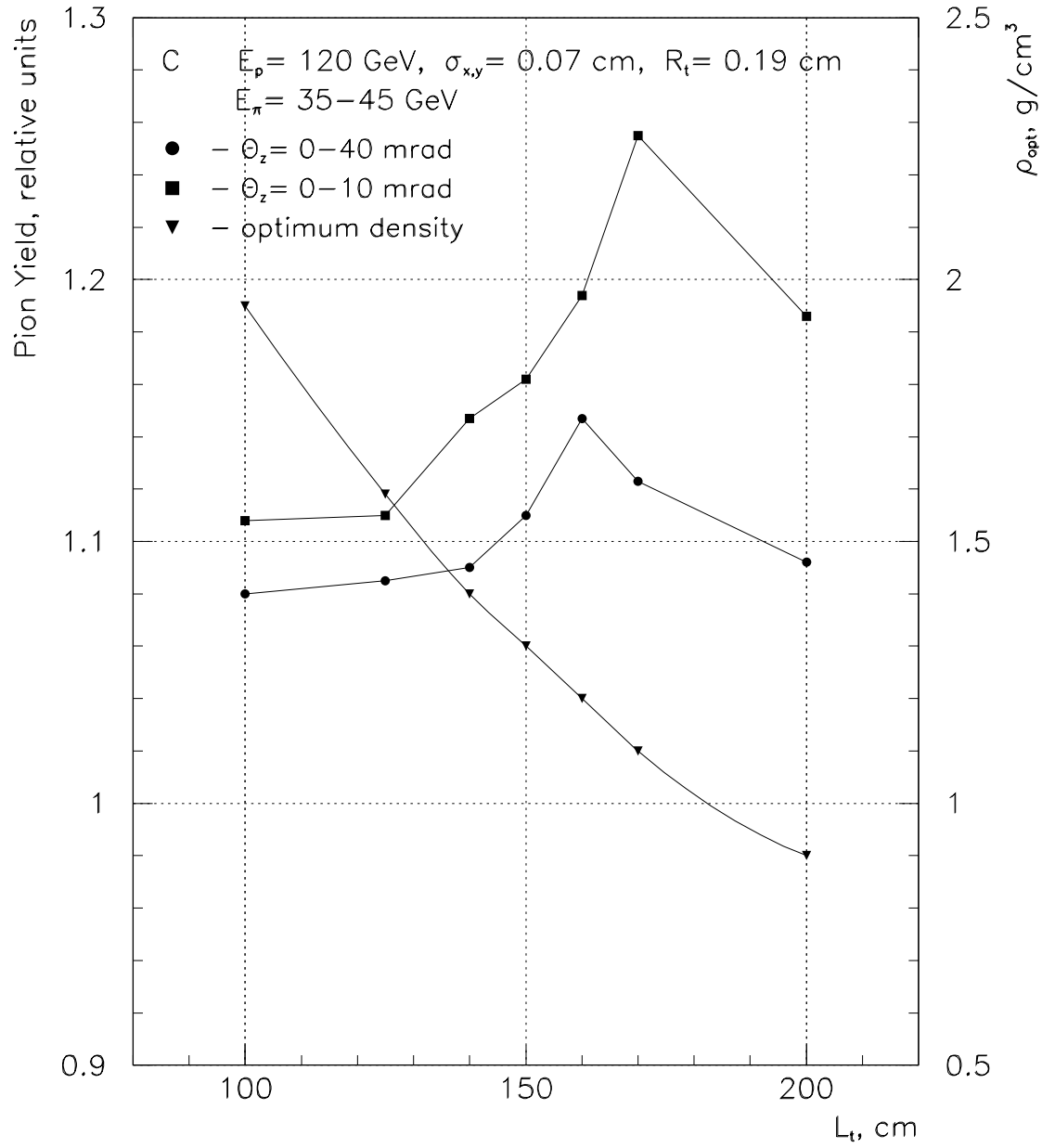


Figure 1.4: The dependences of the optimum graphite density and the pion yield on the target length.

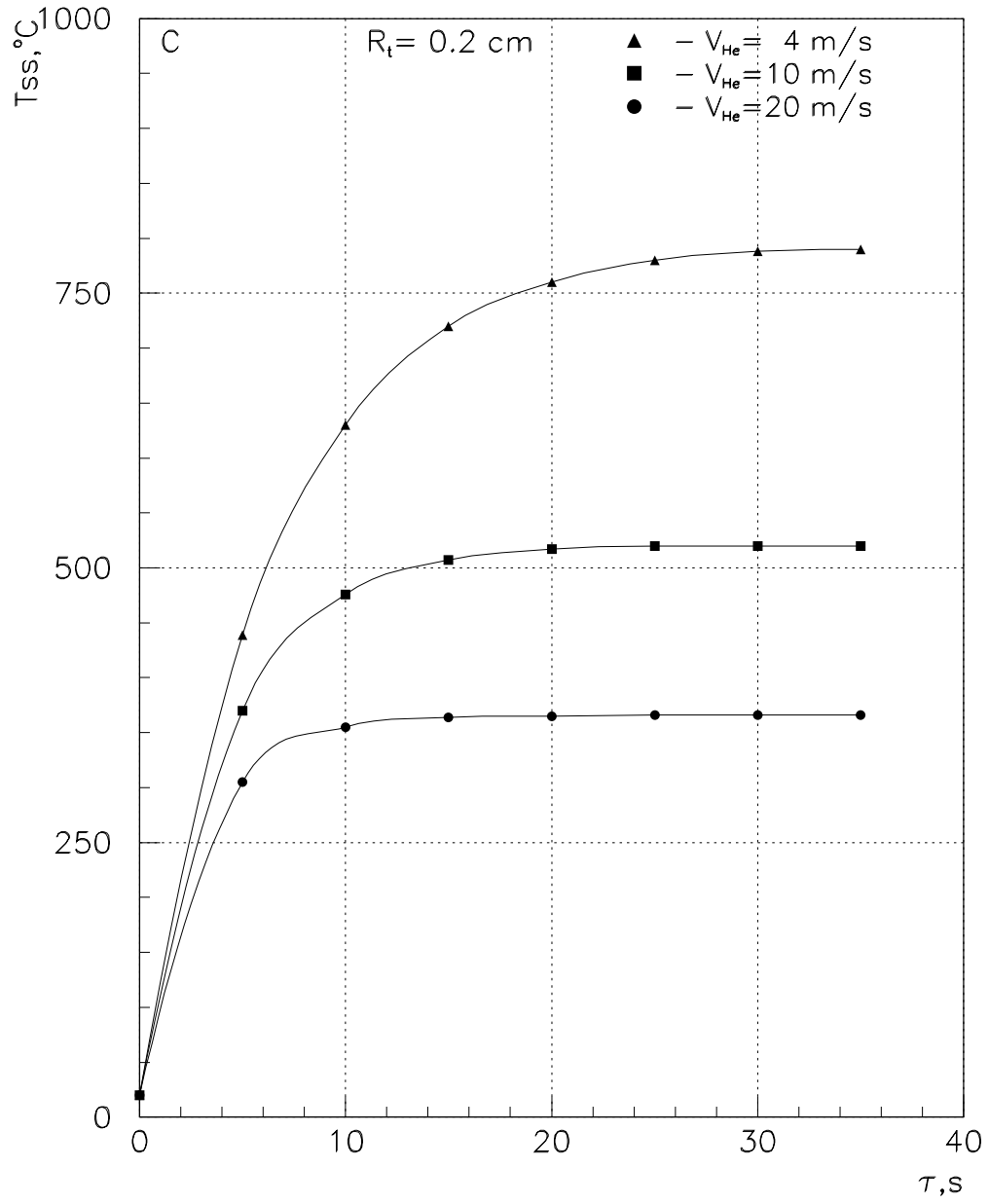


Figure 1.5: The steady-state temperature of the target versus time after beginning of proton spills.

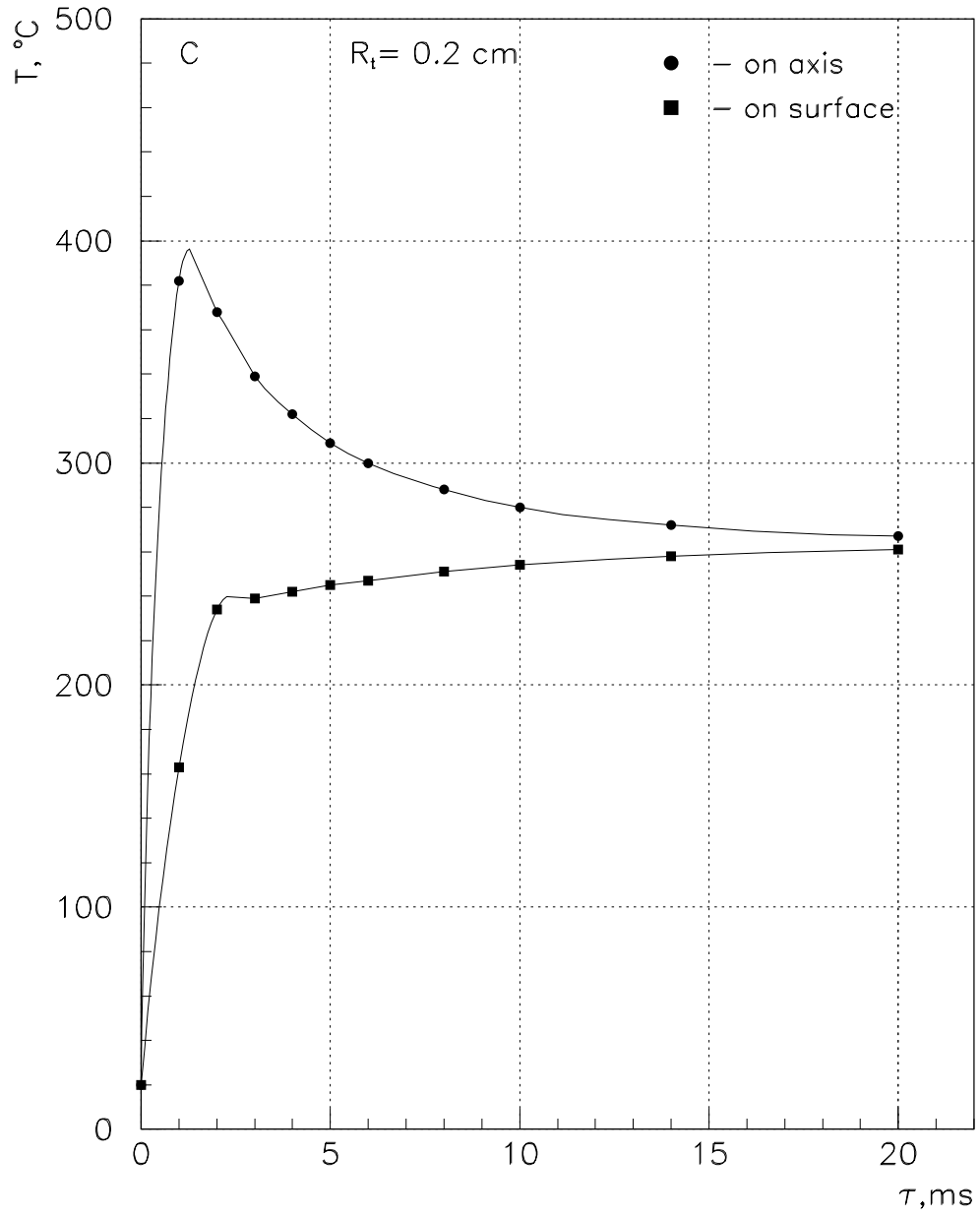


Figure 1.6: The temperature on the axis and surface of a target versus time after a single proton spill.

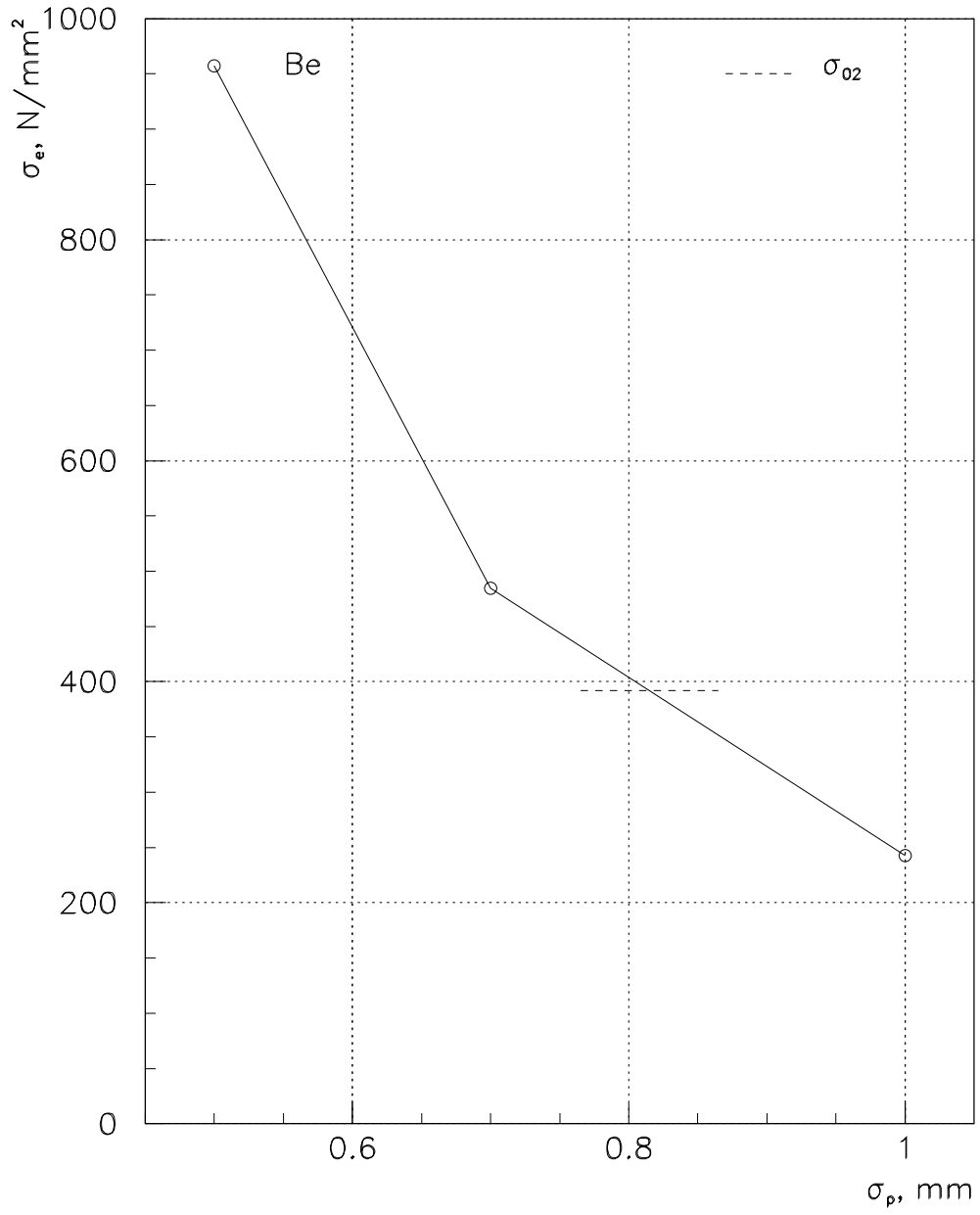


Figure 1.7: The maximum equivalent stress σ_e as a function of the proton beam RMS size σ_p for the beryllium cylindrical target.

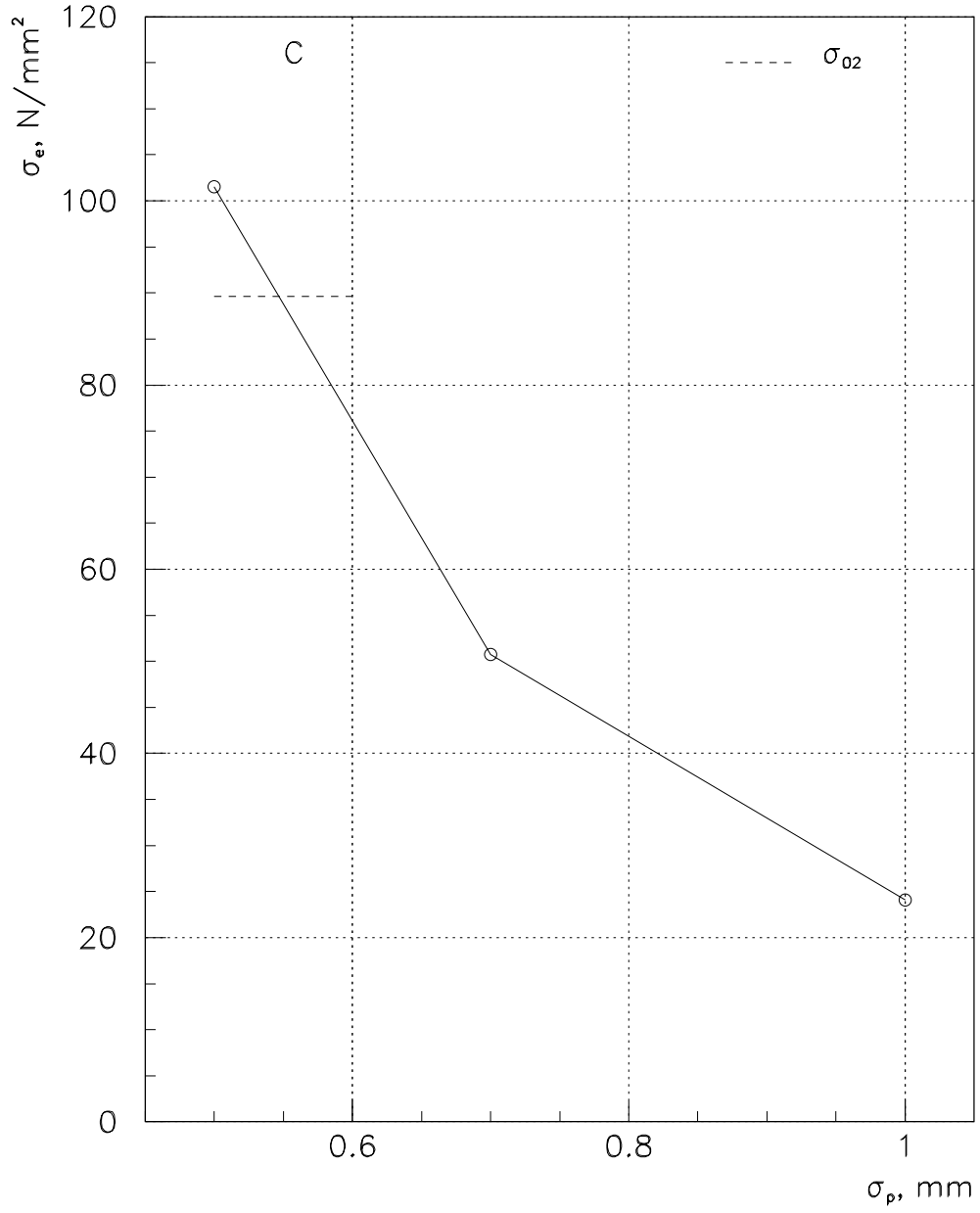


Figure 1.8: The maximum equivalent stress σ_e as a function of the proton beam RMS size σ_p for the graphite cylindrical target.

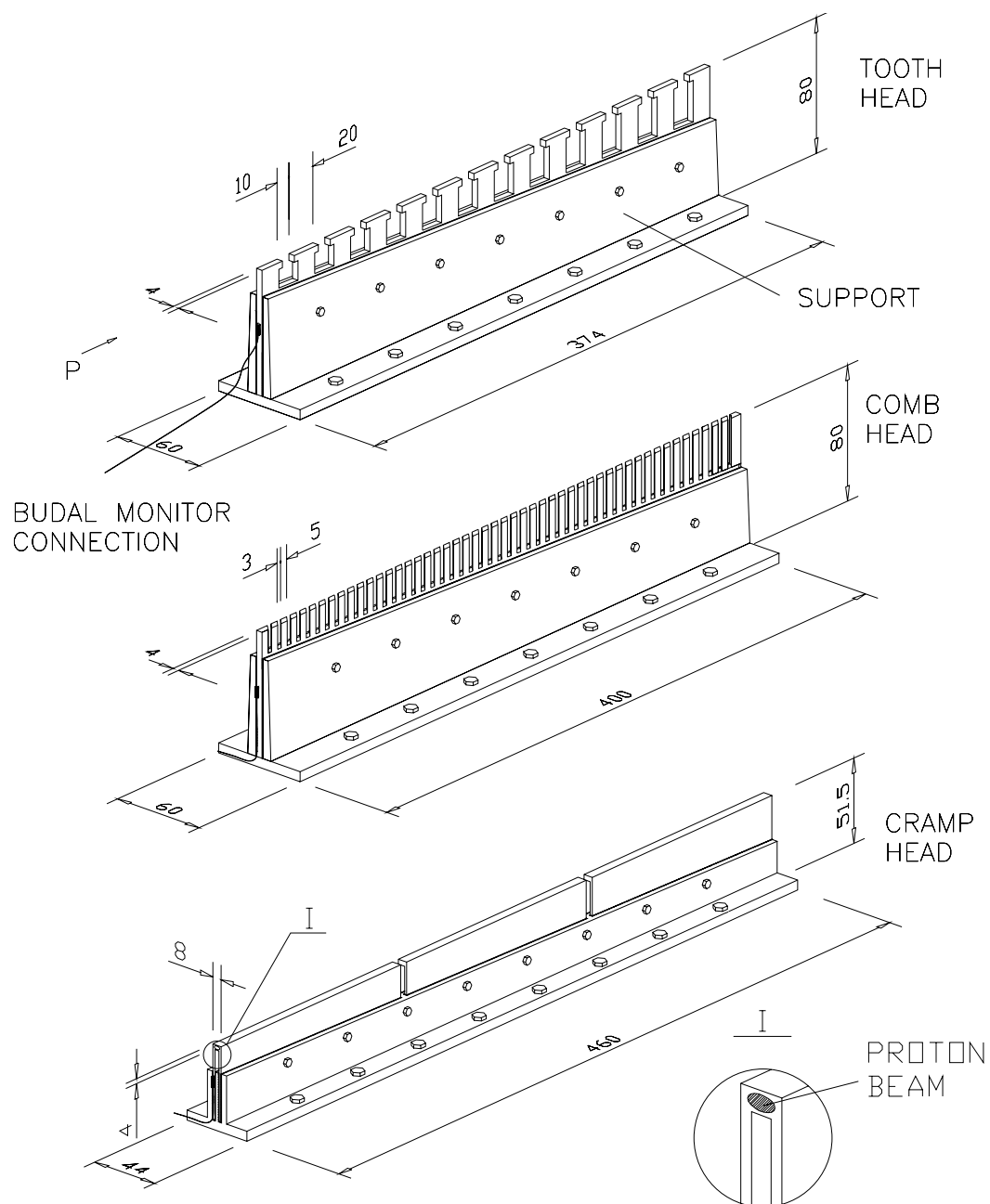


Figure 1.9: Various target heads.

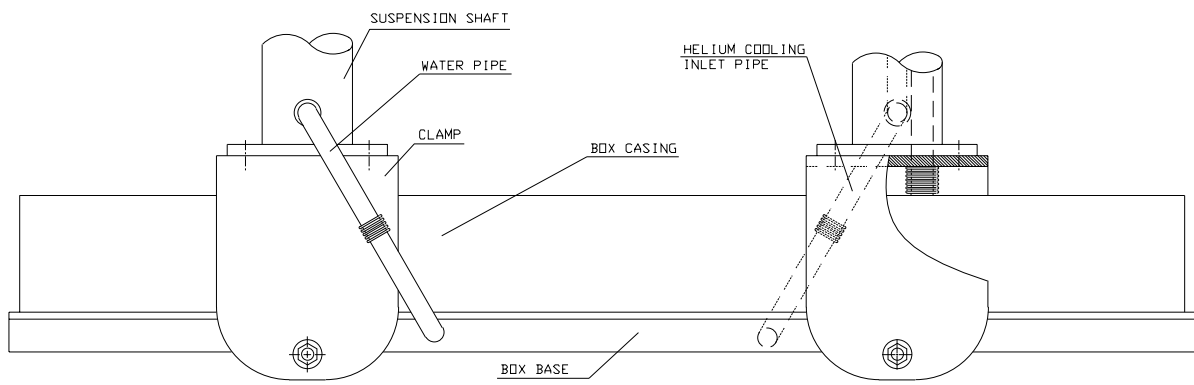


Figure 1.10: The side view of the WBB target box.

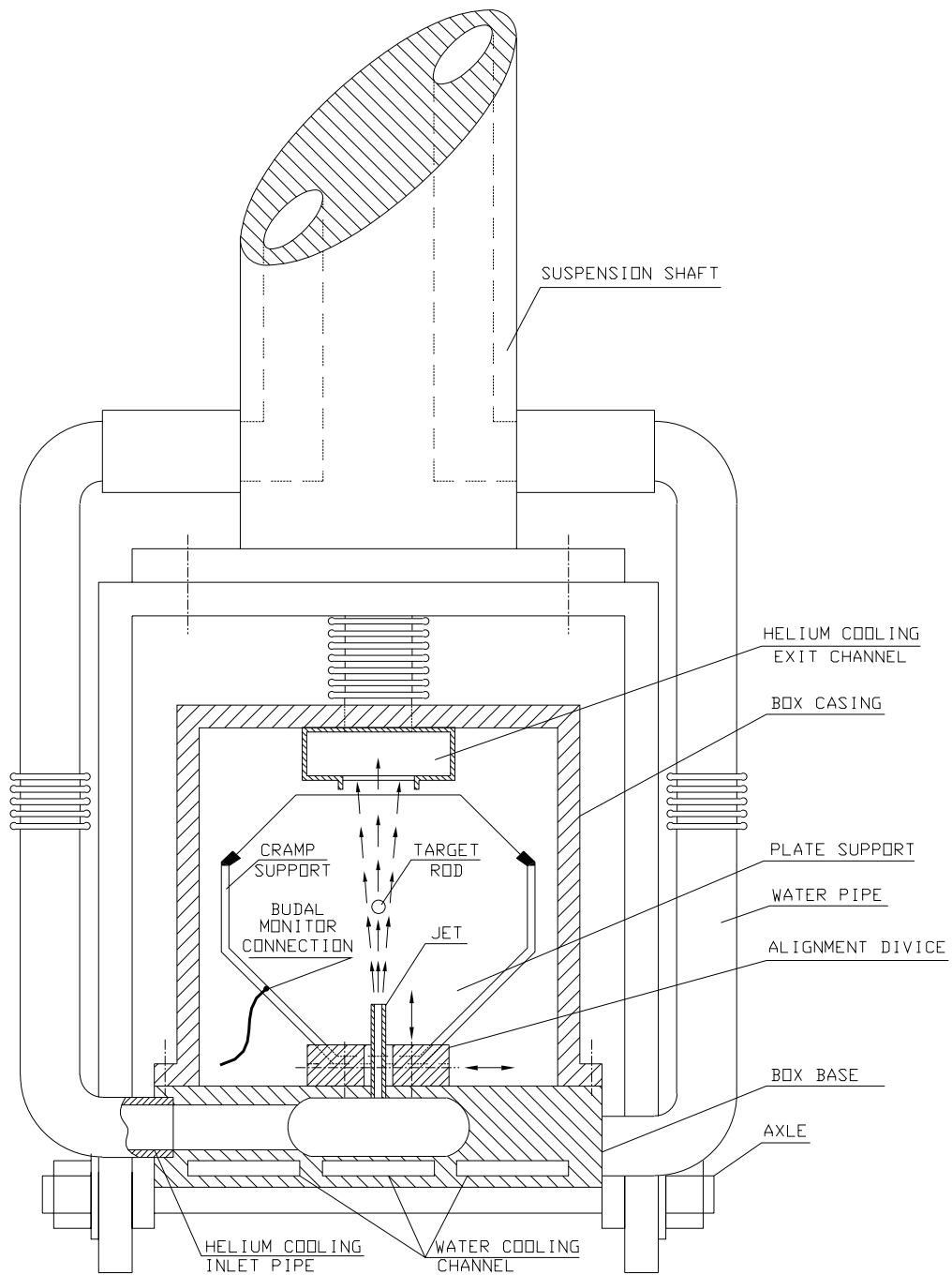


Figure 1.11: Cross-section of the WBB target unit.

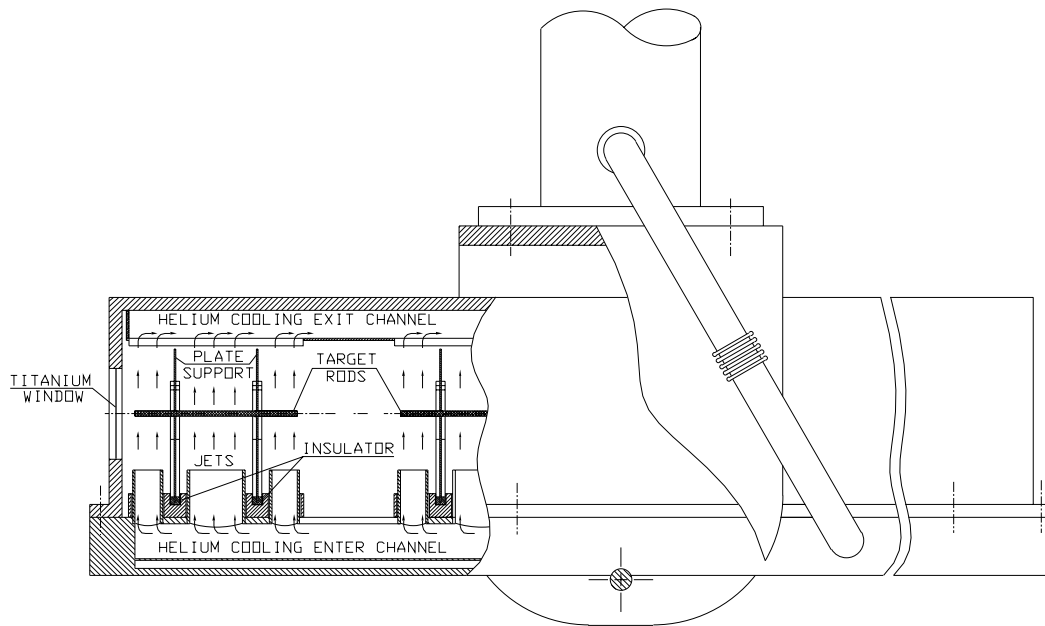


Figure 1.12: Longitudinal section of the WBB target unit.

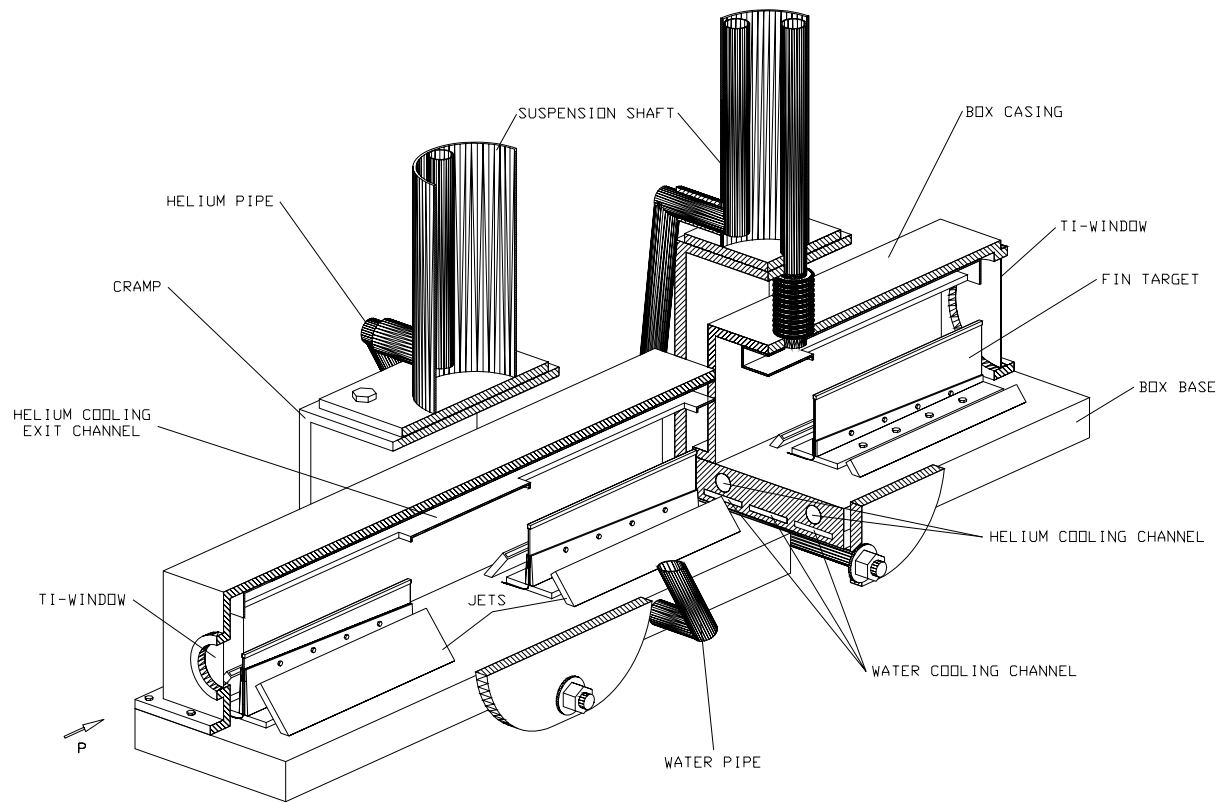


Figure 1.13: The WBB target unit with the segmented fin target.

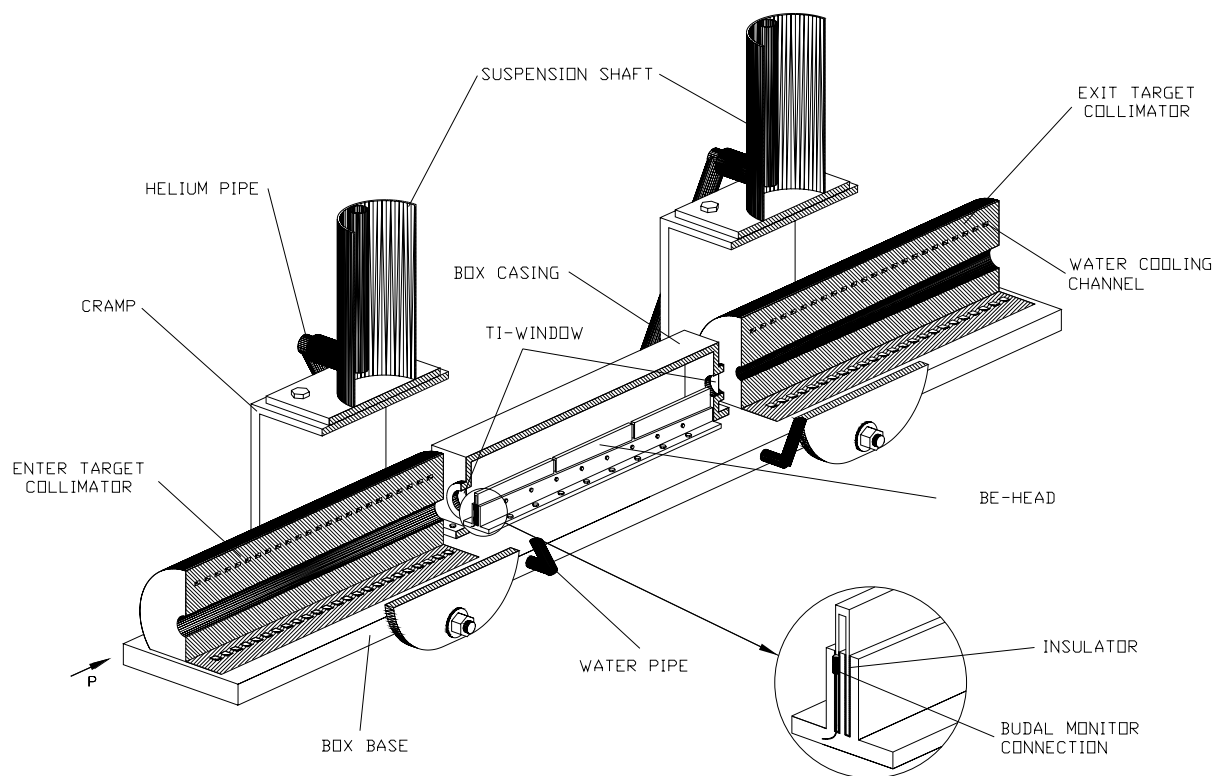


Figure 1.14: The NBB target unit with beryllium cramp-shape head.

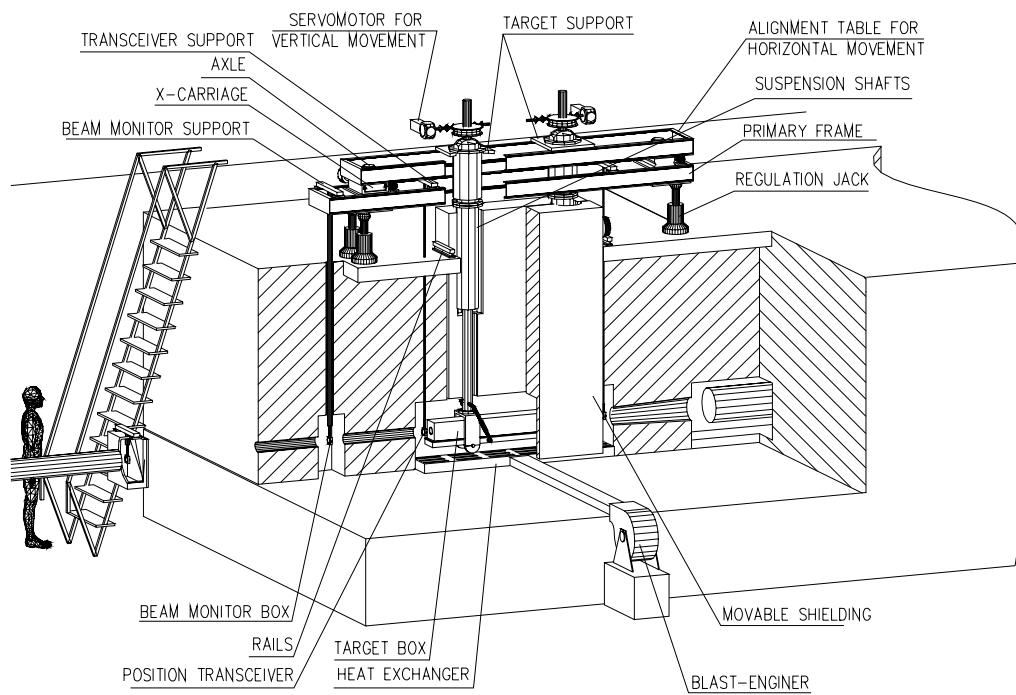


Figure 1.15: General view of the target complex.

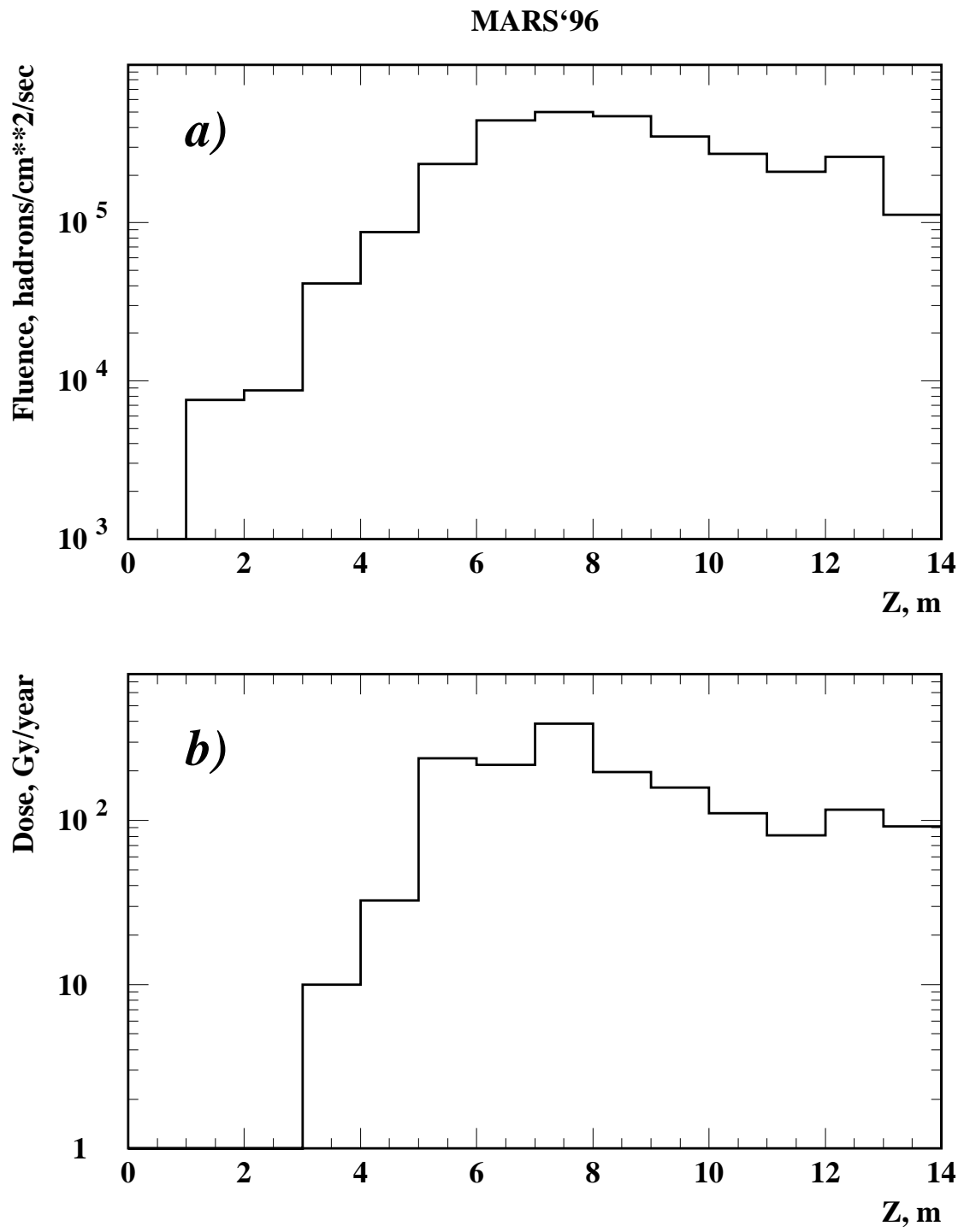


Figure 1.16: The longitudinal distributions over concrete shielding of: a) hadron fluence, b) absorbed dose.

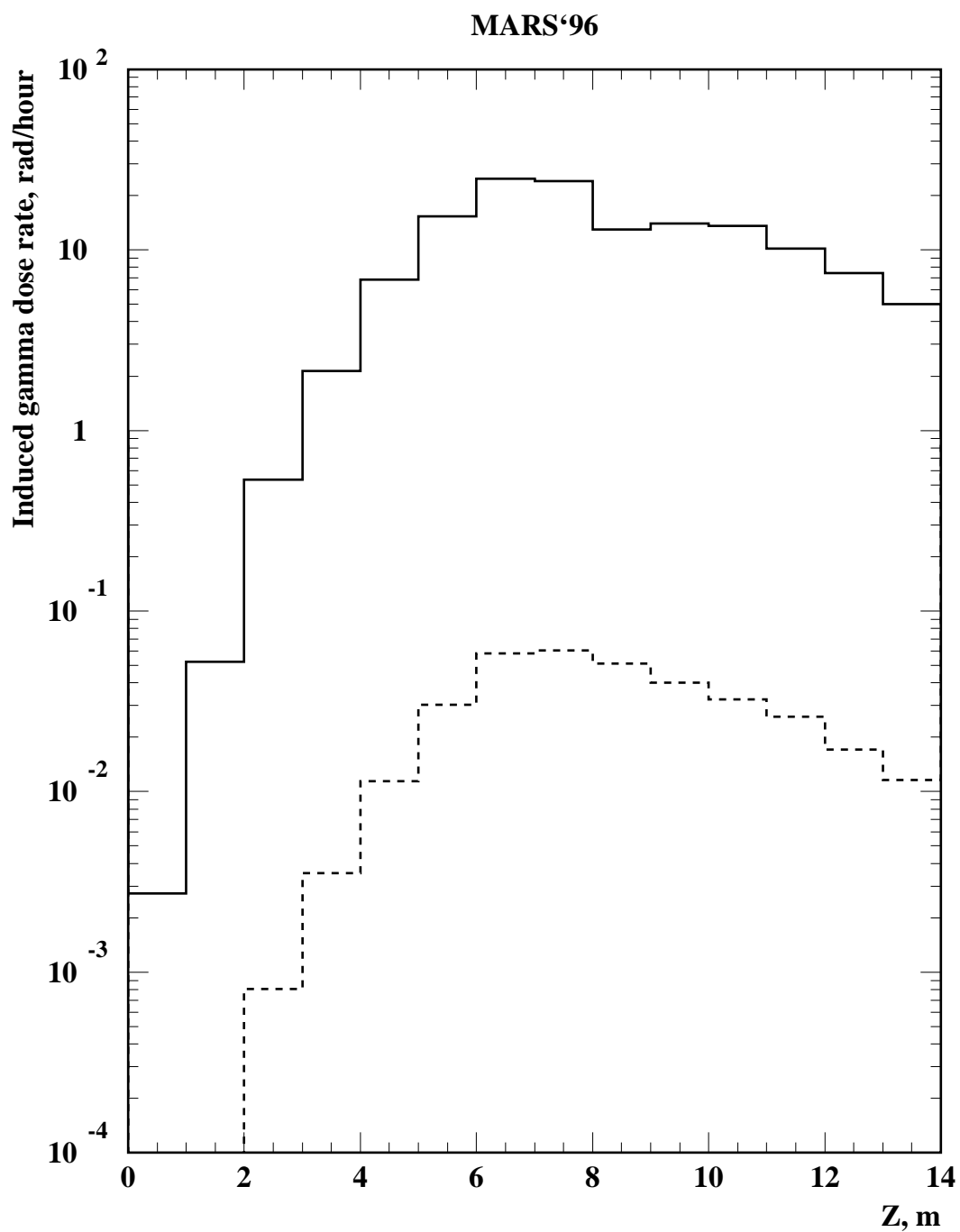


Figure 1.17: Longitudinal distribution of the induced radioactivity levels on internal (solid) and external (dashed) surfaces of iron shielding.

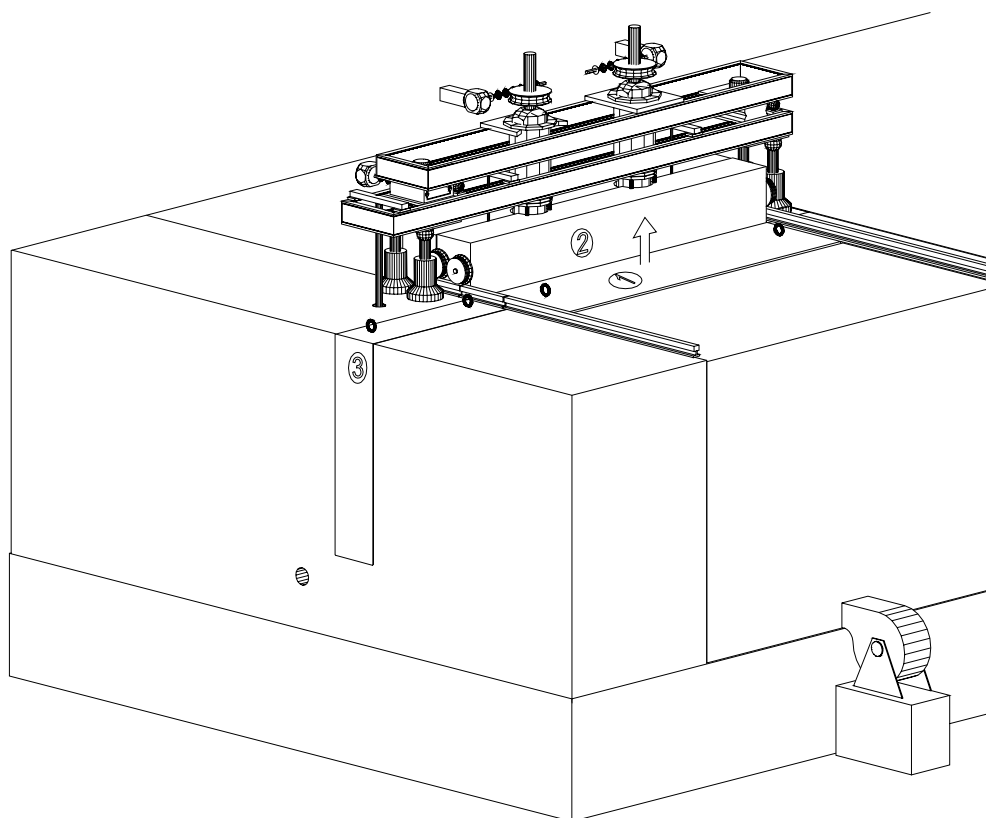


Figure 1.18: Outward view of the shielding and the arrangements at the start state before the target unit removal.

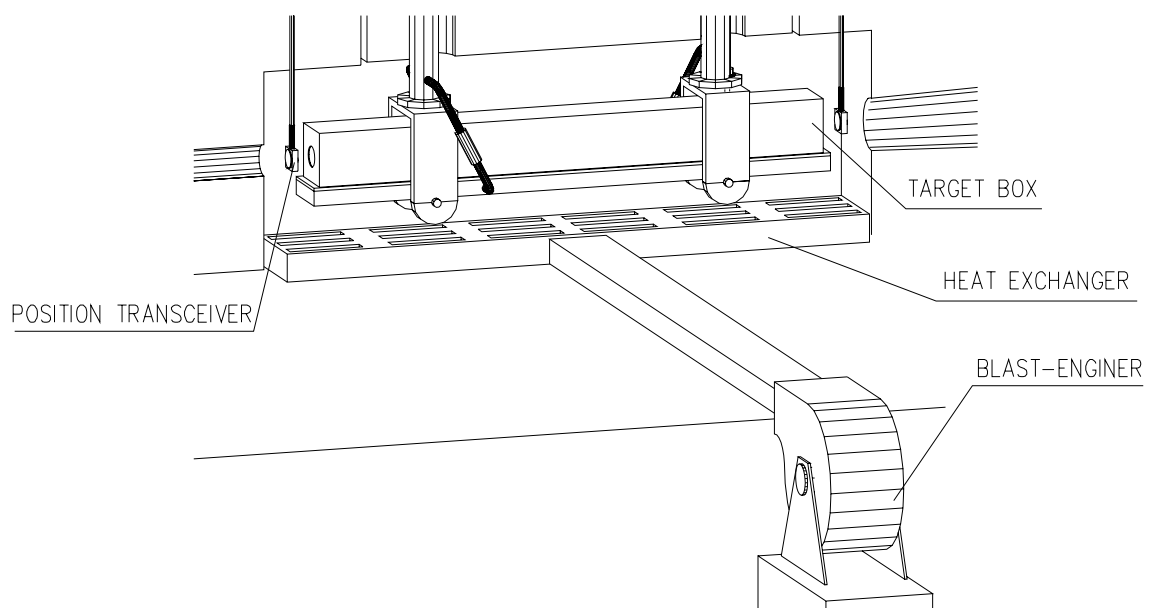


Figure 1.19: Inward view of the "hot zone" of the target station.

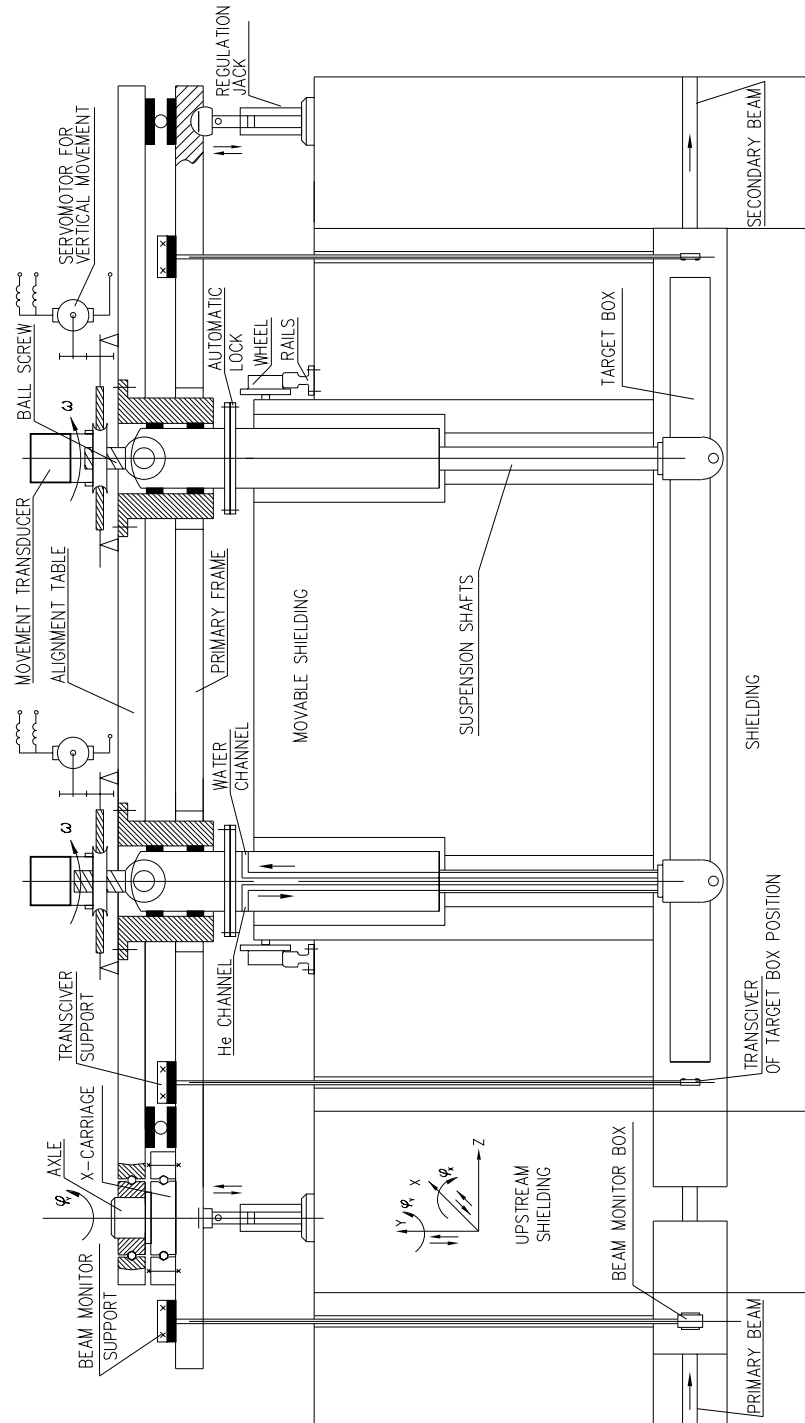


Figure 1.20: A schematic section of the target station.

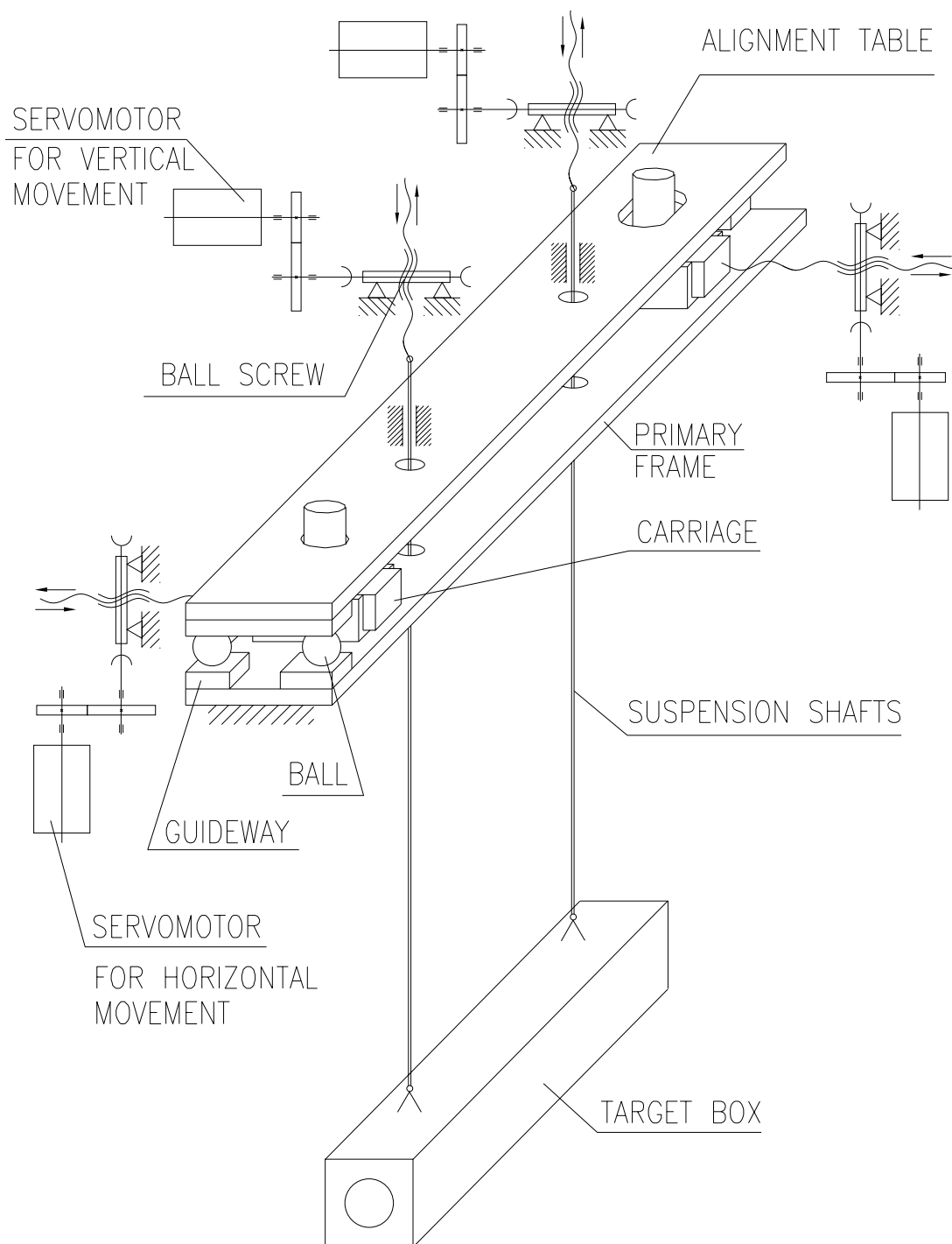


Figure 1.21: Kinematic scheme for displacements of the target box with the upper placed mechanisms.

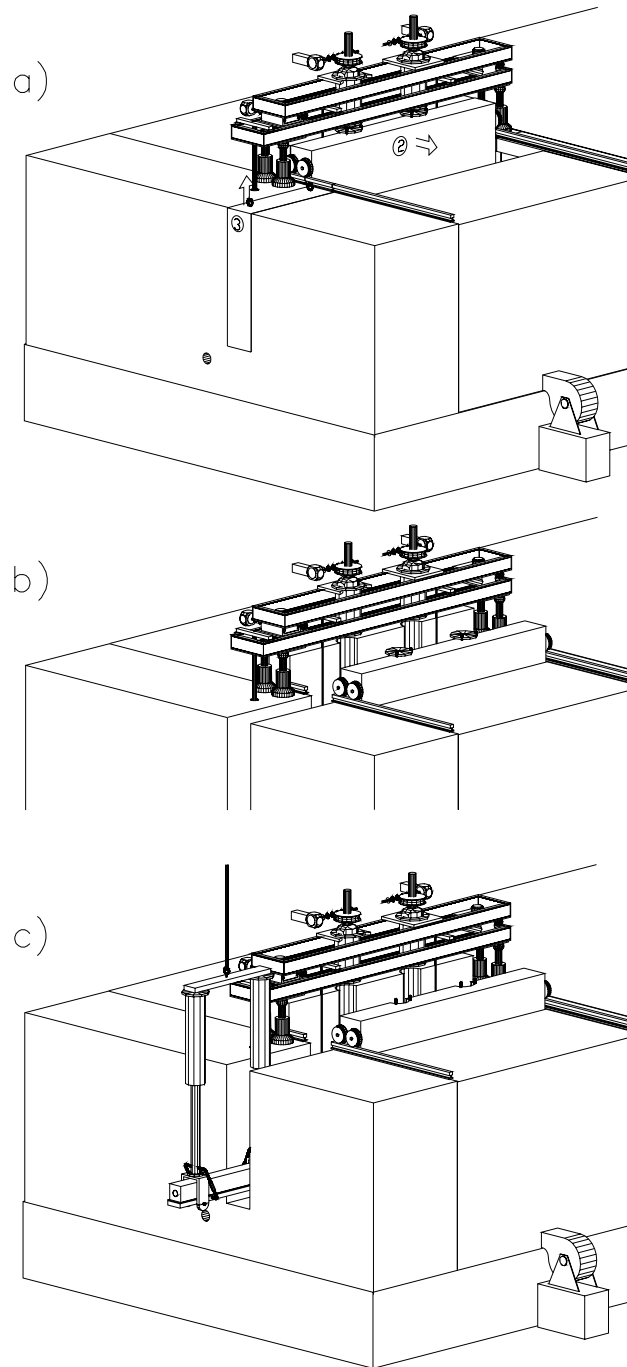


Figure 1.22: The sequential stages of a replacement procedure: a) after the block 1 removal; b) after the block 3 removal; c) removing of the target unit.

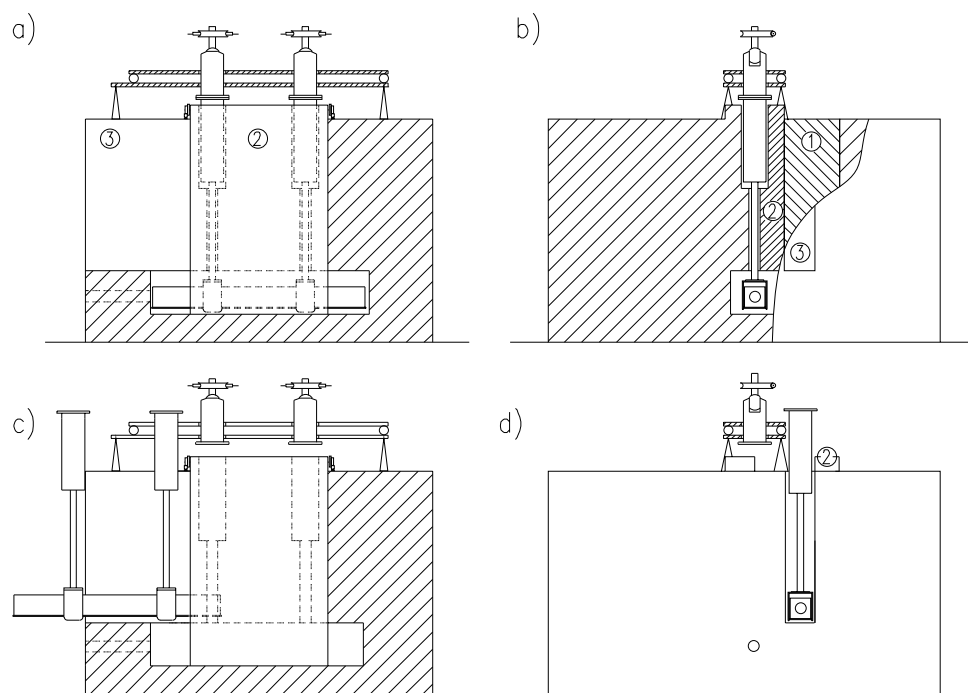


Figure 1.23: The target unit position during removing.

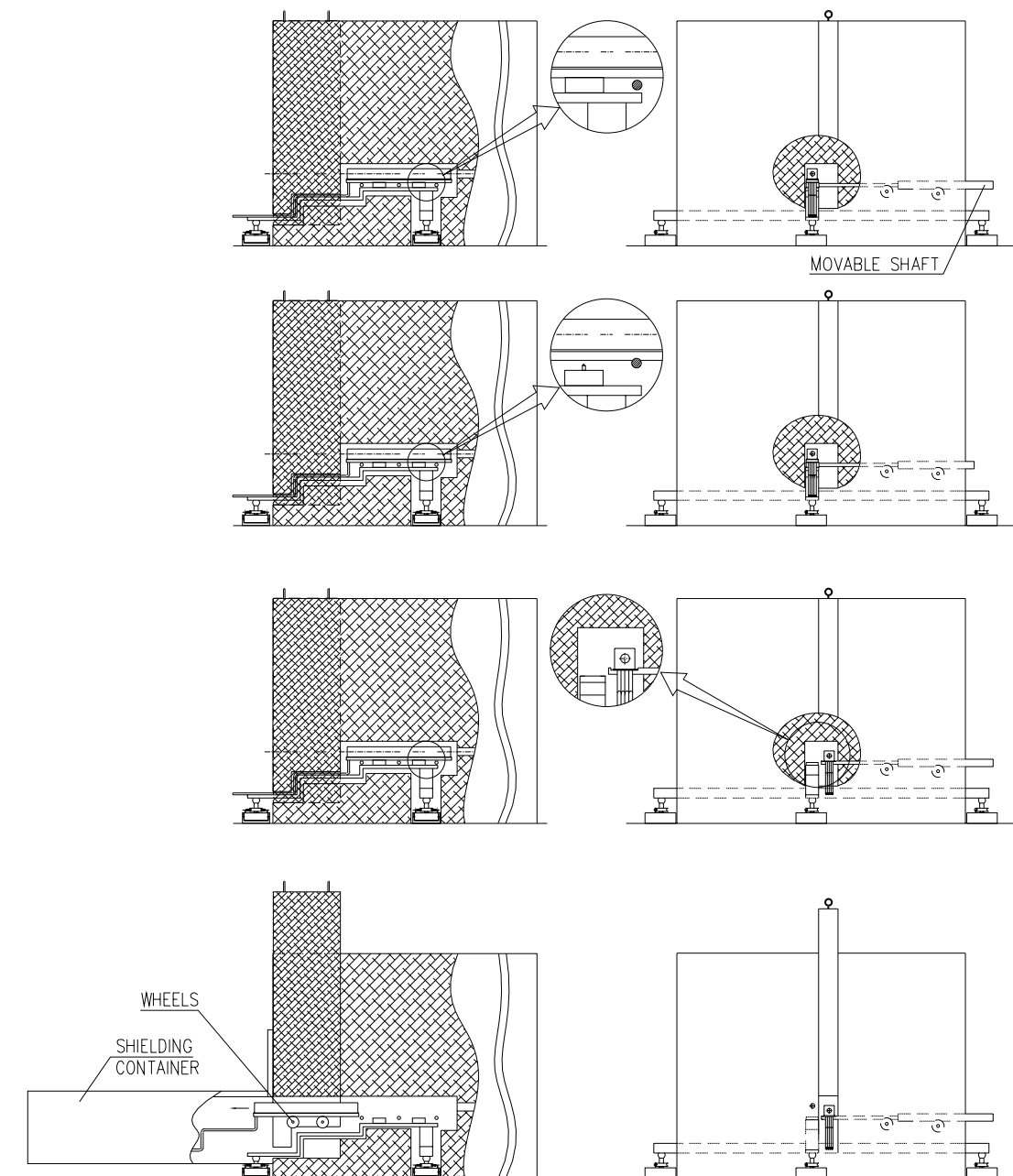


Figure 1.24: The sequential stages of the removal of the target unit with lower placed mechanisms.

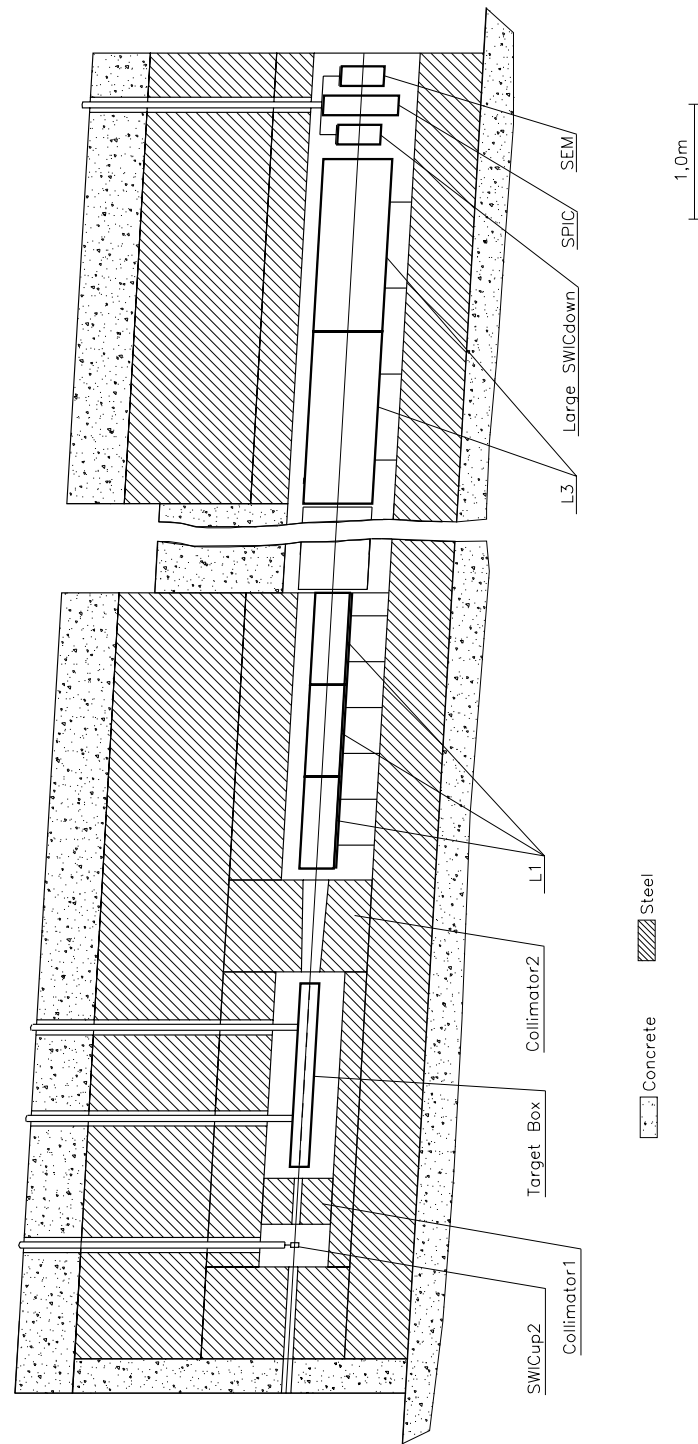


Figure 1.25: The layout of the WBB.

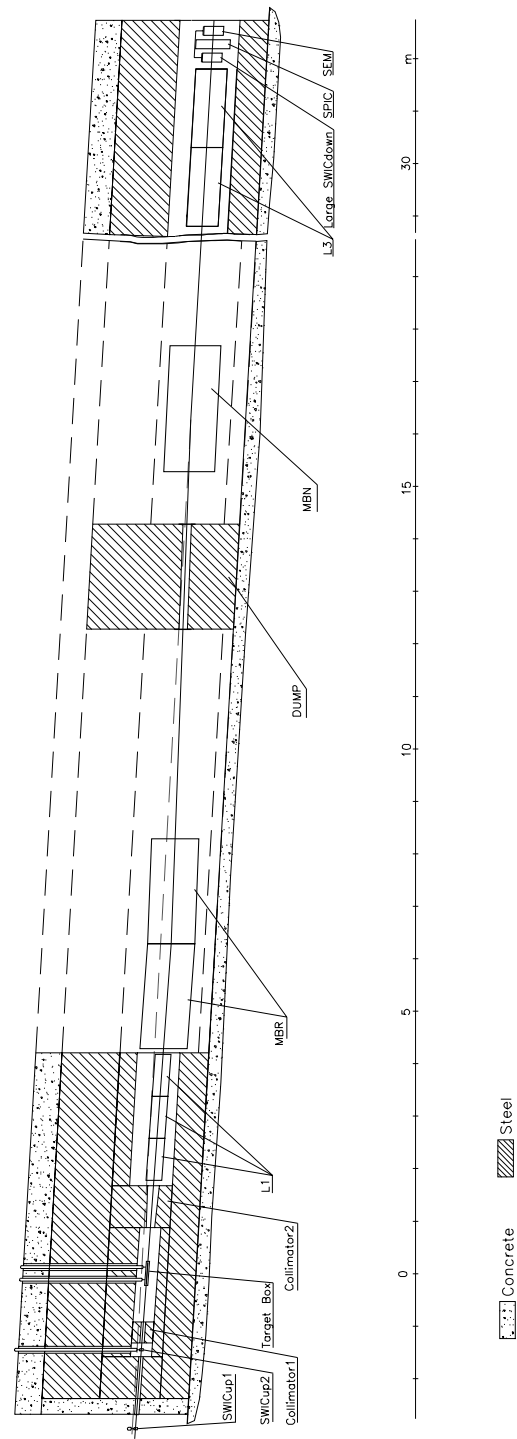


Figure 1.26: The layout of the NBB with parabolic lenses.

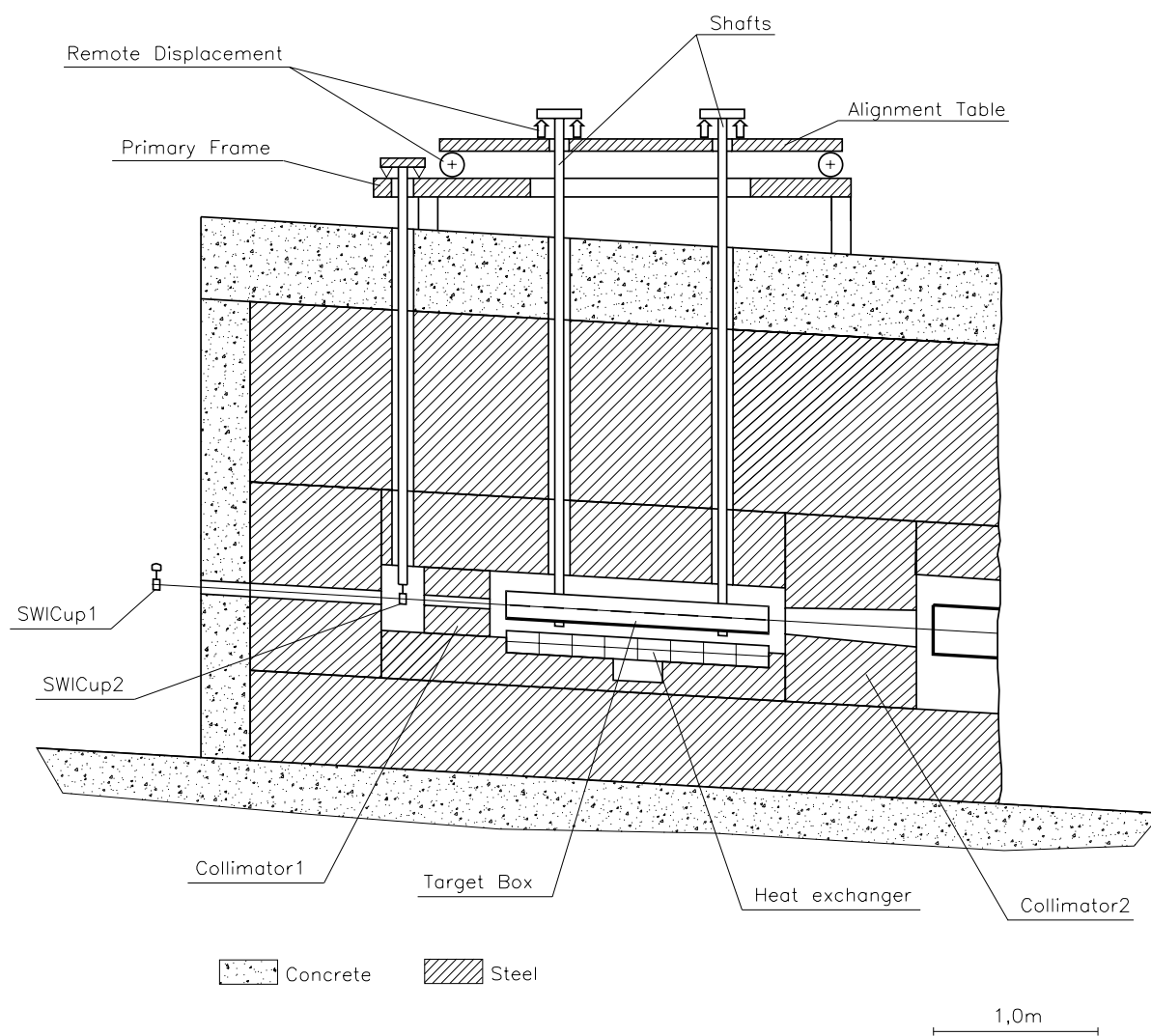


Figure 1.27: The layout of the WBB target station.

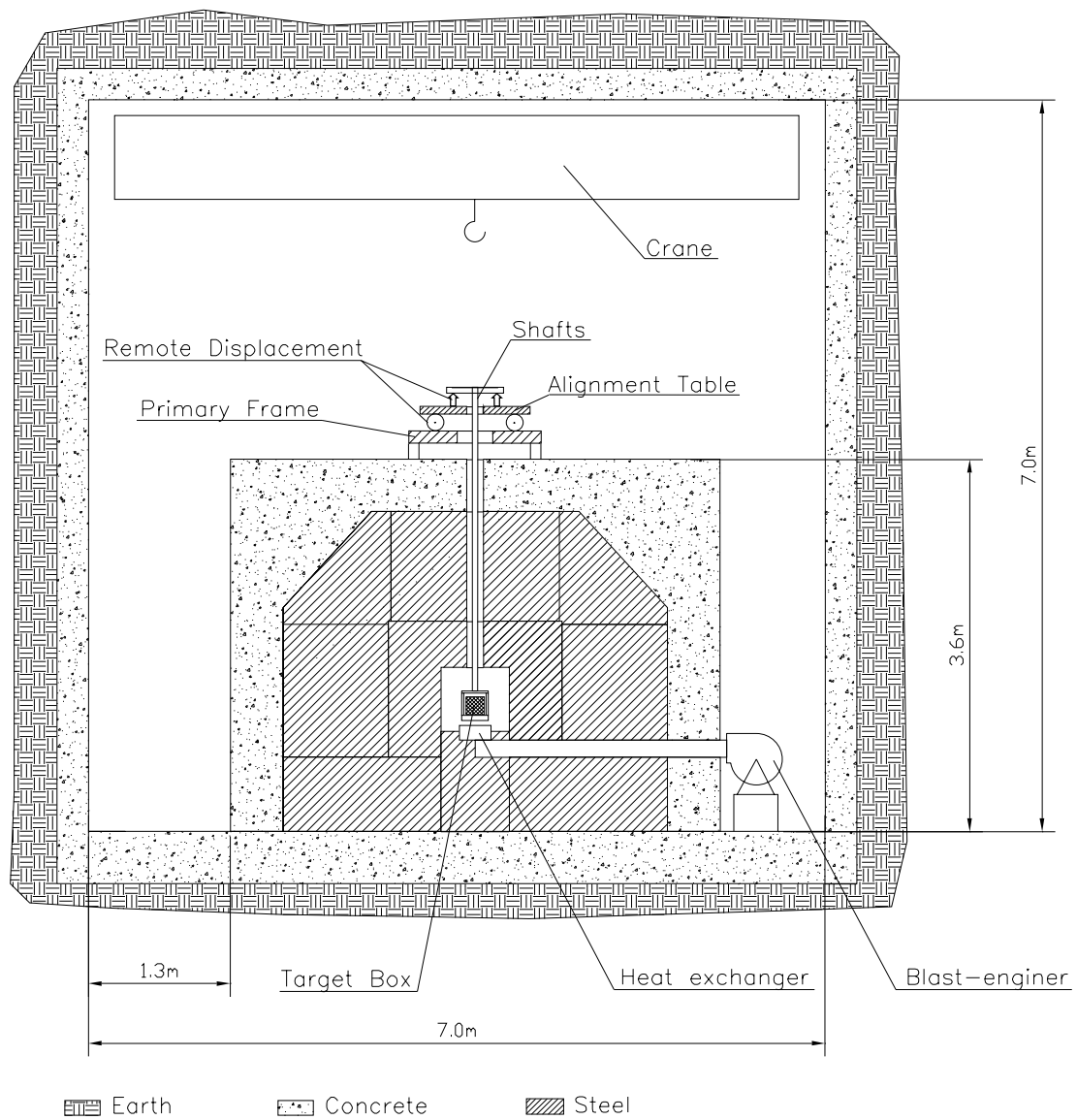


Figure 1.28: Cross-section of the target station.

2 NuMI Neutrino Beams using the Parabolic Horn (Lens) Focusing System

The possible variants of the NuMI wide band and narrow band beams with parabolic lens focusing systems have been discussed in Task A and B Report of the IHEP [1]. Table 2.1 of the Report mentioned above gives the main geometrical dimensions of the existing parabolic lenses L1, L2 and L3, which have been used to design the focusing system for both WBB and NBB. The main geometrical dimensions of the proposed new parabolic lens LX are given in Table 3.1 of this Report.

2.1 Wide Band Neutrino Beam

The neutrino beam parameters for the focusing system with three L1 and two L3 (3L1/2L3) compared with those for the Fermilab three horn focusing system H6.6 have been given in the previous IHEP Report.

As follows from the recent results of the beam simulations in Fermilab, the usage of the magnetic field of a straight wire carrying a given current on the decay pipe axis (ADP or "Hadron Hose") improves the WBB parameters significantly. Below the parameters of the neutrino beam in the presence of ADP compared with those without ADP are given for three different WBB designs:

- Fermilab three horn focusing system H6.6;
- parabolic lens 3L1/2L3 focusing system;
- parabolic lens 2LX/2L3 focusing system.

A schematic layout for the 3L1/2L3 focusing system is given in Figure 2.1. A schematic layout for the 2LX/2L3 focusing system is similar to the 3L1/2L3 ones; the currents in both sets of lenses are equal to 320 kA.

All WBB designs use a two nuclear interaction length segmented carbon target with radius of 0.2 cm, described in [3]. The proton beam RMS size is equal to 0.1 cm. The neutrino event rates have been calculated using M.C. program HALO.

Figures 2.2, 2.4 and 2.6 show the neutrino spectra at the far detector for H6.6, 3L1/2L3 and 2LX/2L3 focusing systems respectively, calculated for wire current of 1.0 kA (the wire radius is equal to 0.15 cm), 0.5 kA

(the wire radius is equal to 0.10 cm) and without ADP. The Far/Near ratio calculated for the same values of ADP currents is given in Figures 2.3, 2.5 and 2.7 respectively. The total neutrino event rates for all focusing systems are shown in Table 2.1.

Focusing system	Without ADP	I=0.5 kA r=0.10 cm	I=1.0 kA r=0.15 cm
H6.6	3144	3122	2746
3L1/2L3	2829	3046	2719
2LX/2L3	3034	3191	2883

Table 2.1: The total neutrino event rates at the far detector.

One should note that in the case of wire current 0.5 kA the total neutrino event rates for the parabolic lens focusing systems 3L1/2L3 and 2LX/2L3 are greater than those without ADP and decrease with further rise of the ADP current. Moreover, the Far/Near ratio for these focusing systems does not change significantly for the currents greater than 0.5 kA. It looks that the wire current 0.5 kA is sufficient one for the parabolic lens focusing systems.

2.2 Narrow Band Neutrino Beam

As follows from the previous IHEP Report, the same parabolic lenses can be used for creation of the NBB focusing system. Below the parameters of the neutrino beam are given for two NBB designs, which differ only by the first focusing device: 3L1/2B/2L3 and 2LX/2B/2L3 focusing systems.

The proposed focusing systems provide the neutrino beams from hadron beams with the momenta from 20 up to 45 GeV/c. The tuning to various momenta can be done by changing the currents in parabolic lenses and dipoles, while keeping the target and all equipment at fixed positions.

A schematic layout for the 3L1/2B/2L3 focusing system is given in Figure 2.8. A schematic layout for the 2LX/2B/2L3 focusing system is similar to the 3L1/2B/2L3 ones; the currents in both sets of lenses I_1/I_2 are equal to 320/320 kA for 20 and 45 GeV tunes and 320/190 kA for 30 GeV tune.

The 3L1/2B/2L3 and 2LX/2B/2L3 NBB designs are completely compatible with the corresponding 3L1/2L3 and 2LX/2L3 WBB designs and allow a simple change between WBB and NBB, in particular:

- one may exclude any repositioning of the primary proton beam-line equipment;
- focusing devices 3L1 (or 2LX) and 2L3 remain on their longitudinal positions (first device must be shifted by about 15 cm in transverse direction);
- the proton beam dump for the NBB design does not disturb the WBB and may be installed before the beginning of neutrino beams operation.

The most important positive feature of these NBB designs is the usage of the same focusing devices and the same power supply circuits as for the WBB designs.

Both NBB designs use a one nuclear interaction length carbon or beryllium target with radius of 0.2 cm. The proton beam RMS size is equal to 0.1 cm. The neutrino fluxes have been calculated using the Fermilab beam simulation package GNUMI.

There is no principal difference between the focusing properties of both parabolic lens NBB designs. Figure 2.9 and 2.10 show the neutrino spectra for the 3L1/2B/2L3 and 2LX/2B/2L3 focusing systems at 45 GeV tune. As follows from these beam simulations, the ratio of the neutrino events with $E < 10$ GeV to the total number of neutrino events is equal to 0.36% for 3L1/2B/2L3 and 0.38% for 2LX/2B/2L3 focusing systems. The total event rates are equal to 740 and 770 events/kTon-yr respectively.

WBB. $3*L1/2*L3$ Focusing System.

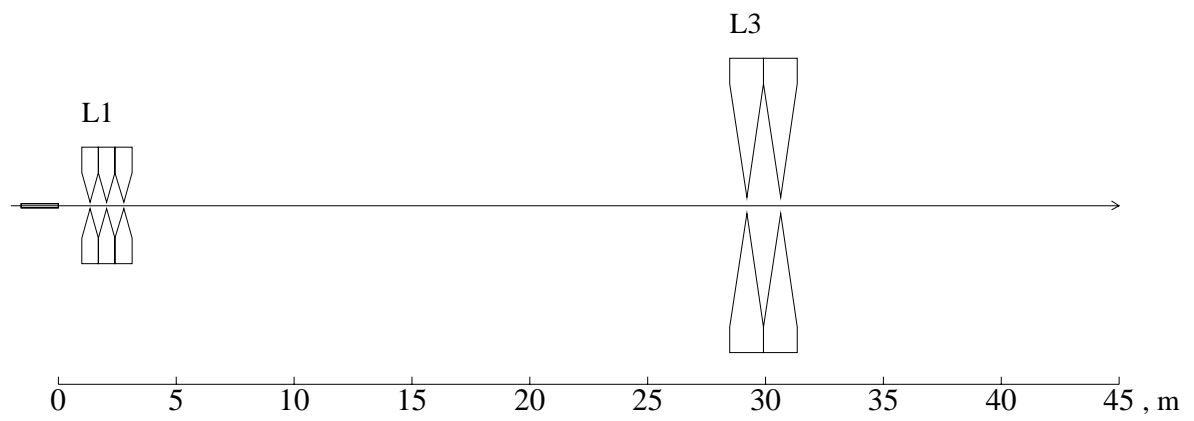


Figure 2.1: The layout of the $3L1/2L3$ focusing system for the WBB.

WBB. Far Detector NuMu Event Rate.

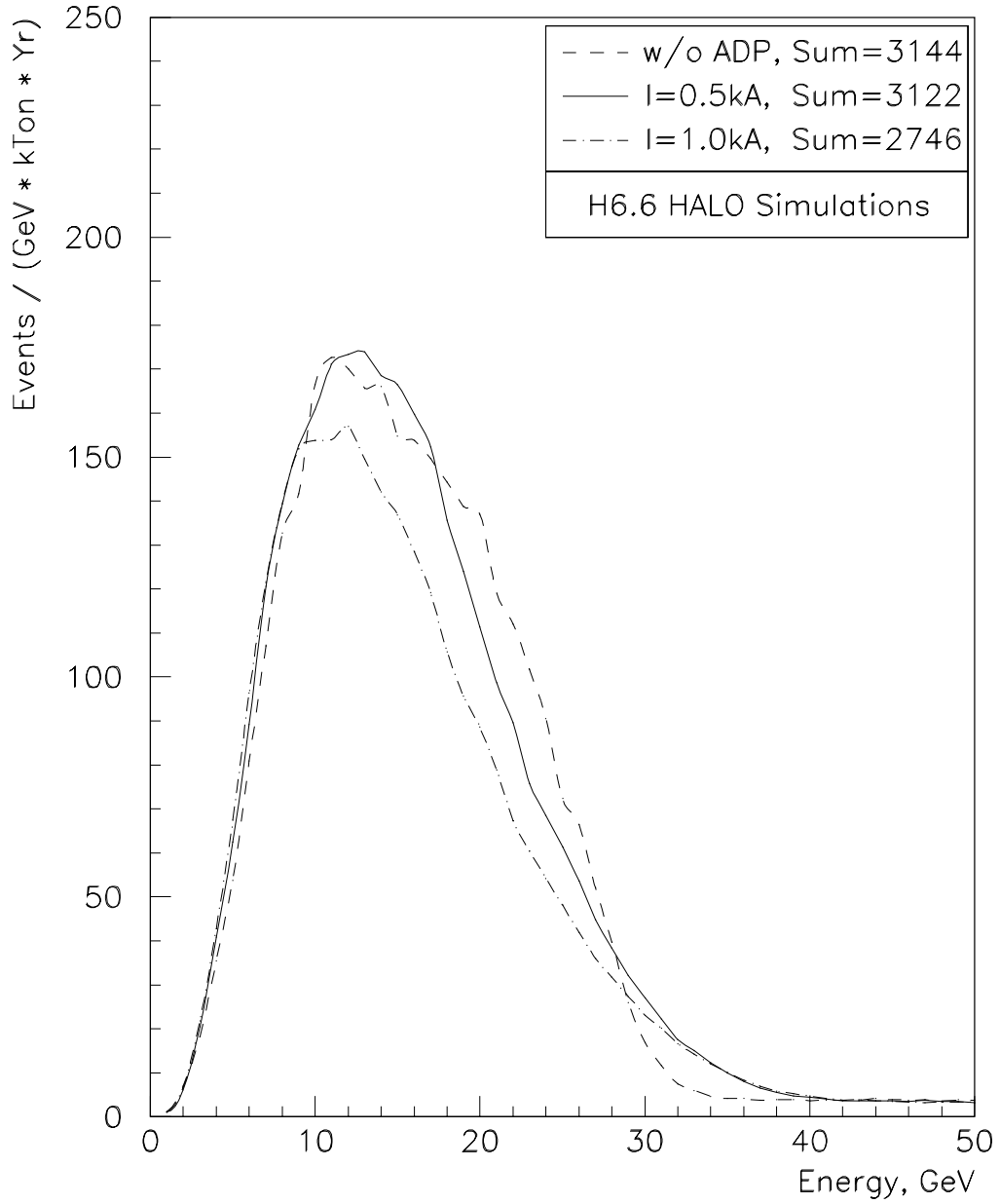


Figure 2.2: The ν_μ event rate for the H6.6 focusing systems with the different wire currents.

WBB. Far / Near NuMu Event Rate Ratio.

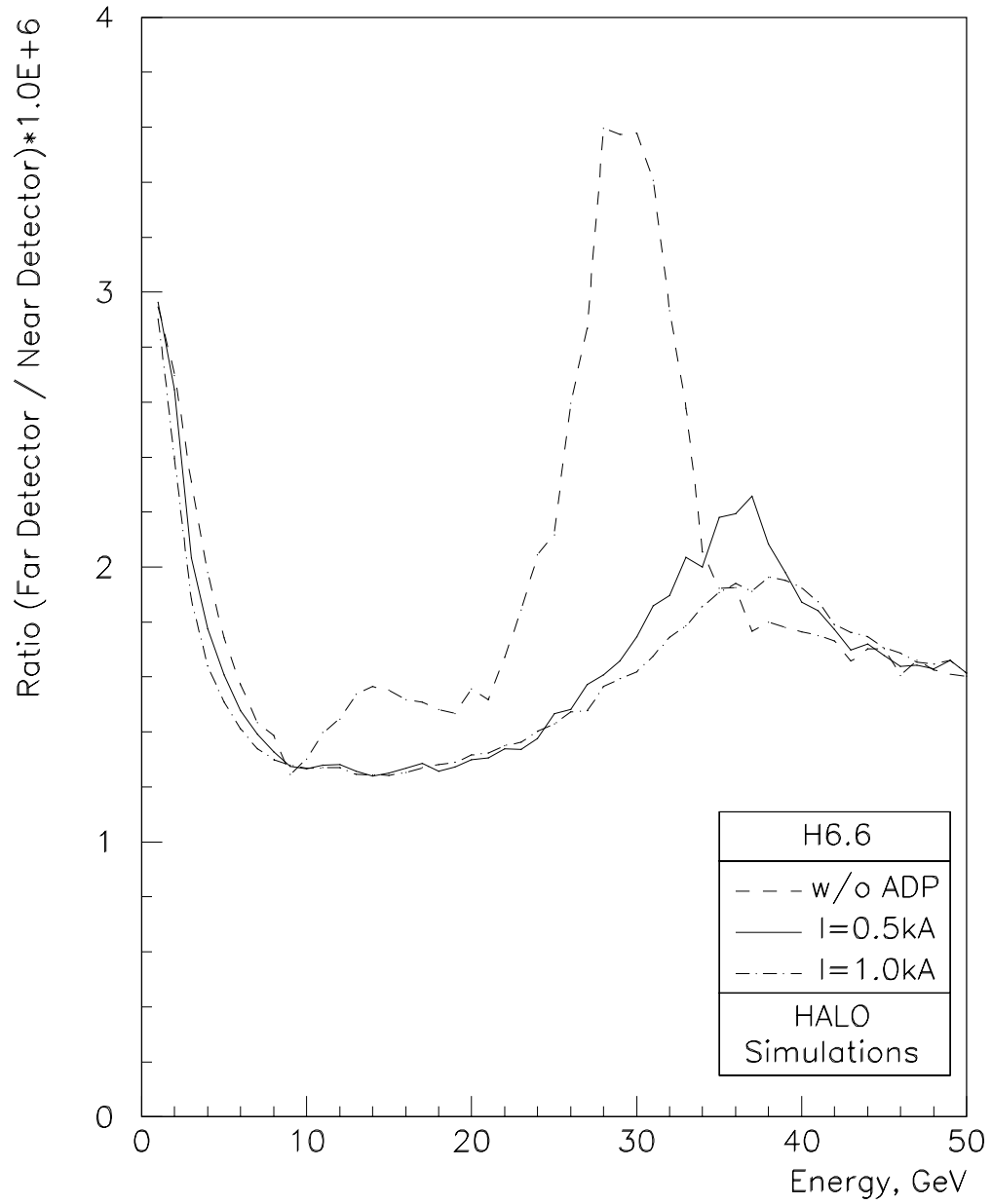


Figure 2.3: The Far/Near ratio for the H6.6 focusing systems with the different wire currents.

WBB. Far Detector NuMu Event Rate.

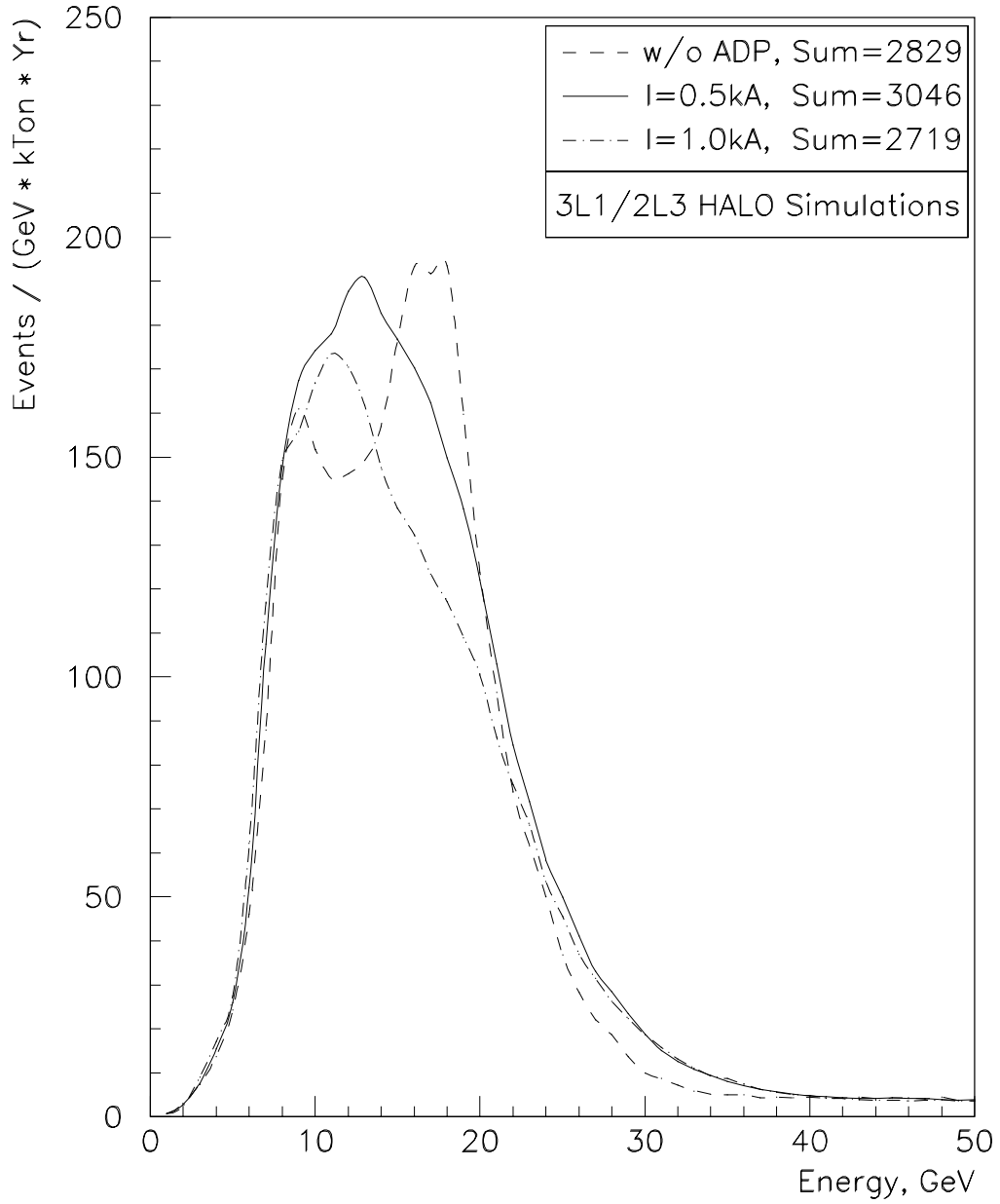


Figure 2.4: The ν_μ event rate for the 3L1/2L3 focusing systems with the different wire currents.

WBB. Far / Near NuMu Event Rate Ratio.

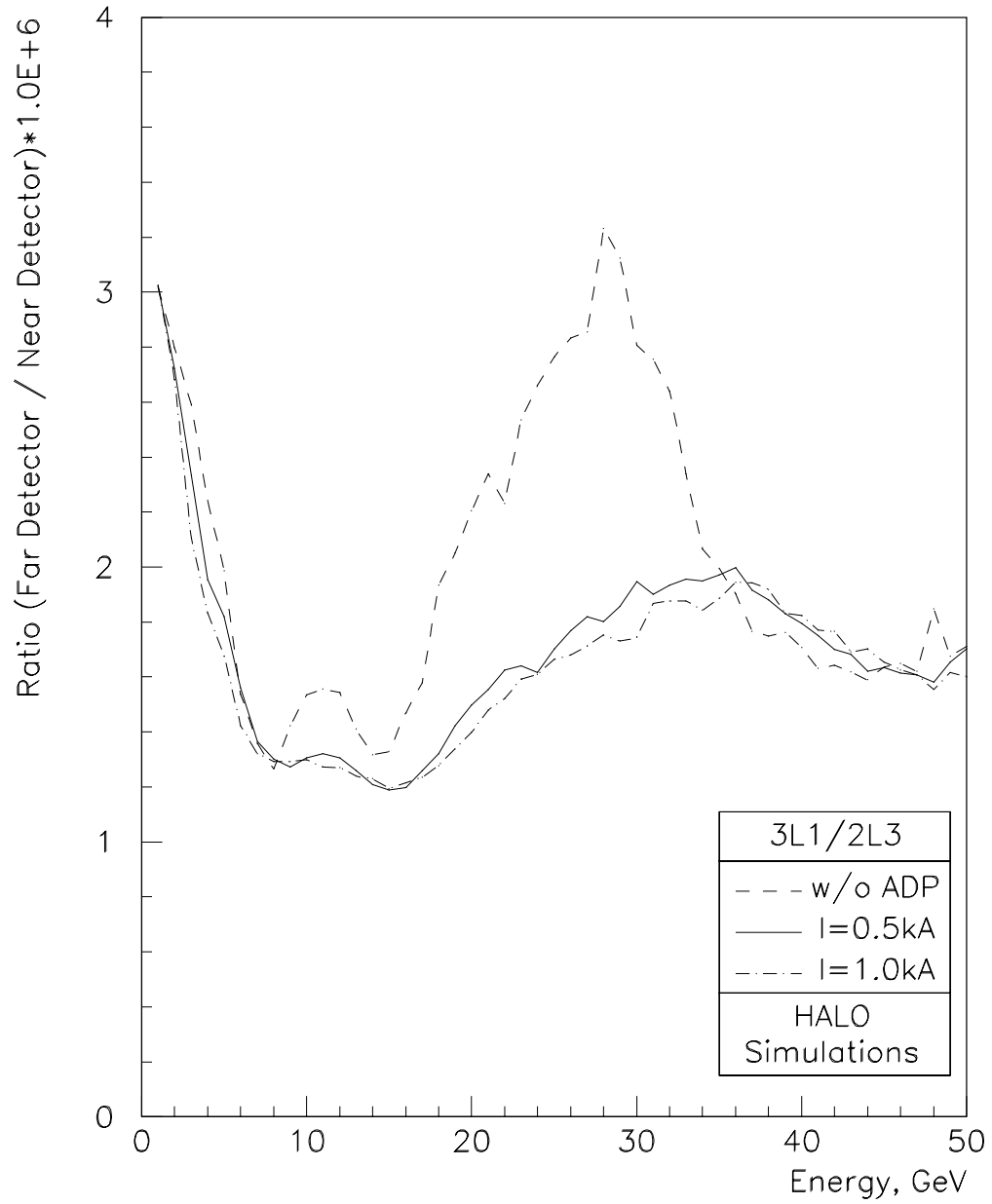


Figure 2.5: The Far/Near ratio for the 3L1/2L3 focusing systems with the different wire currents.

WBB. Far Detector NuMu Event Rate.

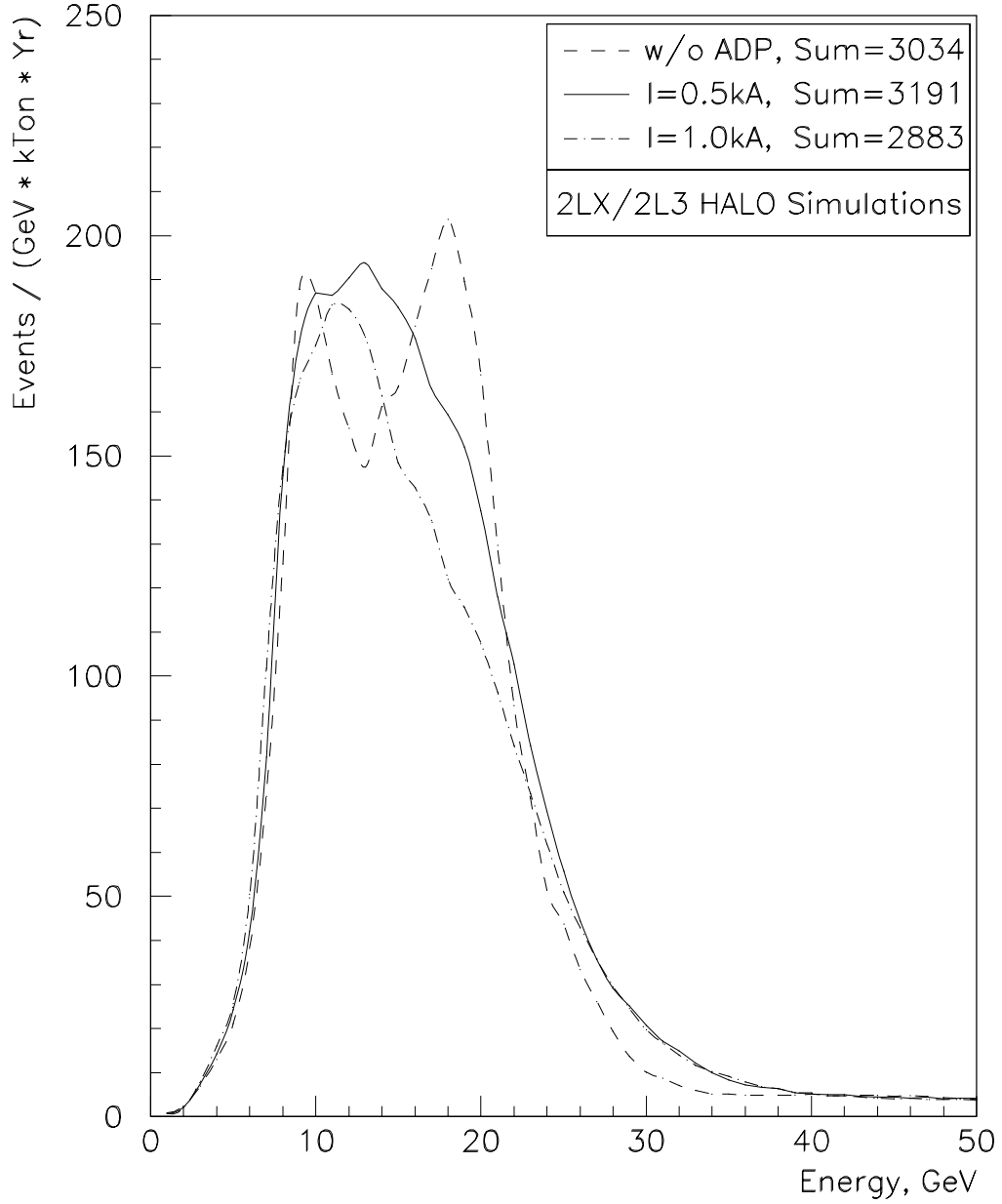


Figure 2.6: The ν_μ event rate for the 2LX/2L3 focusing systems with the different wire currents.

WBB. Far / Near NuMu Event Rate Ratio.

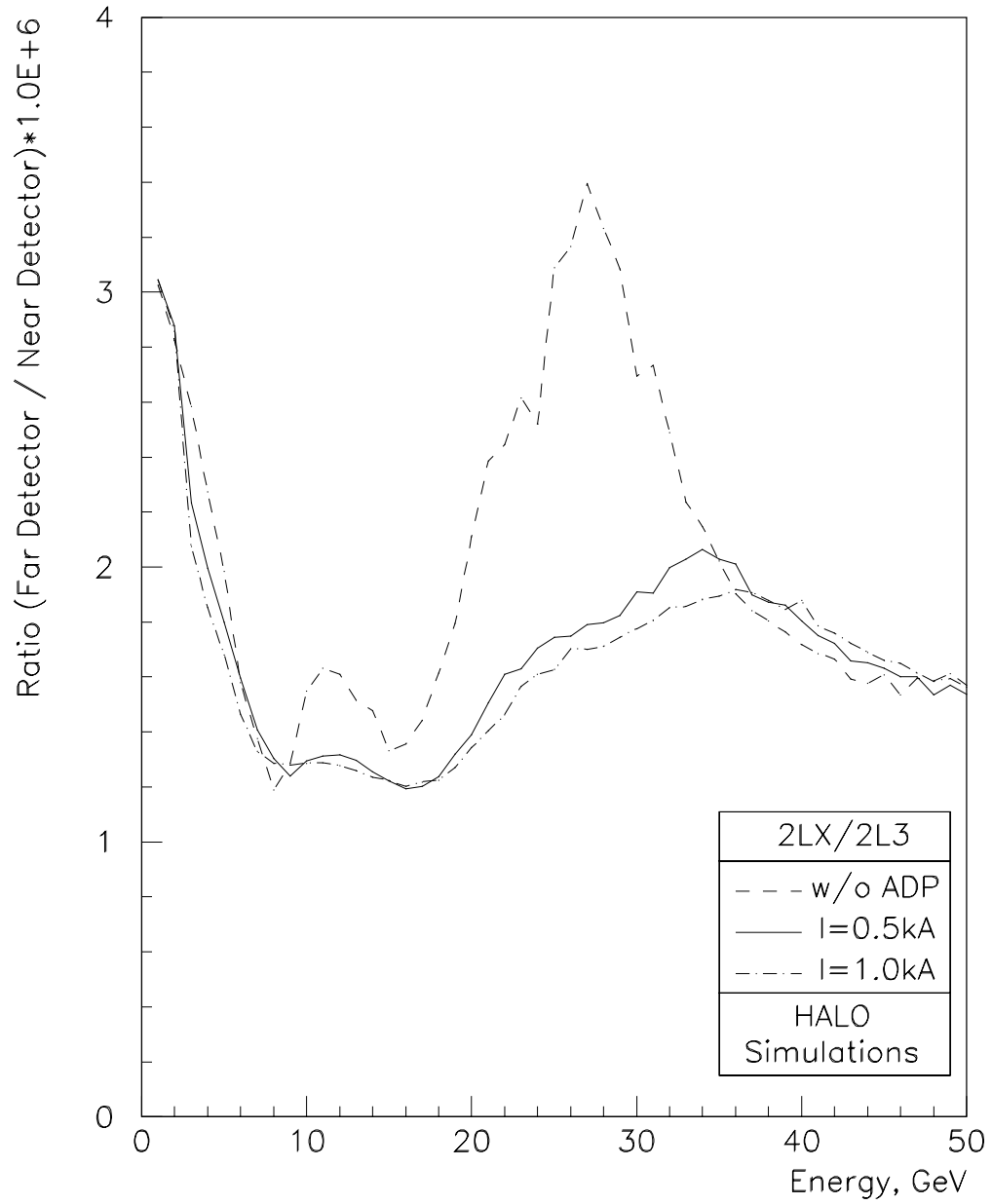
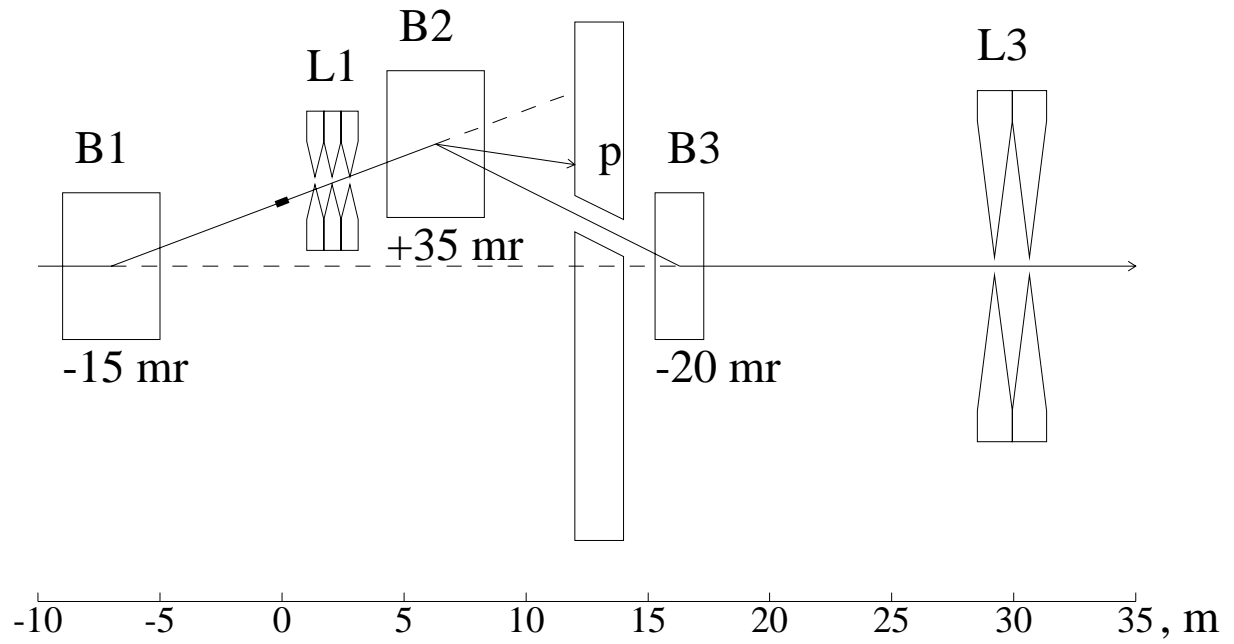


Figure 2.7: The Far/Near ratio for the 2LX/2L3 focusing systems with the different wire currents.

NBB. $3*L1/2*B/2*L3$ Focusing System.



Dipole Aperture: B2 12cm x 10cm (W x G)
B3 16cm x 12cm (W x G)

Figure 2.8: The layout of the $3L1/2B/2L3$ focusing system for the NBB.

NBB. Far Detector NuMu Event Rate.

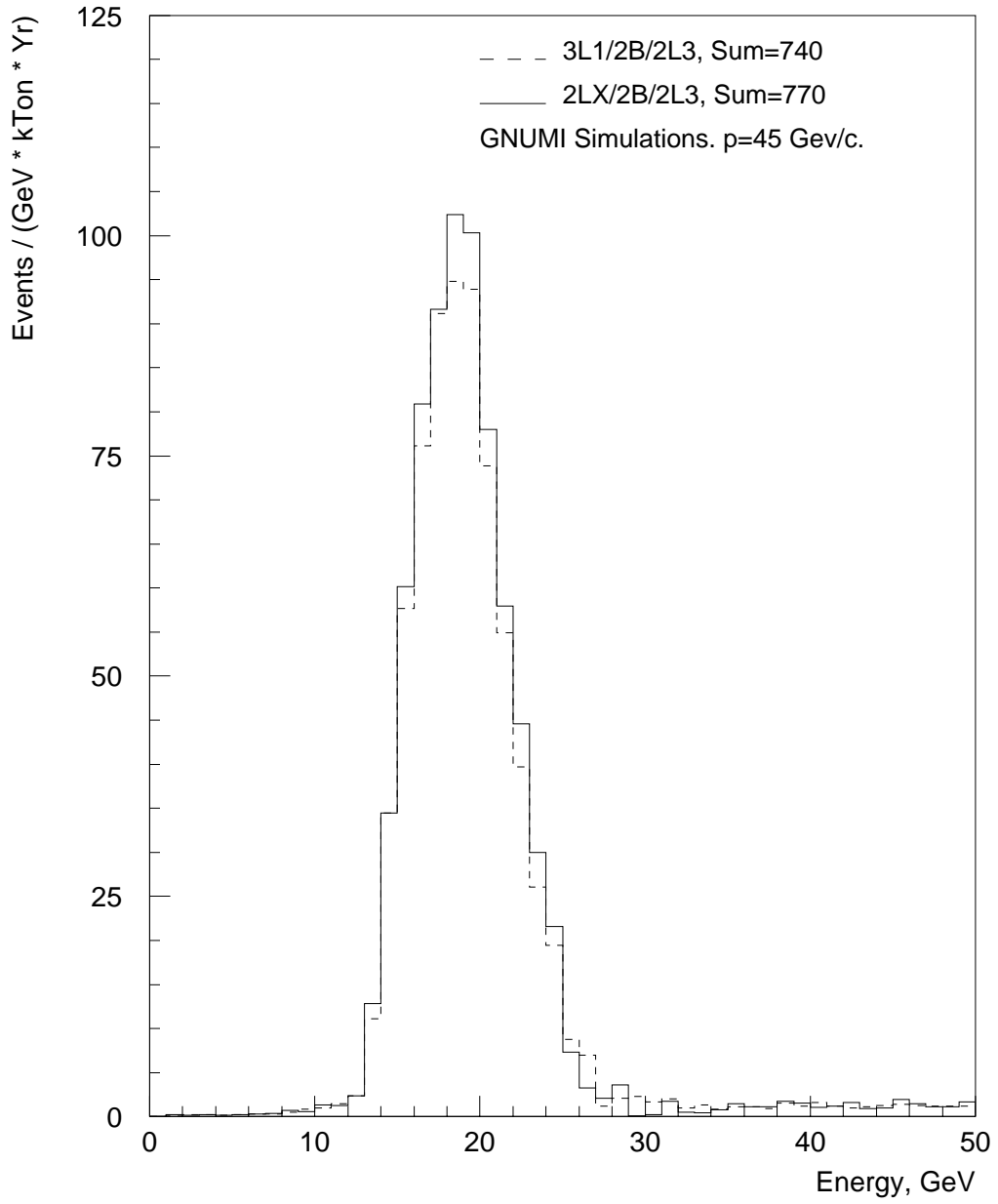


Figure 2.9: The ν_μ event rate for the 3L1/2B/2L3 and 2LX/2B/2L3 focusing systems at 45 GeV tune.

NBB. Far Detector NuMu Event Rate.

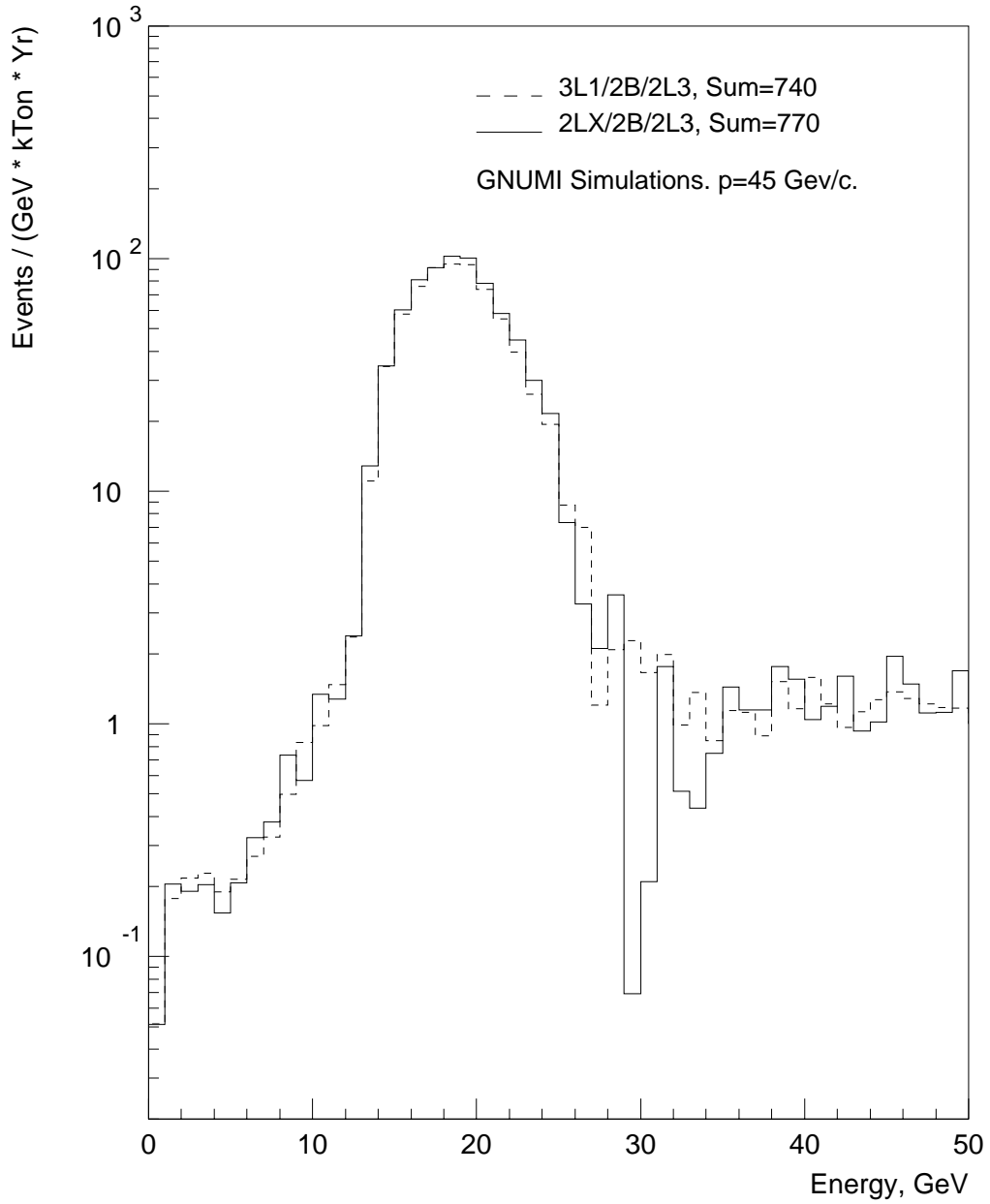


Figure 2.10: The ν_μ event rate for the 3L1/2B/2L3 and 2LX/2B/2L3 focusing systems at 45 GeV tune.

3 Parabolic Lenses

Some aspects of parabolic lens design have been described in [1].

3.1 Lens LX

The optimization of neutrino spectra for WBB and NBB shows that the new lens LX has geometrical parameters as listed in Table 3.1.

The outer surface of this lens consists of two paraboloids with parabola parameter $p = 1.297 \text{ cm}^{-1}$ connected together by a neck with the radius of 1.3 cm. The inner surface has a parabola part with the same p , but when the radial thickness of the shell reaches 2 mm (dimension 329.8 mm, Figure 3.1) it remains constant up to the lens flanges.

Parameter	Outer surface	Inner surface
Neck (hole) radius, cm	1.3	0.55
Parabola parameter, cm^{-1}	1.297	1.297
Parabola shift, cm	0.0	1.8
Max radius, cm	6.94	6.8
Full length, cm	125.0	128.0

Table 3.1: Lens LX geometrical parameters.

Focusing device (FD) consists of 2 lenses LX bolted together. The thickness of connecting flanges is equal to 15 mm. The dielectric (ceramic) supports between the connecting flanges and the outer conductor are provided in order to prevent the sagging of inner conductor and to damp its transverse vibration, but to allow the inner conductor to move longitudinally. The cooling of the inner conductor is produced by a low conductivity water sprayed from the system of external pipes through the holes in the outer conductor. In order to prevent the penetration of cooling water to the electrical contacts all of connections have to be vacuum tight. The internal radius of the outer conductor is equal to 9 cm. The stripline feeding the FD by a current will be connected to the lens assembly via coaxial connector providing the axial asymmetry of the current at the beginning of internal conductor not more than 0.5%. Such connection was used at the Serpukhov neutrino beam line.

Electrical parameters of LX focusing device are listed in Table 3.2, and waveforms of its current and voltage are shown in Figure 3.2.

Parameter	Focusing device
Inductance L , nH	392
Resistance R , μOhm	240
Peak current I , kA	320
Duty factor Q	765
Average power P , kW	32.3
Power flux from the neck surface, W/cm^2	20.5
Neck temperature jump ΔT , K	29.3

Table 3.2: Electrical parameters of the LX focusing device.

The evolution of the neck temperature in time for lens LX for various heat transfer coefficients (HTC) is shown in Figure 3.3 and the temperature distribution along the lens – in Figure 3.4. The stresses in a lens have been computed under the boundary conditions similar to the mentioned in [1] (section 3.2.2) and are represented in Figure 3.5 – pure magnetic stresses, Figure 3.6 – for various instants of time. The maximum stress is reached at the neck after the current pulse (maximum temperature) and equal to $44 \text{ N}/\text{mm}^2$.

3.2 Stripline

The focusing devices are feeded by a current via low inductance stripline. Figure 3.7 is a cross-sectional view of the preliminary stripline being considered. It consists of 8 aluminium plates with specific resistance $\rho = 2.9 \cdot 10^{-6} \cdot \text{Ohm} \cdot \text{cm}$, width a and thickness $d = 1 \text{ cm}$. As the peak voltage at the focusing device does not exceed 200 volts the thickness of 1 mm of the insulation layer between the opposite plates is more than sufficient to prevent the breakdown. Figure 3.8a shows that the average power flux from the surface, average current density and peak pressure to the stripline plates as well as the ratio of its inductance to the total inductance at the secondary side of a transformer (see Figure 3.8b, the parameters of power supply are not included) drop with increase of width a . If the inductance ratio is limited to $0.3 \div 0.35$ then the stripline width should be $20 \div 25 \text{ cm}$. The final optimization of a stripline will be done together with

the power supply design. To contain the forces generated by a current pulse, the plates will be bolted at appropriate intervals along the stripline length.

The average power flux from the stripline plates reaches a few hundreds W/m^2 . The temperature of stripline (width $a=25\text{ cm}$) is shown as function of heat transfer coefficient (HTC) of free convection in Figure 3.9. The IHEP experience for the stripline width of $30\div 40\text{ cm}$ gives the value of $HTC \approx 15\div 20\cdot\text{W}\cdot\text{m}^{-2}\cdot\text{K}^{-1}$. The expected value of a stripline temperature does not exceed $55\text{ }^\circ\text{C}$.

3.3 General layout

Figure 3.10 is the preliminary general view of Target Hall with the beam components for WBB and shielding, the power supply room and tunnels between them.

- The width of Target Hall is equal to $\approx 6.0\text{ m}$, room for power supply — 4 m , tunnel — 3 m .
- A discharge circuit is distributed over four cabinets. Each cabinet contains 25 capacitor banks, thyristor switch and 7-th harmonic correction circuit. The dimensions of cabinet: length — 1.9 m , width — 1.0 m , height — 1.7 m . and weight — 1800 kg .
- The transformer (3.0 m height, 1.8 m length, 1.0 m width and 9700 kg weight) is placed in a tunnel between Target Hall and power supply room in order to minimize the stripline length.

3.4 Focusing Device Support Design

The cross-sectional view of a Target Hall with focusing device and shielding is shown in Figure 3.11. The shielding dimensions are taken from [3] (Figure 3.23, p.72). The alignment table consisting of two frames (one — for vertical alignment of focusing device (FD), another one — for horizontal alignment) is placed on the top of the shielding. The lens assembly is mounted to the FD support frame by means of two vertical rods with appropriate dimensions sufficient to install the FD to the beam axis. The FD support frame is placed at horizontal alignment frame on three pins (system of ball-prism). Before installation the position of ball-pins will be aligned

at the special stand similar to the horizontal alignment frame to be sure in the right position of focusing device being installed. Another possibility — all the focusing devices have to be aligned at the same alignment table before the beam line assembly. There will be three positioning motors for vertical and two for horizontal adjustment of FD. All motors are remotely controlled.

All of the connections for power, water and instrumentation will be made on the top of the shielding. The flexible connection is placed between the stripline and remotely controlled connector (see Figure 3.12). Such connector was successfully used at the neutrino beam line at Serpukhov accelerator for the current value of 500 kA. Its principle of operation is based on using of low-melting temperature alloy. To disconnect the feeder it is necessary to heat the alloy by means of special heating units. As a flexible connection, the copper grids similar to ones described in [7] but for the average current of 15 kA will be designed. The insulation of the stripline vertical part closed to the lens assembly should have radiation resistance as the insulation between the connecting flanges and outer conductor.

The cooling water will be brought through the shielding in metal piping to the distribution system in FD. The water system should be a closed loop system that has rows of nozzles in the outer conductor spraying water into the inner conductor continuously.

The FD support frame with lens assembly, vertical rods and stripline should be carefully balanced in all directions to relieve the mounting and replacement of lens assembly.

Such system of focusing device support, alignment and feeding by current and cooling water allows to remove the systems for maintenance or repair from the high radiation and chemically active area.

3.5 Replacement of failed lens

The location of all connections at the top of the shielding means, that for well designed shielding, there is personal access to the connections. Upon entering the hall (in a few days after beam off) all of the connections of power, water and instrumentation will be disconnected at the top of the shielding. Two vertical rods are installed at the alignment table through the holes in FD support frame in order to prevent its rotation during lifting. Special lifting fixture is attached to the FD support frame.

The shielding blocks with arrows in the vertical direction (Figure 3.11) are removed by Target Hall overhead crane and placed in a location far enough from the personnel so as to provide minimal exposure. The most radioactive blocks (arrows in the horizontal direction) are not removed, but shifted at the distance sufficient to lift the failed lens assembly in a vertical direction.

FD support frame with lens assembly and stripline is removed by overhead crane and placed in a coffin. The new FD support frame with lens assembly and stripline will then be put onto the alignment table utilizing the vertical rods as director. The ball-prism system will provide an accurate position of the lens assembly at the beam axis. The movable shielding blocks are returned to the previous position by driving motors as well as the removed blocks by overhead crane. The power, water, and instrumentation will be reconnected and tested. After successful tests the FD will be ready for operation.

Such conception of replacement of failed FD leads to the height of Target Hall at least of 7.5 m. To have a smaller height it is necessary to remove the failed FD to the right side as it is shown in Figure 3.13. The procedure of FD replacement differs from the one described above only by the shielding dismantling (assembly):

- shielding blocks 1 and 3 are removed by overhead crane;
- shielding block 4 is shifted and then removed;
- shielding blocks 2 and 5 are shifted at the appropriate distance;
- FD support frame is lifted over block 5 and removed to the right side.

In this case one additional movable shielding block is needed and the volume of shielding dismantling is significantly larger. The utilizing of the movable shielding blocks is very important to be sure to have no break of the alignment table and FD vertical rods during the shielding assembly or dismantling.

3.6 Switching between Wide Band and Narrow Band Beams

The focusing systems for wide band and narrow band beams have the difference only in the vertical position and direction of the first focusing device 3L1 (or 2LX) as well as of the target.

- Primary proton beam is bent at an angle of 15 mrad in a vertical plane by pre-target bending magnets. No movements of bending magnets are necessary.
- Target (old or new) has new vertical position -10 cm and direction -15 mrad, but the same position along the beam axis. There are two possibilities: the alignment system of the target provides all necessary movements of old target, or a new target is used with appropriate dimensions of its vertical supports.
- The first focusing device (FD1) of WBB is replaced by a similar one, which differs from the old one only by its vertical supporting rods and stripline dimensions.
- Two magnets NBR and magnet NBN are installed at the NBB line. The system of installation and replacement of these magnets is similar to the FD1 one. All of the connections for power, cooling water and instrumentation are made on top of the shielding. The magnet stands should have the alignment systems to ensure the position (mainly the field angle) during the long run operation. Preliminary magnets parameters computed by program POISSON are given in Table 3.3.

Dipole	NBR	NBN
Nominal field B , Tl	1.4	1.5
Vertical gap, cm	10	12
Useful aperture $V \times H$, cm ²	10×12	12×14
Field variation in the useful aperture, $\Delta B/B$	± 0.005	± 0.005
Nominal current, A	1000	1000
Power, kW	148	78
Iron length, m	2.0	2.0
Magnet weight, T	7.4	9.8
Width, cm	86.0	89.0
Height, cm	64.0	72.0
Full length, cm	243	250

Table 3.3: Dipole magnet parameters.

As the NBR magnets just follow the FD1 practically without any beam collimation, the expected absorbed doses in the magnet coils will be on the same order of magnitude as ones in the first lenses[1]. For this reason these magnets should have radiation resistant coils (mineral insulation, for example – magnesium oxyde). The given parameters of NBR-magnet have been computed for the coil wounded from the mineral (MgO) insulated cable with external dimensions of copper shell of $16.75 \times 16.75 \text{ mm}^2$, current copper conductor of $11.0 \times 11.0 \text{ mm}^2$ and cooling hole diameter of 7.0 mm. This magnet may operate only in d.c. mode. The value of power of NBN magnet is given also for d.c. operation.

- The NBB proton dump will be placed in the initial installation of the beam line and remain there until the line is disassembled. The dump will have a removable upper core that allows the WBB second focusing device to fit.

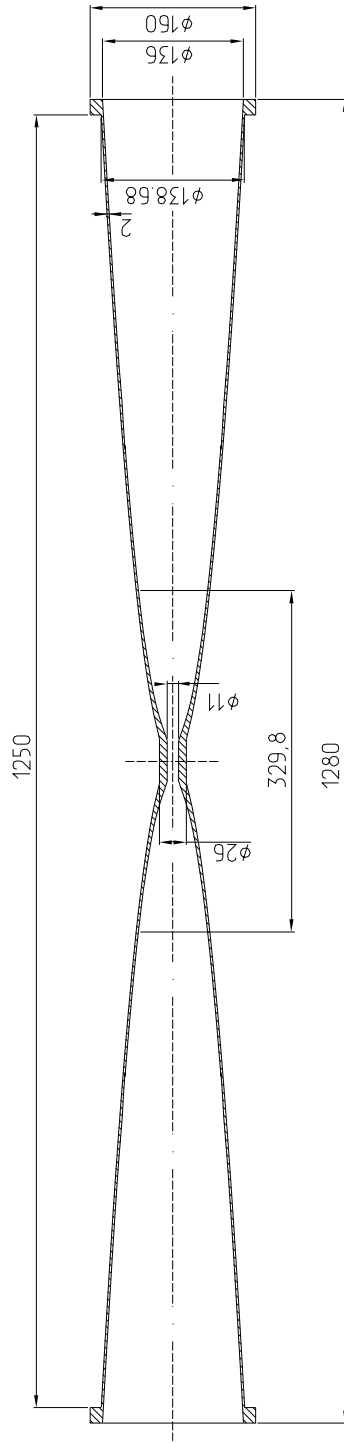


Figure 3.1: Cross-section of the internal conductor of lens LX.

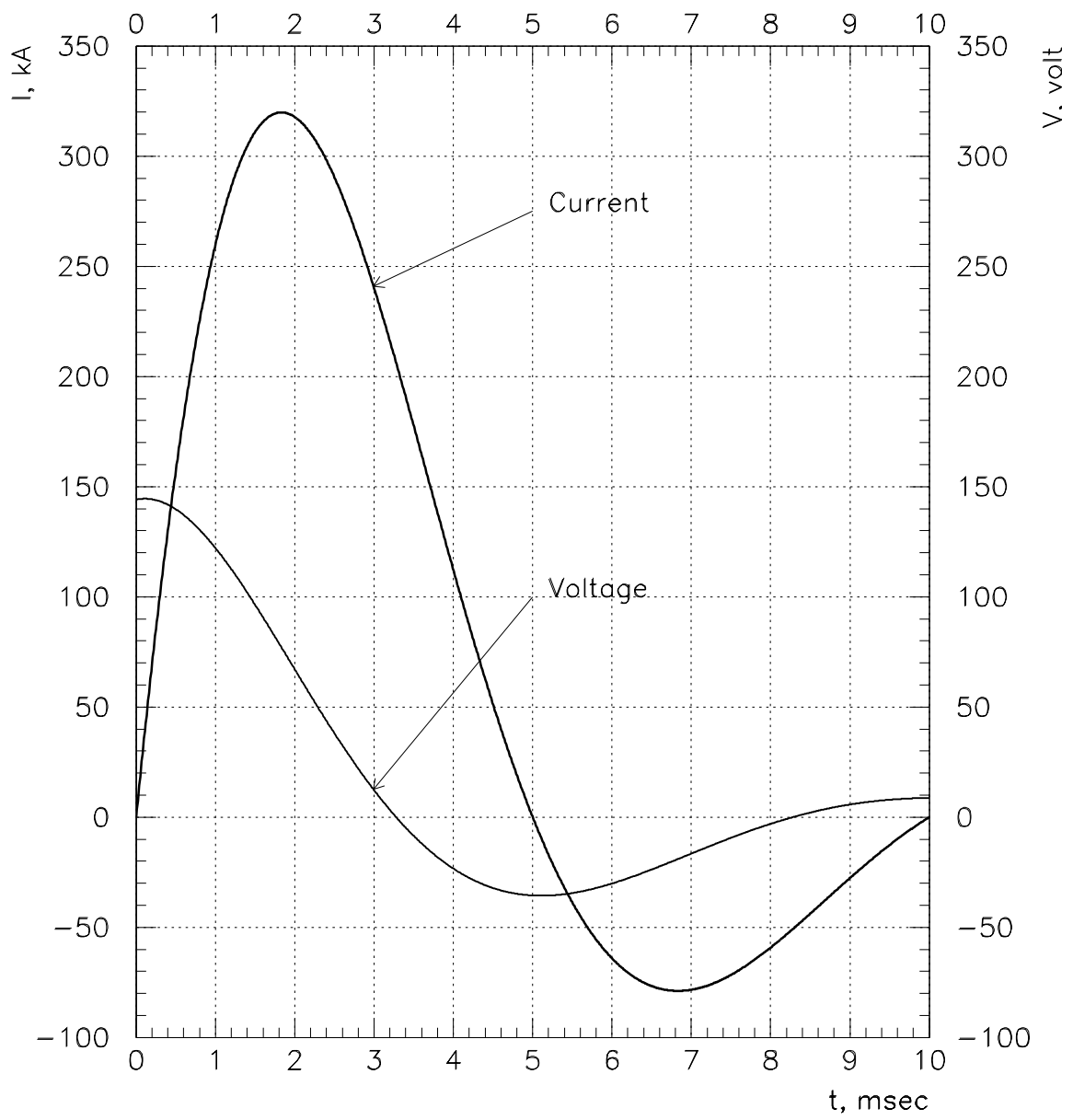


Figure 3.2: Waveforms of current and voltage of FD (2LX).

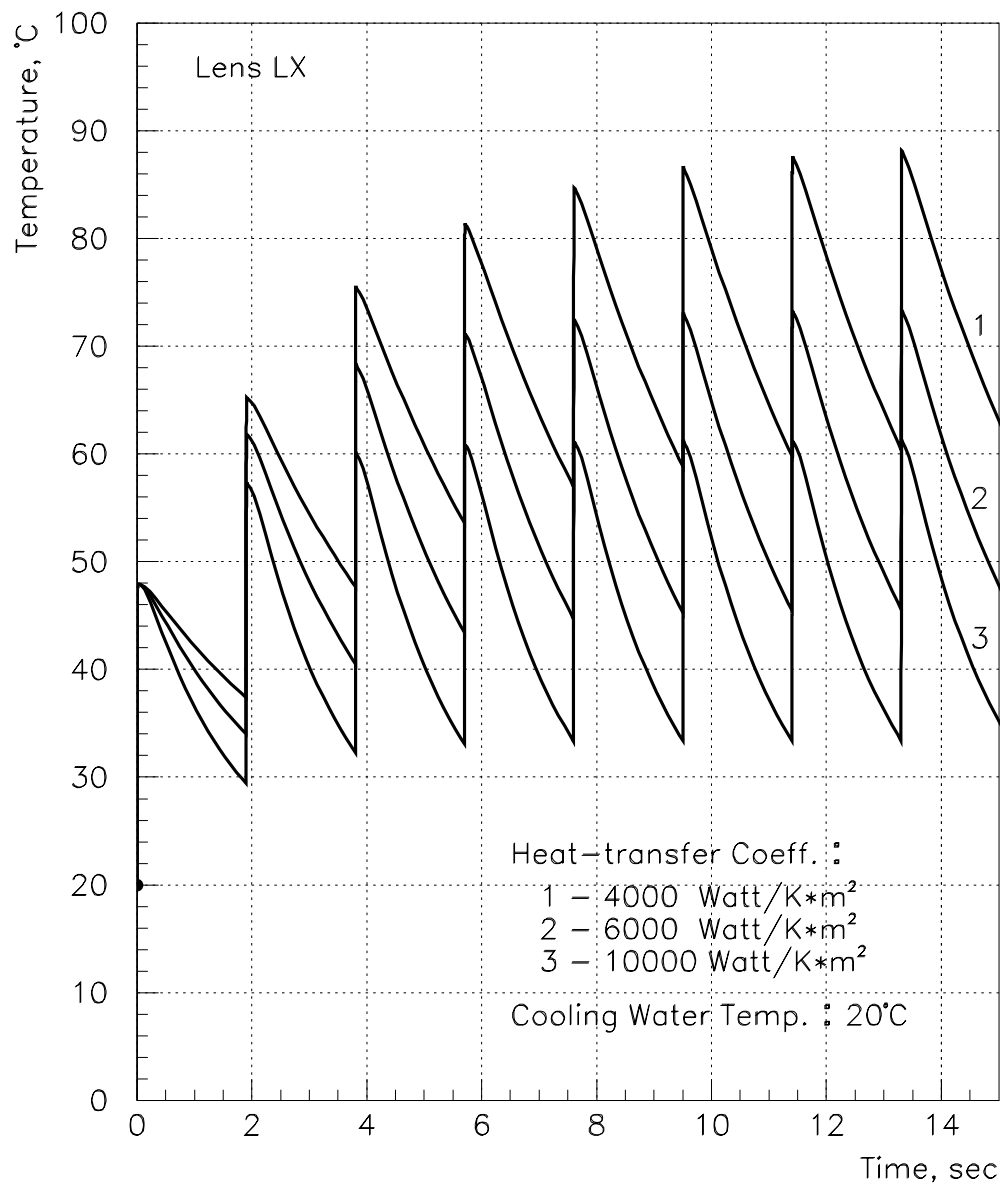


Figure 3.3: Temperature versus time in the neck region of the lens LX.

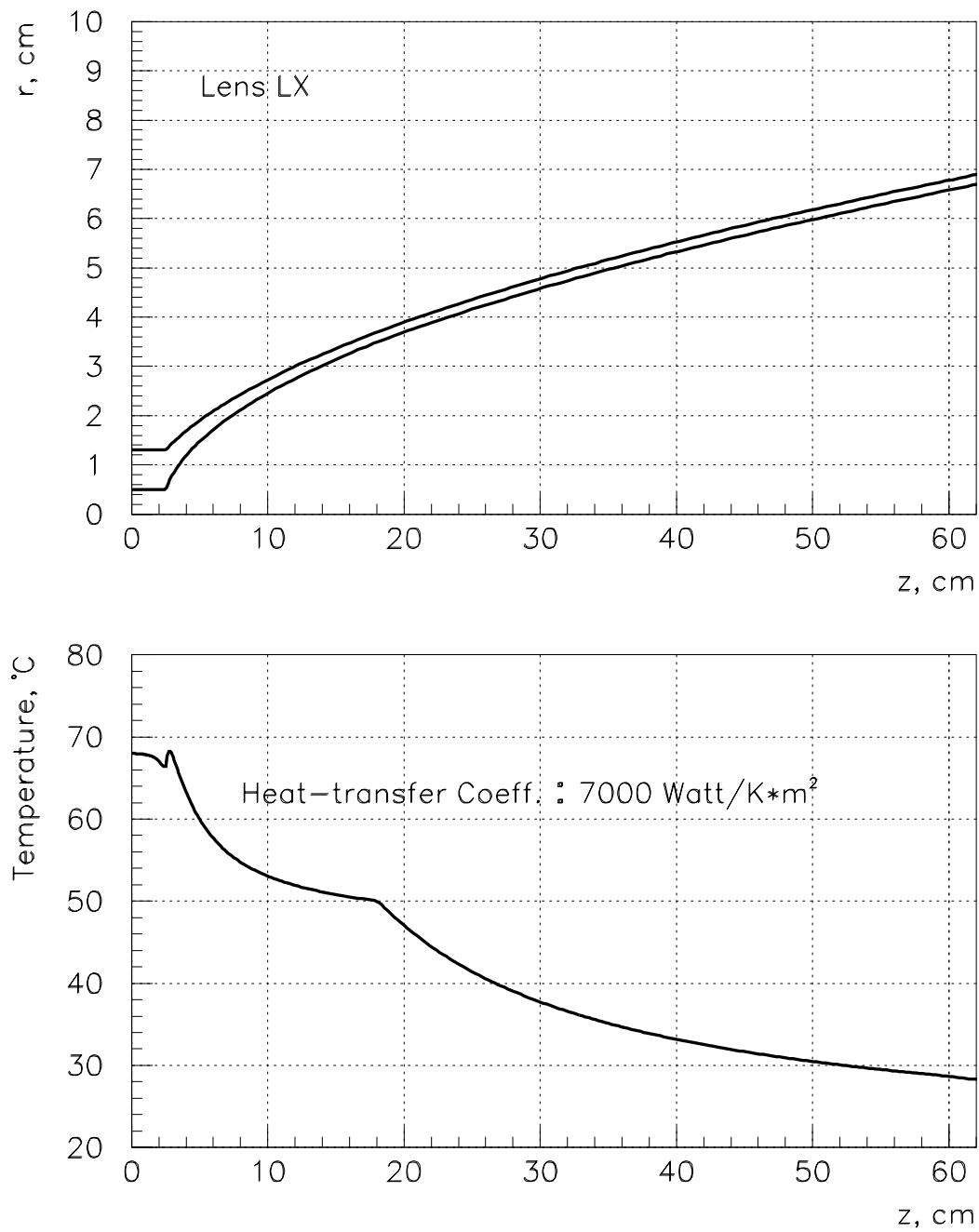


Figure 3.4: Maximum temperatures along the lens LX in a steady state.

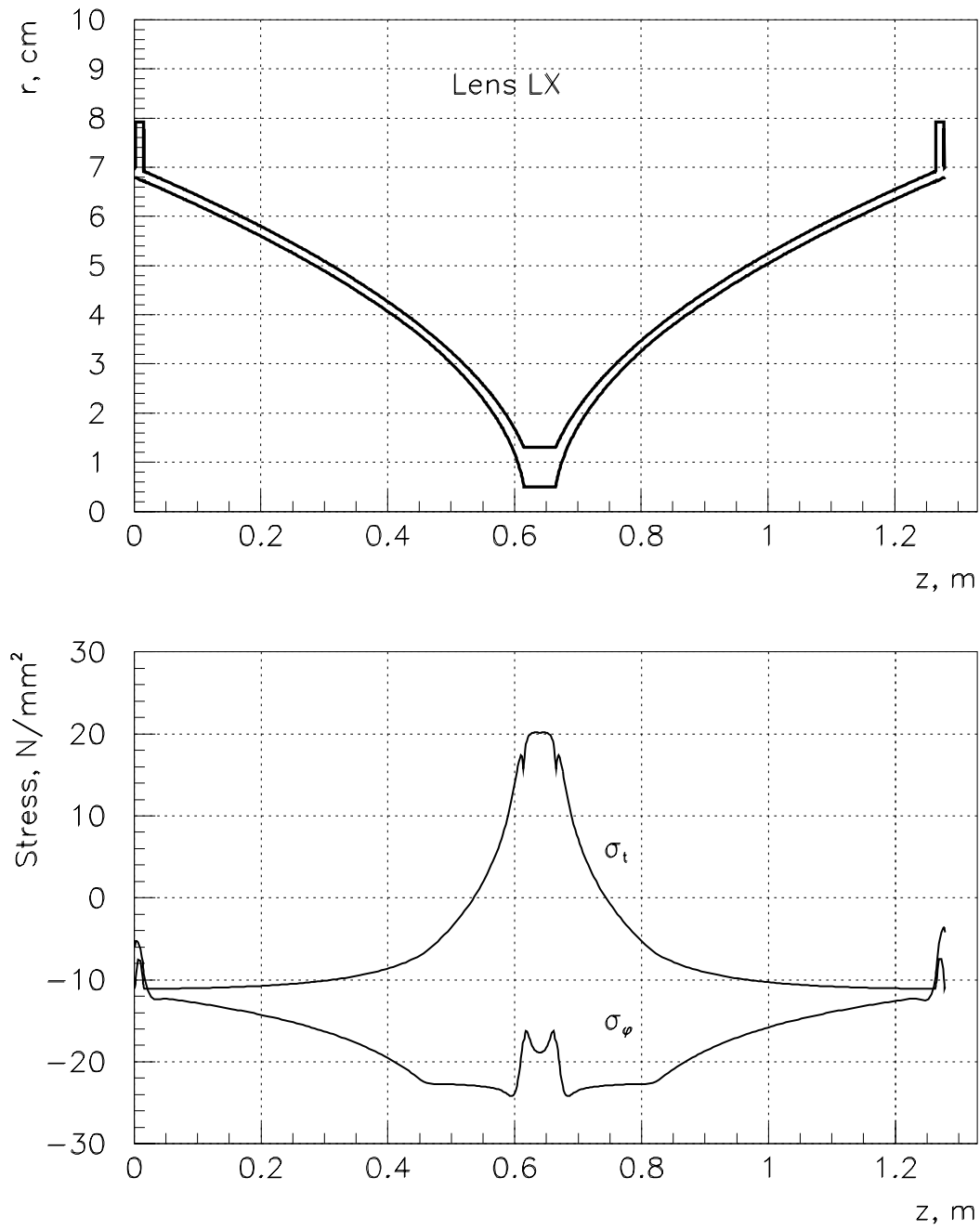


Figure 3.5: The axial (σ_t) and circumferential (σ_ϕ) stresses along the lens LX produced by current 320 kA.

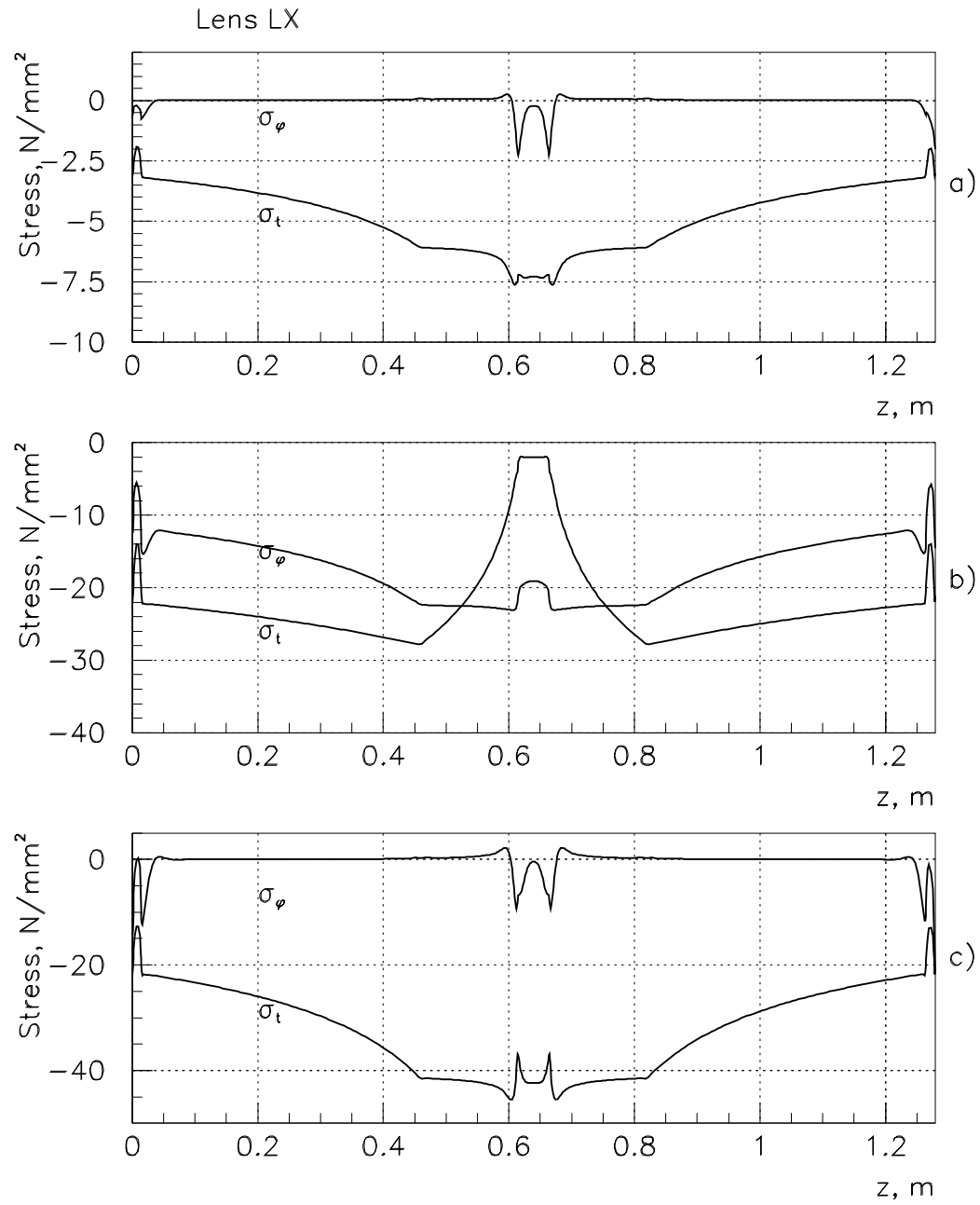


Figure 3.6: The axial (σ_t) and circumferential (σ_ϕ) stresses along the lens LX before current load (a), at the peak of current pulse (b) and just after the pulse (c).

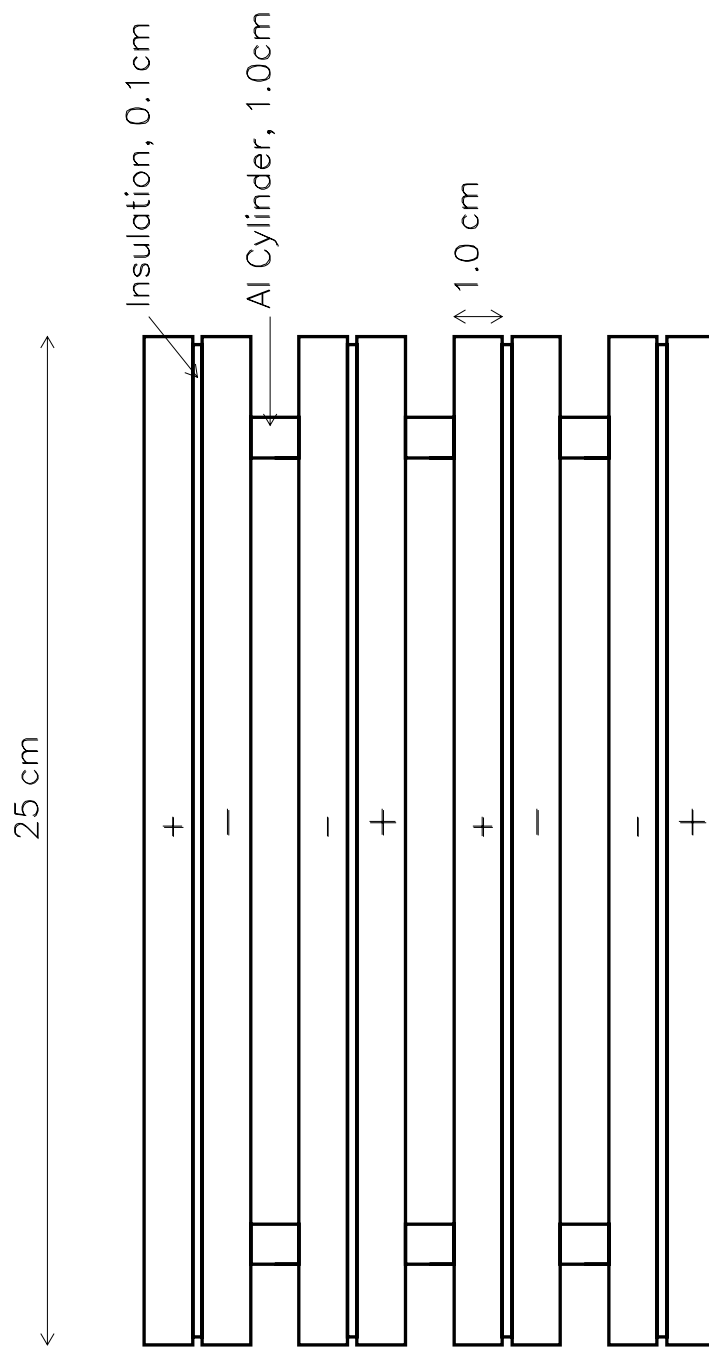


Figure 3.7: Cross-sectional view of the stripline.

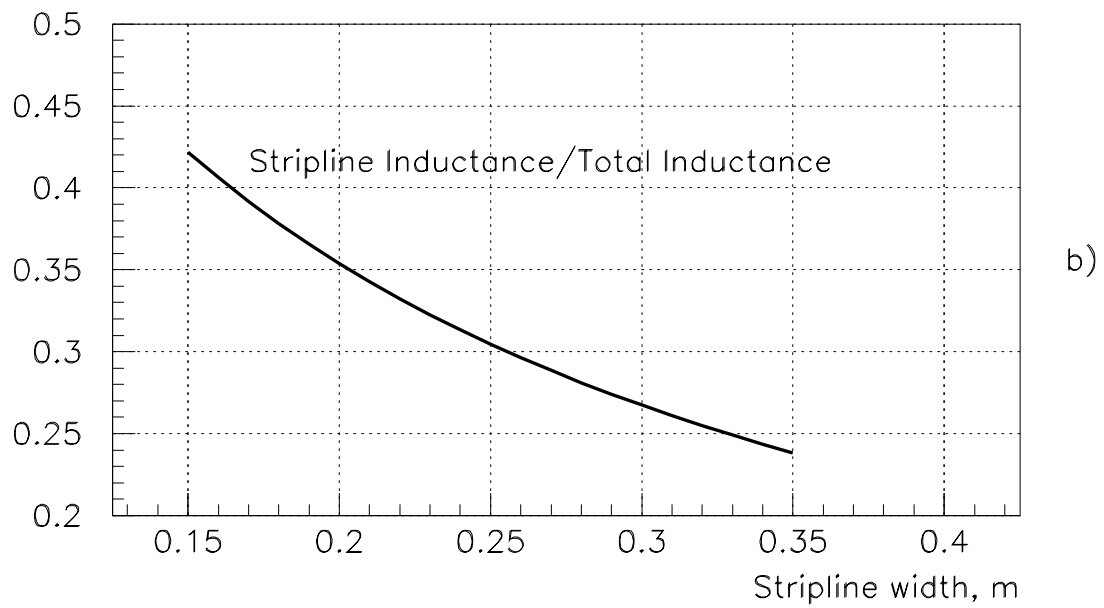
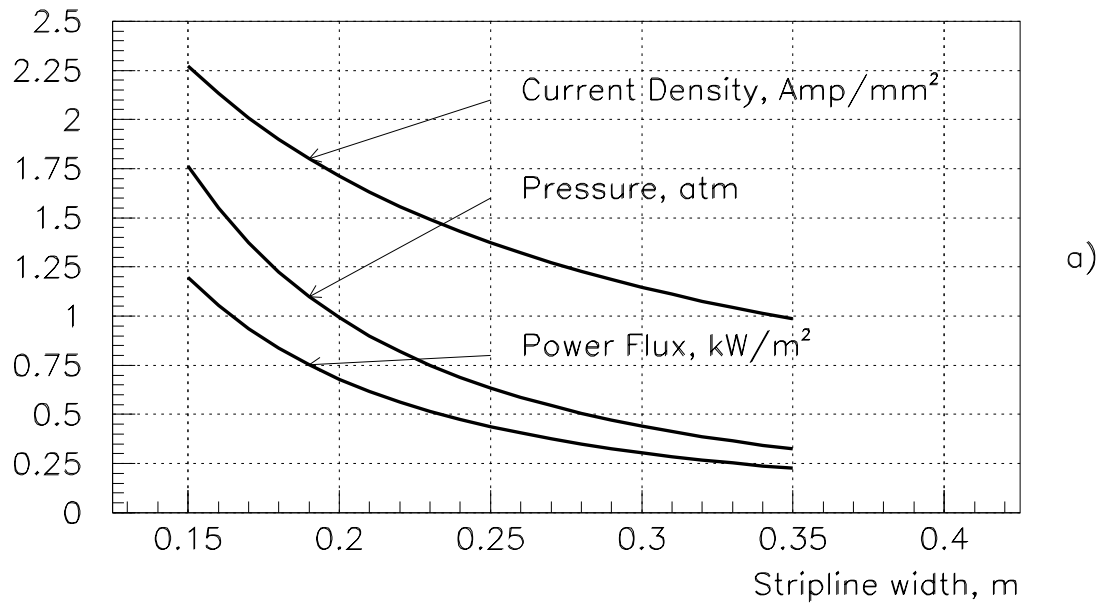


Figure 3.8: Stripline characteristics versus its width.

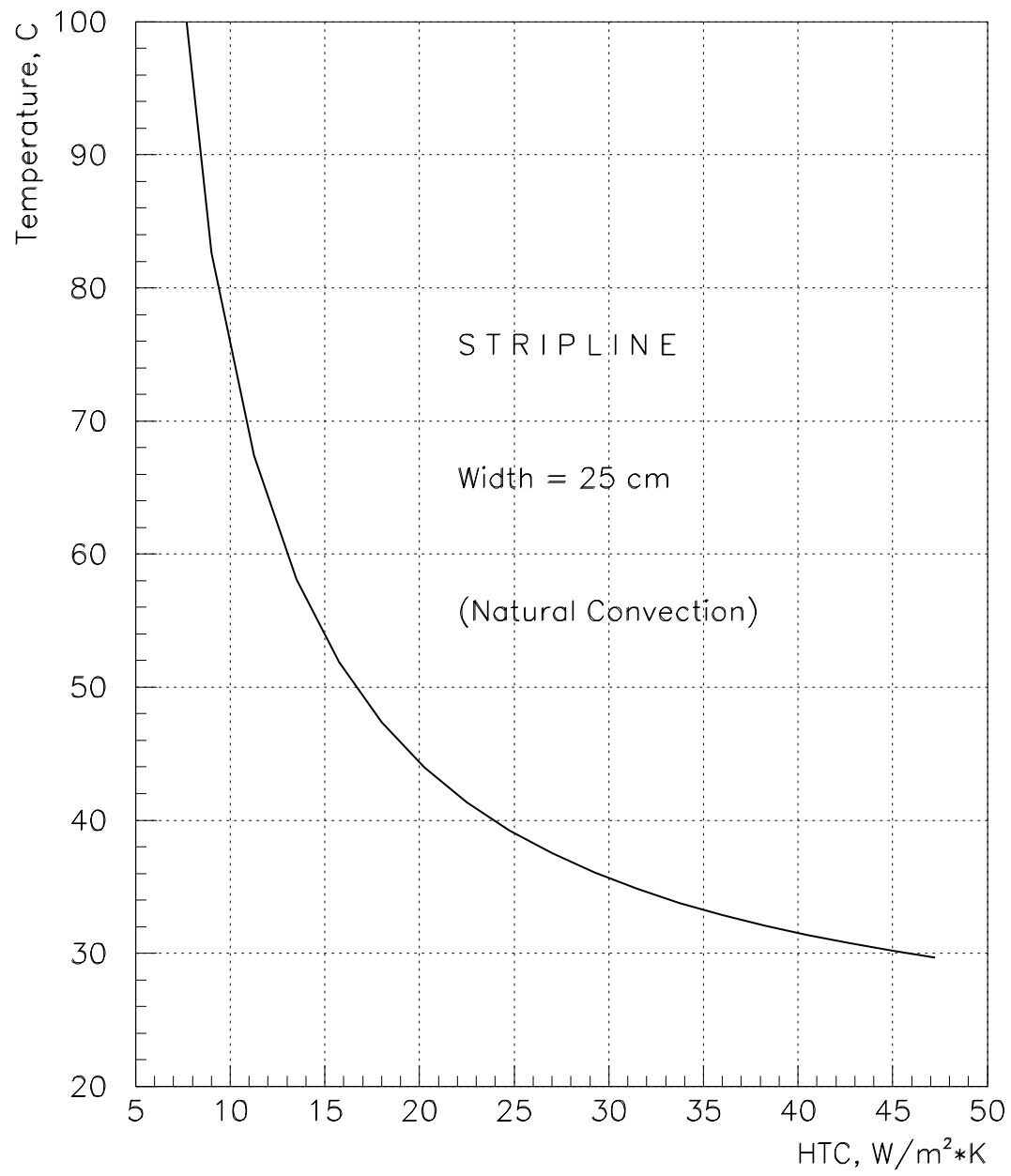


Figure 3.9: Temperature of the stripline as function of HTC.

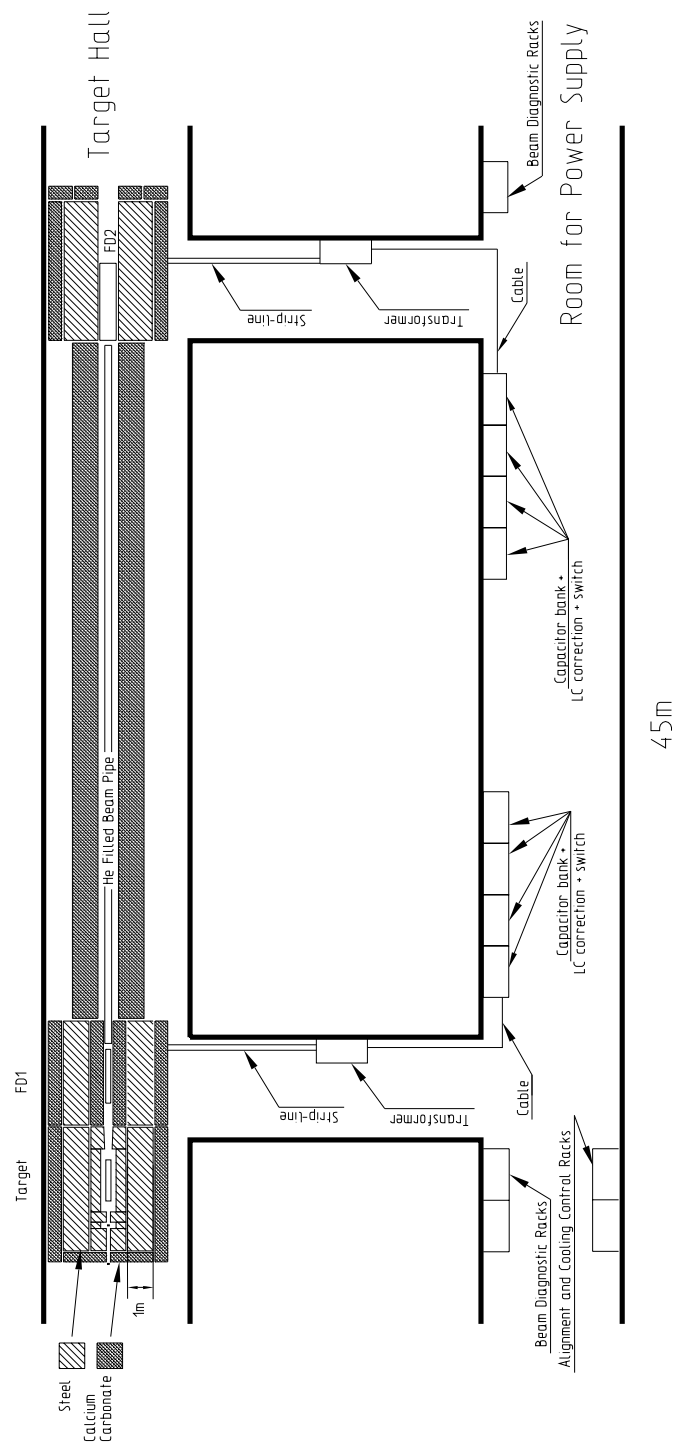


Figure 3.10: General layout of WBB.

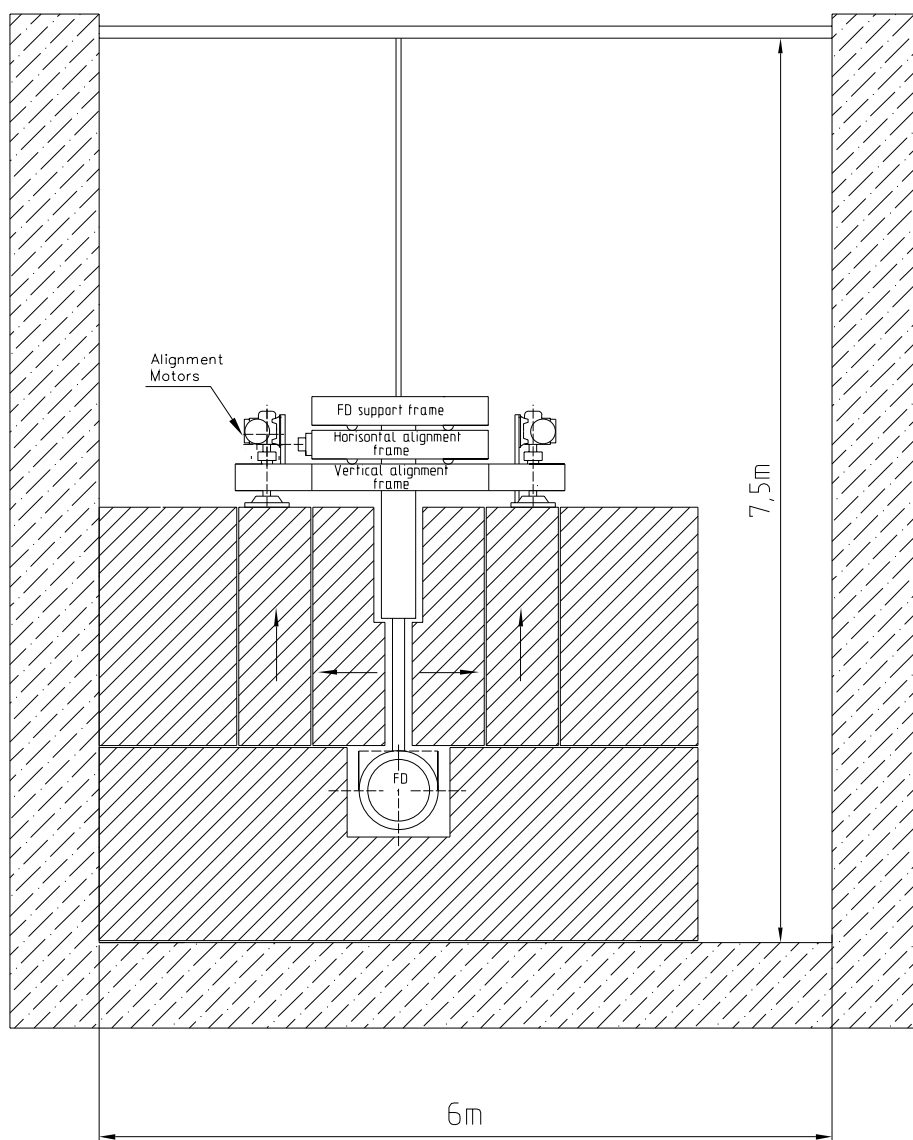


Figure 3.11: Cross-section of Target Hall with FD.

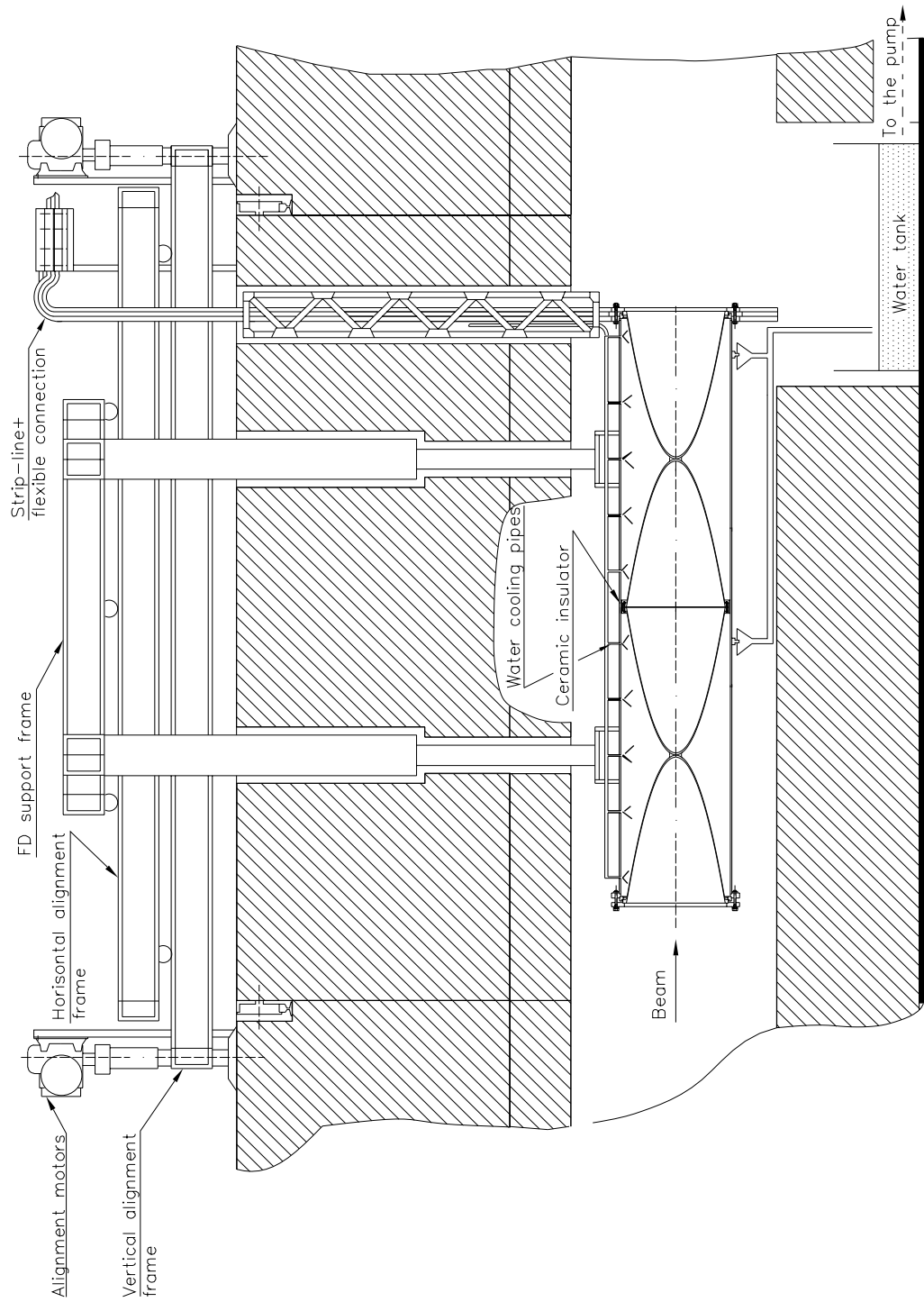


Figure 3.12: Cross-section of the shielding and FD along beamline.

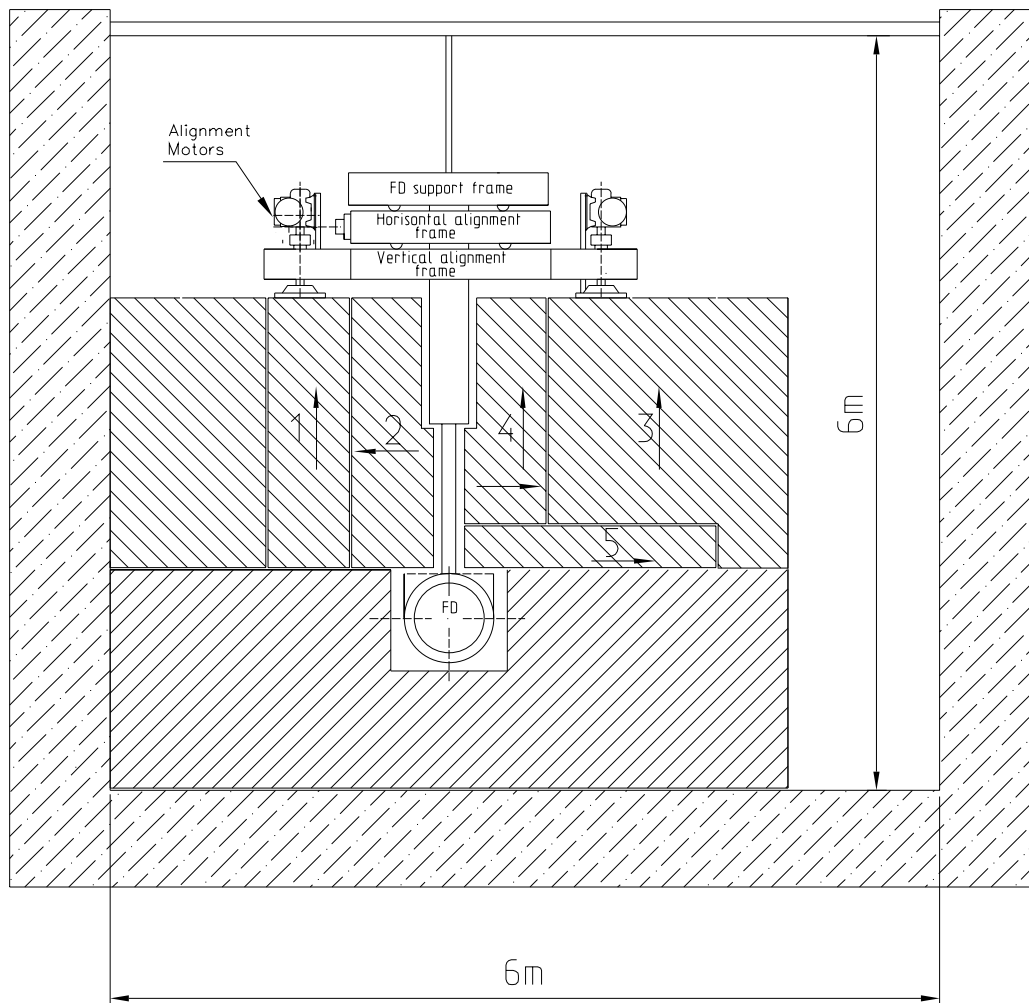


Figure 3.13: Cross-section of Target Hall with FD removal to the right side.

References

- [1] Preliminary Design Work and Neutrino Beam Calculations for the NuMI Project, IHEP, Protvino, 1997.
- [2] I.Azhgirey et al, Proc. XV Conference on Charged Particles Accelerators, p.74, Protvino, 1996.
- [3] Status Report: Technical Design of Neutrino Beams for the Main Injector (NuMI), NuMI-B-92, (TM-1946), Batavia, 1995.
- [4] Conceptual Design Report: Main Injector Neutrino Program, FNAL, 1991, edited by R. Bernstein et al.
- [5] I.S.Baishev et al., "Calculation of the Residual Gamma Radiation Dose Rate Near Elements of High Energy Accelerators", IHEP Prprint 86-76, Protvino, 1986.
- [6] S. P. Timoshenko and J. N. Goodier, Theory of elasticity, 2nd edition, "Science", Moscow, (1979).
- [7] G. Acquistapace et al, CERN-ECP/95-14, July 1995.